Coordination Chemistry Reviews 469 (2022) 214671

Contents lists available at ScienceDirect

Coordination Chemistry Reviews

journal homepage: www.elsevier.com/locate/ccr

Review

Luminescence thermometry with transition metal ions. A review

L. Marciniak [a,*], K. Kniec [a], K. Elżbieciak-Piecka [a], K. Trejgis [a], J. Stefanska [a], M. Dramićanin [b,c,*]

[a] Institute of Low Temperature and Structure Research, Polish Academy of Sciences, Okólna 2, 50-422 Wroclaw, Poland
[b] Centre of Excellence for Photoconversion, Vinca Institute of Nuclear Sciences - National Institute of the Republic of Serbia, University of Belgrade, P.O. Box 522, Belgrade 11001, Serbia
[c] College of Sciences & CQUPT-BUL Innovation Institute, Chongqing University of Posts and Telecommunications, Chongqing 400065, PR China

ARTICLE INFO

Article history:
Received 30 April 2022
Accepted 8 June 2022
Available online 21 June 2022

Keywords:
Luminescent thermometry
Transition metal ions
Chromium
Manganese

ABSTRACT

Transition metal (TM) ion activated phosphors are increasingly being used as probes for luminescence thermometry. Their luminescence is characterized by strong absorption and emission bands that span the visible and near-infrared spectral ranges and are highly susceptible to temperature variations. Due to the latter characteristic, sensitive and reliable remote temperature measurements can be performed by observing temperature-induced changes in TM ion emission intensities, emission bandwidths and bandshifts, and excited state lifetimes, as well as the temperature dependences of the intensity ratios between various emission bands in single or double activated phosphors. This review provides a systematic analysis of the performances of luminescent thermometers based on different TM ions and discusses the relations among the TM spectroscopic properties, characteristics of the host material structure, and thermometric performance. Particular attention is given to the engineering of energy transfer between TM and other dopant ions to obtain highly sensitive thermometers. Finally, several typical application examples from recent literature are highlighted.

Contents

Abbreviations: TM, Transition metal; Ln3+, Lanthanide; CT, Charge transfer; CFS, Crystal Field Strength; LT, Luminescent thermometers.

* Corresponding authors at: Institute of Low Temperatre and Structure Research, Polish Academy of Sciences, Okólna 2, 50-422 Wroclaw, Poland (L.Marciniak); Centre of Excellence for Photoconversion, Vinca Institute of Nuclear Sciences - National Institute of the Republic of Serbia, University of Belgrade, P.O. Box 522, Belgrade 11001, Serbia (M. Dramićanin).

E-mail addresses: l.marciniak@intibs.pl (L. Marciniak), dramican@vinca.rs (M. Dramićanin).

https://doi.org/10.1016/j.ccr.2022.214671
0010-8545/

1. Luminescence thermometry

The continuous expansion of the sensor market, with particular emphasis on temperature sensors, is a response to the increasing demand for the analysis of temperature changes in various scientific fields and industry [1,2]. According to the latest data, it is estimated that the value of the temperature measurement market is 6412.5 Million USD in 2020 [2]. Accurate information about temperature, one of the most important thermodynamic parameters, enables the diagnosis of medical conditions, as increased temperature is one of the first symptoms of many types of inflammation and diseases [3–7]. In industry, temperature regulates the pace and nature of production processes, and its control enables equipment diagnostics [8–11]. The history of temperature measurements dates back to III century B.C., when Philo of Byzantium described an instrument for reading temperature [12]. Even though many centuries have passed since then, new techniques for determining temperature are still appearing. In addition to thermometers that use thermal expansion of solids, liquids, or gas and thermoelectric phenomena for temperature measurement, thermometers that perform remote temperature reading are being developed [13,14]. Remote temperature reading is particularly important because it is a non-invasive modality that does not disturb the operation of the tested system in real time. This characteristic is of particular importance in many application areas. Among thermometers of this type, infrared cameras are the most common. In this case, real-time 2D temperature imaging is also possible. These devices use thermal radiation emitted by objects, and by analysing the intensity of this radiation in the range of 7–14 μm, they provide information about the temperature distributions of objects in a simple and rapid manner. Unfortunately, a significant limitation of this technique is the fact that the exact temperature reading depends on the input parameters in the form of the emissivity of the tested object [13]. and the emissivity is often difficult to determine or varies over time. Hence, the reliability of the temperature reading is reduced. In addition, most infrared cameras enable imaging of only the surface of the tested object, as most objects are not transparent in the spectral range of 7–14 μm [15]. A relatively new method of remote temperature reading is luminescence thermometry, which exploits the luminescence variations of materials due to temperature fluctuations [14,16–21]. In this technique, the temperature is determined by analysing the luminescence parameter of the phosphor in physical contact with the analysed object [14,17,19,22,23]. This contact is ensured by applying a phosphor layer to the tested object, or, as is the case in biological applications, by introducing phosphor nanoparticles into cells or attaching them to specific tissues. After calibration, it is possible to estimate the temperature of the tested object by analysing the luminescence parameter. Depending on the type of luminescence parameter used, luminescence thermometry can be divided into seven different techniques: a) emission intensity, b) emission bandshift, c) emission bandwidth d) polarization, e) ratiometric intensity, f) emission kinetics, and g) single band ratiometric approaches (Fig. 1) [23,24]. The advantages and disadvantages

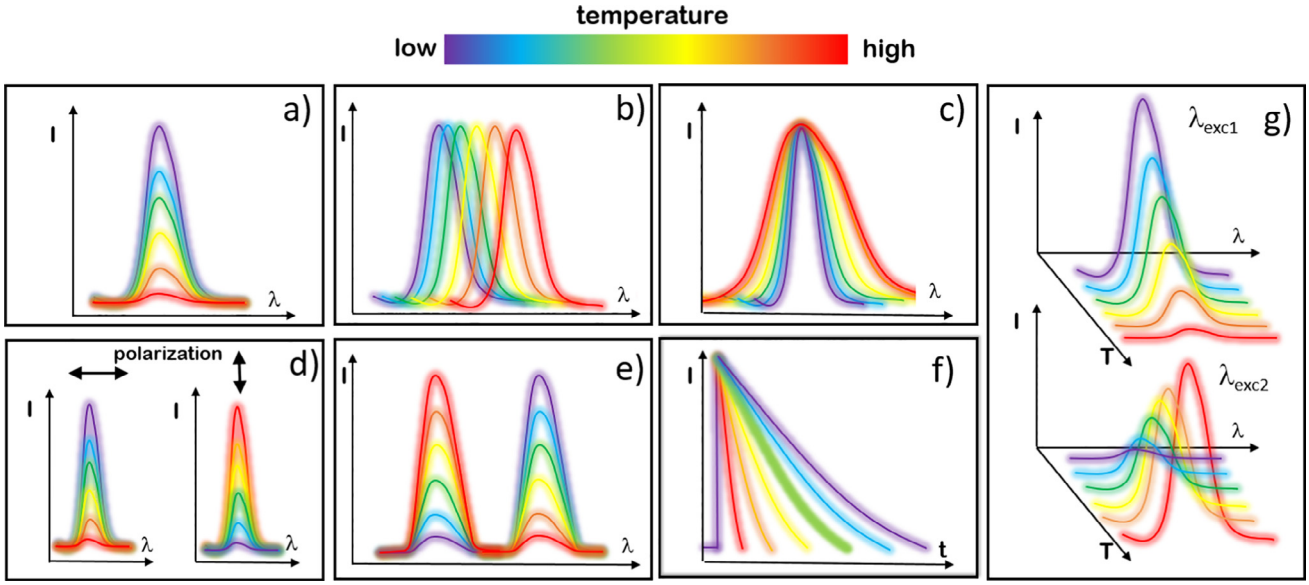

Fig. 1. Different strategies of temperature reading in luminescence thermometry: intensity based LT-a); bandshift based LT-b); bandwidth based LT-c); polarization based LT-d); ratiometric LT-e); luminescence kinetics based LT-f); single band ratiometric LT-g).

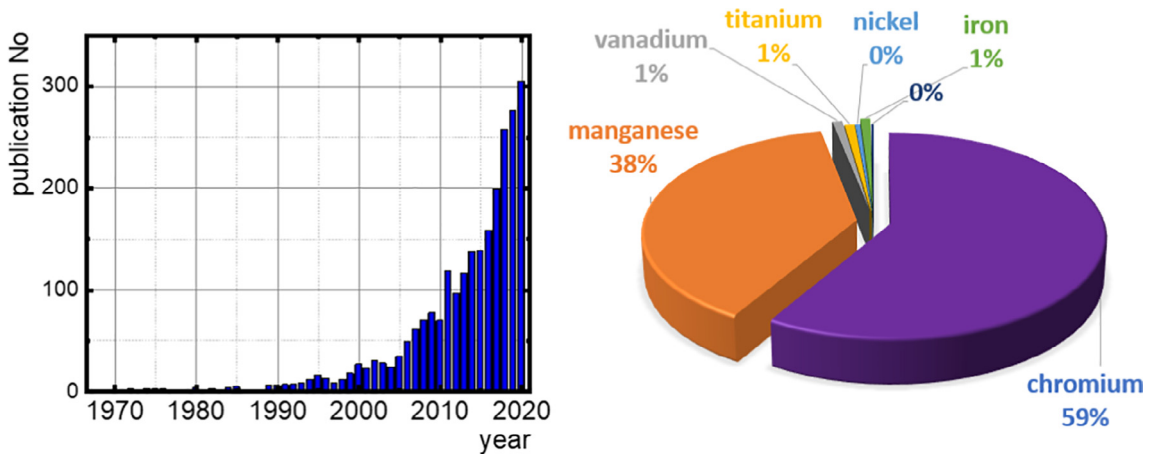

Fig. 2. Number of publications per year devoted to TM-based luminescence thermometers-a) and the percentage share of works in luminescence thermometry devoted to individual ions-b).

of these individual techniques have been described in detail previously [14,16–19,22,23,25]. As they provide the most reliable temperature readout, enable simple measurement, and entail low equipment cost, the most popular and most often described methods are ratiometric approaches and a technique that uses the disappearance of luminescence.

As many different types of materials are luminescent, there are ample choices when selecting materials for luminescence thermometry probes [14,16,22]. Among them, the most common are organic dyes, luminescent polymers, carbon dots, metal–organic frameworks, semiconductor quantum dots, fluorescent diamonds, and inorganic materials doped with optically active ions. The materials in the latter group are among the most intensively researched in recent years due to their high mechanical, chemical, and thermal strengths, which enable their use in extreme conditions and at high temperatures[14,16–21,26]. The luminescence properties of these materials are determined by the type of luminescent admixture, among which two groups are of the particular importance: materials doped with trivalent lanthanide ions (Ln^{3+}) and transition metal (TM) ions. Due to the weak electron–phonon coupling in Ln^{3+}, which results from the 4f orbital shielding by the 5 s and 5p orbitals, Ln^{3+} has unique luminescence properties that are particularly

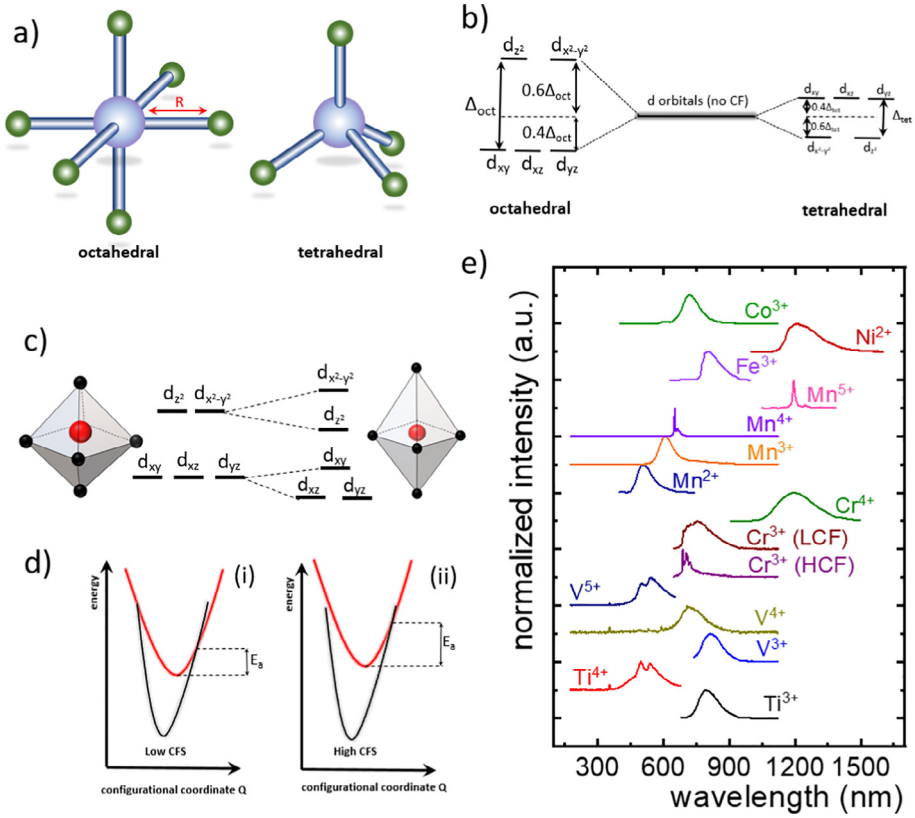

Fig. 3. Visualization of the octahedral and tetrahedral crystallographic sites preferentially occupied by the TM ions-a); splitting of the 3d energy levels of TM in octahedral and tetrahedral environment-b); the influence of the polyhedral distortion on the splitting of the 3d energy levels-c); schematic visualization of the influence of CFS on the activation energy on the basis of the $3d^3$ electronic configuration-d); representative emission spectra of TM-doped luminescent thermometers-e).

well-suited for luminescence thermometry. In particular, Ln^{3+} has narrow emission, which facilitates spectral separation of bands during spectral measurements; a long luminescence lifetime; and a unique configuration of electron energy levels, which enables the activation of various energy transfer processes between dopant ions that can be exploited for luminescence thermometry [14,16,20]. So far, most published research studies and reviews in the luminescence thermometry field have been related to this type of material. In recent years, however, there has been increasing interest in TM ion activated materials as luminescence temperature probes [27–33]. In materials doped with TM, luminescence arises from the *d-d* electronic transitions. The *d*-orbitals, unlike the 4*f* orbitals in trivalent lanthanides, are not shielded by the outer orbitals. Consequently, the spectroscopic properties of TM strongly depend on the properties of the containing material and, in particular, the strength of the crystal field that acts on the dopant ion [34–38]. Therefore, both the emission range of luminescence and the rate of temperature quenching of the luminescence can be modulated by changing the type of matrix material used [33,39–44]. Moreover, the high susceptibility of the luminescence intensity to temperature changes enables the development of luminescence thermometers with excellent thermometric performances [45–47]. In addition, TMs have much higher absorption cross-sections than those corresponding to *f-f* transitions of Ln^{3+}, which enables greater luminescence brightness. Due to these advantages, there has been a semi-exponential increase in the number of works published recently related to this type of luminescence thermometry. This research field is dominated by chromium- and manganese-based temperature sensors, which are the focuses of 59 % and 38 % of the literature published in this area, respectively (Fig. 2) (Fig. 2 [27,46,48–53]). Only approximately 4 % of the scientific papers published in this field deal with other TM ions. Recent works clearly confirm that TM-doped materials are characterized by particularly favourable thermometric parameters that enable their use in wide temperature and spectral ranges. Therefore, the aim of this paper is to provide a comprehensive review of the current knowledge about luminescence thermometry based on TM-doped materials.

2. Introduction to the spectroscopy of TM ions

The spectroscopic properties of TM ions have been thoroughly described in previous literature [34,35,37,38]. Hence, this work discusses only the correlations between the host material parameters and spectroscopic properties of TM ions relevant to luminescence thermometry. The *d-d* electronic transitions are responsible for the luminescence properties of TM ions. As the 3*d* orbital is a valence orbital, the energy configuration of an ion at an excited level differs from that at the ground level. Therefore, except in a few cases, the excited level parabola in configuration coordination representation is shifted with respect to the ground level parabola, and the magnitude of this shift depends significantly on the local point symmetry of the TM ion sites in the host material crystal. TM ions preferentially occupy octahedrally and tetrahedrally coordinated crystallographic sites, although the presence of TM ions in perturbed and distorted polyhedra has also been observed (Fig. 3a) [37]. The coordination number and distance between the metal and ligand significantly influence the spectroscopic properties of the TM ions. Due to the complexity of the analysis of the TM ion interaction with each ligand, the concept of superposition of the electrical interactions of all matrix ligands (each ligand treated as a point charge) on the TM ions in the form of the crystal field strength (CFS) was introduced. This approach considerably simplifies the analysis of the spectroscopic properties of TM ions in different matrices and, to some extent, enables the prediction of their spectroscopic properties. The *d* state of a TM localized in an octahedral environment is split into two doubly degenerate states e_g (d_{z2}, d_{x2-y2}) of higher energy and triply degenerate states t_{2g} (d_{xy}, d_{xz}, d_{yz}) of lower energy [34,35,37,38]. In this case, there is a simple correlation between the CFS and the metal–oxygen distance *R*: CFS $\sim R^{-5}$. Based on this relationship, one can predict how changing this parameter will affect the spectroscopic properties of TM ions. An excellent example of this is the spectroscopy of Cr^{3+} ions widely described in the literature [28,39–42]. However, for ions located at tetrahedral positions, such direct correlation is no longer present. One can only determine some general tendencies considering that the splitting strength between the ground and excited levels is much lower than the octahedral coordination and is $\Delta_{tet} = 4/9\Delta_{oct}$. (Fig. 3b) [34,35,37,38]. Additionally, an inversion of energy states will be observed, in that the triply degenerate states t_{2g} (d_{xy}, d_{xz}, d_{yz}) will have higher energy than the doubly degenerate states e_g (d_{z2}, d_{x2-y2}).

This significant change in the energy distance between the excited and ground levels is responsible for the multiphonon relaxation of the excited level in some TM ions. For example, this feature results in the inability to observe the luminescence of Cr^{3+} ions located at tetrahedral crystallographic sites. Any disorder or deformation of the polyhedra results in the occurrence of additional energy level splitting via the Jahn-Teller effect (Fig. 3c) [54,55]. This effect further alters the spectroscopic properties of the TM ions. The strength of the interaction between the crystal field and TM ions affects not only the shape and spectral position of the TM ions bands, but also the thermal dependences of their spectroscopic properties. As will be described in detail in Section 3, the offset of the ground level parabola with respect to the excited level parabola in the wavevector domain results in the intersection of these parabolas. The energy distance between the bottom of the excited level band and the crossover point (also called the activation energy) determines the rate of temperature quenching of TM

Table 1
Electronic configurations of different transition metal ions. Ions used in luminescence thermometry are highlighted in green.

Electronic configuration	Transition metal ions									
$3d^0$	Ti^{4+}	V^{5+}								
$3d^1$	Ti^{3+}	V^{4+}	Cr^{5+}	Mn^{6+}						
$3d^2$	Ti^{2+}	V^{3+}	Cr^{4+}	Mn^{5+}						
$3d^3$		V^{2+}	Cr^{3+}	Mn^{4+}						
$3d^4$			Cr^{2+}	Mn^{3+}						
$3d^5$			Cr^{+}	Mn^{2+}	Fe^{3+}					
$3d^6$				Mn^{+}	Fe^{2+}	Co^{3+}				
$3d^7$						Co^{2+}	Ni^{3+}			
$3d^8$						Co^{+}	Ni^{2+}			
$3d^9$							Ni^{+}	Cu^{2+}		
$3d^{10}$								Cu^{+}		

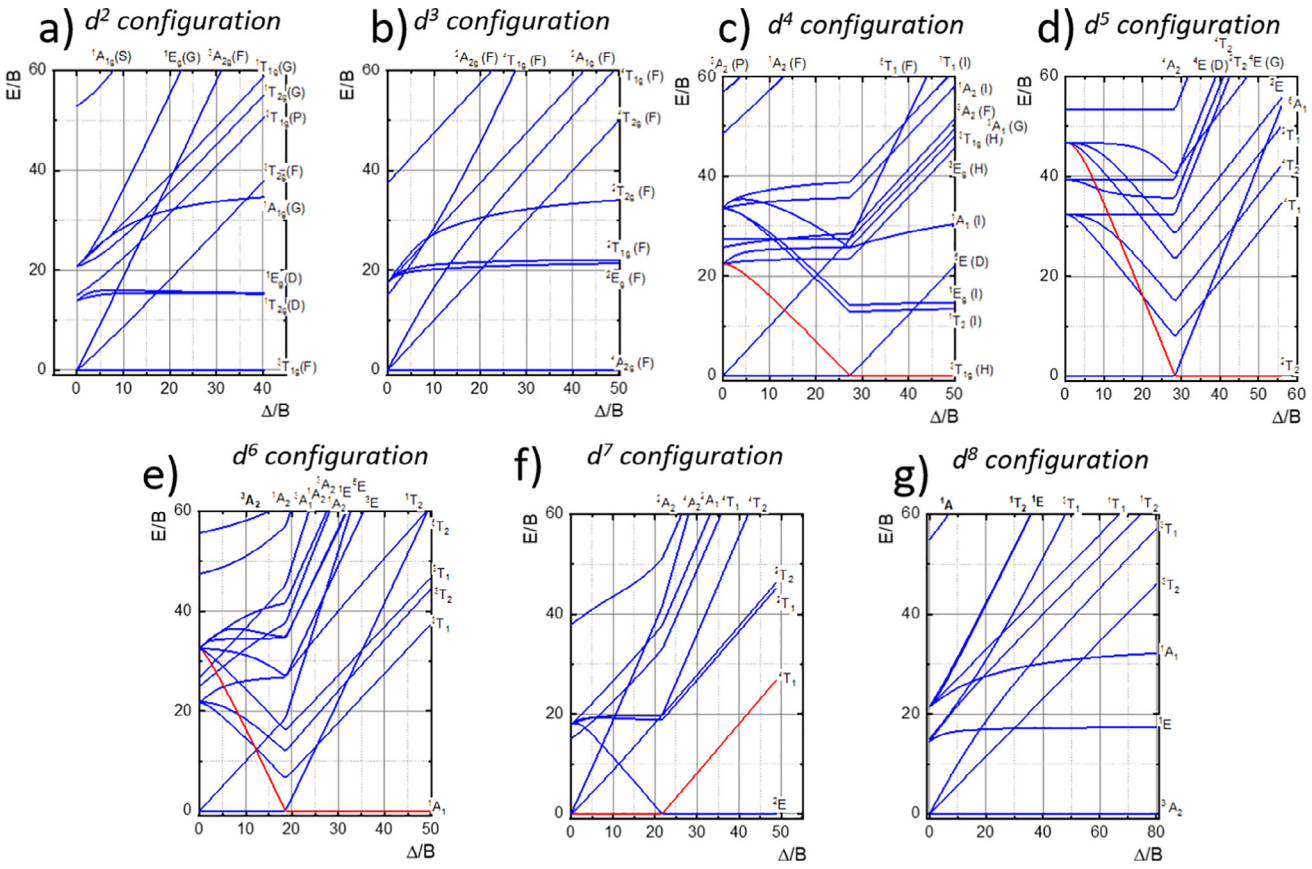

Fig. 4. Tanabe-Sugano diagrams for different electronic configurations of TM ions [56].

ion luminescence. The higher the activation energy, the more stable the TM ion luminescence. Hence, the matrix thermal dynamics plays an important role in the changing luminescence properties of TM ions. The schematic depicting a simplified version of the configurational coordinate diagram for $3d^3$ ions shows that for stronger crystal fields, the shift between parabolas is reduced, resulting in larger activation energies. The energy diagrams of TM ions are predefined by their electron configurations. The relative arrangements of energy levels in the domain of the crystal field parameter (usually normalized with respect to the Racah parameter) for TMs of different electron configurations (see Table 1) were determined in 1970 and are called Tanabe-Sugano diagrams after their authors (Fig. 4)[56]. This qualitative means of describing the relations among the energy levels of TM ions in the octahedral coordination provides a very useful tool for analysing the spectroscopic properties of phosphors doped with these ions. However, even for the tetrahedral coordination, Tanabe-Sugano diagrams can indicate the predicted changes in the relations between the energy levels as the CFS changes.

Table 2
Temperature dependences of radiative and non-radiative rates used in different theoretical models of the transition metal ion luminescence thermal quenching.

Model name	Radiative rate k_R	Non-radiative rate k_{NR}
Mott-Seitz	constant	$k_{NR0} \cdot \exp(-\Delta E/k_B T)$
Multiphonon relaxation model	constant	$k_{NR0} \cdot \left[\frac{\exp(h\nu/k_B T)}{\exp(h\nu/k_B T)-1}\right]^{\frac{\Delta E}{h\nu}}$
Relaxation through the crossover with the excited state, charge transfer band or autoionization	$k_0 \cdot \coth(h\nu/2k_B T)$	$k_{NR0} \cdot \exp(-\Delta E/k_B T)$

3. Temperature dependences of emission intensity and excited state lifetime of TM activated phosphors

When selecting materials for luminescence thermometry, one of the primary considerations is how their emission intensity and lifetime depend on temperature. To answer this question, it is sufficient to know the change of the material quantum efficiency η with temperature. Once optically activated electrons populate a certain excited state, they return to the ground state through either radiative or non-radiative processes with rates of k_R and k_{NR}, respectively. η is defined as the share of radiatively relaxed electrons to the total number of relaxed electrons:

$$\eta = \frac{k_R}{k_R + k_{NR}} \tag{1}$$

The population density $N(t)$ of the excited state in a simple two-state model is.

$$\frac{dN(t)}{dt} = -(k_R + k_{NR})N(t), \tag{2}$$

$$N(t) = N_0 \exp\left[-(k_R + k_{NR})t\right]. \tag{3}$$

The intensity of photoluminescence emission I_{PL} is proportional to the product of the quantum efficiency and state population density as.

$$I_{PL} = C\eta N(t) = C\eta N_0 \exp\left[-(k_R + k_{NR})t\right] \tag{4}$$

where C encapsulates all physical parameters that are characteristic of the measurement system and investigated material. The lifetime of observed excited state τ is defined by.

Table 3
Comparison of the thermometric performance of lifetime-based luminescent thermometers on TM.

TM	Valence	Host	Emitting state	S_R (%/K)	T (S_{RMAX}) (K)	λ_{exc} (nm)	Operating temperature range (K)	Ref
Titanium	3+	$SrTiO_3:Ti^{3+}$	^2E	5.5	290	266	77–350	[45]
		$SrTiO_3:Ti^{3+}$, La^{3+}	^2E	4.2	104	266	77–270	[45]
		$SrTiO_3:Ti^{3+}$, Tb^{3+}	^2E	8.83	180	266	77–240	[45]
		$CaTiO_3:Ti^{3+}$, Yb^{3+}	^{2E}	3.55	295	266	77–480	[68]
	4+	$LiTaO_3:Ti^{4+}$, Eu^{3+}		3.395	303	270	303–443	[66]
Chromium	3+	$Al_2BeO_4:Cr^{3+}$	^2E	1.43	773	543.5	273–773	[193]
		$NaYF_4:Yb^{3+}$/ Er^{3+}, Nd^{3+} + $NaAlSiO_4:Cr^{3+}$	^2E	0.58	410	420	300–575	[194]
		$LiGa_5O_8:Cr^{3+}$	^2E	1.15	350	416	293–563	[102]
		$Bi_2Ga_4O_9$ Cr^{3+}	^2E	3.26	550	600	300–550	[44]
		$Bi_2Al_4O_9$	^2E	0.7	550	600	300–550	[44]
		$LiGa_5O_8:Cr^{3+}$	^2E	0.76	295	406	298–563	[100]
		$Ga_2O_3:Cr^{3+}$	^2E	0.46	370	406	298–563	[100]
		$ZnGa_2O4:Cr^{3+}$	^2E	0.58	420	406	298–563	[100]
		$Al_2O_3:Cr^{3+}$	^2E	0.48	390	514.5	292–923	[195]
		$Al_2O_3:C^{r3+}$	^2E	0.9	450	514.5	292–923	[88]
		CaF_2 glass ceramics O^{2-}enriched	^2E	0.76	498	296	300–500	[103]
		CaF_2 glass ceramics F^- enriched	^2E	0.47	351	464	300–500	[103]
		YF_3 + Ga_2O_3 GC Cr^{3+}	^2E	0.59	386	400	303–563	[96]
		YF_3 Yb^{3+}, Er^{3+}+ $ZnAl_2O_4$: Cr^{3+} glass ceramics	^2E	0.61	410	396	303–563	[49]
		$GdAlO_3$	$^4T_2$			532	473–1473	[50]
		$ZnAl_2O_4:Cr^{3+}$ (in glass-ceramics)	^2E	0.83	603	390	293–573	[118]
		$LiAl_5O_8:Cr^{3+}$	^2E	0.83	447	554	200–600	[99]
		$YAB:Cr^{3+}$	^2E	1.1	273	405	273–373	[105]
		LaF_3 + Ga_2O_3 GC	^2E	0.66	500	400	333–573	[97]
		$LiGa_5O_8$ GC: Cr^{3+}	^2E	0.59	386	980	300–463	[86]
		$ZnGa_2O_4:Cr^{3+}$	^2E	1.15	400	NA	225–670	[196]
		$Al_2O_3:Cr^{3+}$ fiber	^2E				293–2073	[197]
		$LaGaO_3:Cr^{3+}$	^2E	1.38	440	610	300–450	[198]
		$GdAlO_3:Cr^{3+}$	^2E	–	–	532	973–1473	[199]
		$Y_3Al_5O_{12}:Cr^{3+}$	^2E	0.55	384	445	123–573	[98]
		$Y_3Al_3Ga_2O_{12}:Cr^{3+}$	^2E	0.61	368	445	123–573	[98]
		$YAlO_3:Cr^{3+}$	^2E	0.58	302	445	123–573	[98]
		$Gd_3Ga_5O_{12}:Cr^{3+}$	^2E	1.09	249	445	123–573	[98]
		LLGG:Cr^{3+}	^2E	1.13	270	445	123–573	[98]
		$CaF_2:Er^{3+}$ and $ZnAl_2O_4:Cr^{3+}$ multi-phase GC	^2E	0.67	535	396	298–573	[95]
		$SrF_2:Er^{3+}$,Yb^{3+} and $ZnAl_2O_4:Cr^{3+}$GC	^2E	0.19	435	532	298–498	[200]
		$Mg_2SiO_4:Cr^{3+}$	^2E	0.92	240	450	10–330	[31]
		$ZnGa_2O_4:Cr^{3+}$, Bi^{3+}	^2E	1.93	473	430	293–473	[9292]
			persistent lifetime	1.7	463	254	323–473	
		$BaAl_{12}O_{19}:Eu^{2+}$,Cr^{3+}	^2E	0.466	366	325	290–480	[81]
		$Mg_2TiO_4:Cr^{3+}$	^2E	0.75	290	473	100–400	[76]
	4+	ZnO–SrO–SiO_2:Cr^{4+} (in glass-ceramics)	$^3T_1$	1.72	387	396	293–573	[118]
		$Ca_2Al_2SiO_7:Cr^{4+}$	$^3T_1$	0.25	300	730	293–353	[115]
Manganese	2+	$Zn_2SiO_4:Mn^{2+}$	$^4T_1(G)$	1.65	575	370	303–573	[129]
		Ca_8BaCe-$(PO_4)_7:Mn^{2+}$	$^4T_1(G)$	5.14	573	315	300–560	[201]
		$ZnGa_2O_4:Mn^{2+}$ Nanoglass	$^4T_1(G)$	2.51	523	304	323–523	[202]
		$Zn2GeO_4:Mn^{2+}$	Decay profile	4.5	360	355	250–420	[203]
		$Zn2GeO_4:Mn^{2+}$	intensity ratio of two frames)	12.2	370	355	250–420	[203]
	3+	$Y_3Al_5O_{12}$: Mn^{3+}	$^5T_2$	2.63	350	266	123–400	[139]
	4+	$BaAl_{12}O_{19}:Mn^{4+}$:$SrAl_{12}O_{19}$	^2E	4.48	353	370	293–393	[131]
		$Li_2TiO_3:Mn^{4+}$	^2E	3.21	~325	480	10–350	[162]
		$Y_2MgTiO_6:Mn^{4+}$	^2E	0.14	153	365	10–513	[144]
		$CaGdMgSbO_6:Mn^{4+}$, Sm^{3+}	^2E	1.23	523	406	300–570	[204]
		$Lu_3Al_5O_{12}:Mn^{4+}$	^2E	6.35	345	355	307–383 K	[46]
		$Li_{1.8}Na_{0.2}TiO_3:Mn^{4+}$	^2E	2.27	330	490	10–350	[161]
		$YAlO_3$: Yb^{3+},Er^{3+},Mn^{4+}	^2E	1.19	525	980	303–560	[205]
		$YAlO_3$: Yb^{3+} Mn^{4+} Ho^{3+}	^2E	1.13	525	980	303–560	[205]
		$Gd_3Al_5O_{12}:Mn^{4+}$, Mn^{3+}	dec ^2E	2.08	249	266	123–573	[3333]
		$Gd_3Al_5O_{12}:Mn^{4+}$, Mn^{3+}	rise ^2E	0.99	390	266	123–573	
		$Gd_3Ga_5O_{12}$ Mn^{4+}, Mn^{3+}	dec ^2E	1.66	154	266	123–573	[3333]
		$Gd_3Ga_5O_{12}$ Mn^{4+}, Mn^{3+}	rise ^2E	3.58	210	266	123–573	
		$Lu_3Al_5O_{12}:Mn^{4+}$, Mn^{3+}	dec ^2E	0.72	320	266	123–573	[3333]
		$Lu_3Al_5O_{12}:Mn^{4+}$, Mn^{3+}	rise ^2E	1	383	266	123–573	
		$YAlO_3$ Mn^{4+}, Mn^{3+}	dec ^2E	0.76	360	266	123–573	[3333]
		$YAlO_3$ Mn^{4+}, Mn^{3+}	rise ^2E	2.36	514	266	123–573	
		$Y_3Al_5O_{12}:Mn^{4+}$, Mn^{3+}	dec ^2E	1.27	330	266	123–573	[3333]
		$Y_3Al_5O_{12}:Mn^{4+}$, Mn^{3+}	rise ^2E	3.34	425	266	123–573	
		$Li_4Ti_5O_{12}$ Mn^{4+}	^2E	2.6	330	500	10–350	[168]
		$Ca_3Ga_2Ge_3O_{12}:Mn^{3+}$,$Mn^{4+}$	rise ^2E	6	33	532	4.5–300	[140]
		$LaTiSbO_6:Mn^{4+}$	^2E	2.75	383	340	298–418	[153]

Table 3 (*continued*)

TM	Valence	Host	Emitting state	S_R (%/K)	T (S_{RMAX}) (K)	λ_{exc} (nm)	Operating temperature range (K)	Ref
		$MgTiO_3:Mn^{4+}$	^2E	4.1	277	550	198–323	[169]
		$Ca_2GdSbO_6:Mn^{4+}$, Eu^{3+}	^2E	1.47	425	393	303–503	[206]
		$Y_2O_3:Ho^{3+}$ and $Mg_2TiO_4:Mn^{4+}$ powders	^2E	0.9	373 K	465	198–373 K	[169]
		Li_2TiO_3: Mn^{4+} and Y_2O_3: Dy^{3+}	^2E	6.67	339	355	273–373	[170]
		$BaLaCa_{0.9}Mg_{0.1}SbO_6:Mn^{4+}$	^2E	1.05	473	340	77–503	[207]
		$BaLaCaSbO_6:Mn^{4+}$	^2E	1.09	503	340	77–503	[207]
		$BaLaCa_{0.1}Mg_{0.9}SbO_6:Mn^{4+}$	^2E	1.42	488	340	77–503	[207]
		$BaLaMgNbO_6:Mn^{4+}$, Dy^{3+}	^2E	2.43	437	355	230–470	[167]
		$Li_2TiO_3:Mn^{4+}$	^2E	3.21	~325 K	480	10–350	[162]
		$SrTiO_3:Mn^{4+}$	^2E	3.5	348	400	123–363	[47]
		$SrTiO_3:Mn^{4+}$,Lu^{3+}	^2E	3.87	290	400	77–450	[160]
		$SrTiO_3:Mn^{4+}$,Er^{3+}	^2E	5.1	290	400	77–450	[160]
		$SrGdLiTeO_6$: Mn^{4+},Eu^{3+}	^2E	0.229	573	302	298–573	[208]
		$Mg_4FGeO_6:Mn^{4+}$	Rise ^2E	0.289	473	385	293–623	[163]
		$Lu_3Al_5O_{12}:Ce^{3+}$, Mn^{4+}	^2E	3.22	350	348	100–350	[154]
		$ZnGa_2O_4:Cr^{3+}$,Bi^{3+}	Persistent ^2E	1.7	473	430	323–473	[92]
		$ZnGa_2O_4:Cr^{3+}$,Bi^{3+}	^2E	1.93	473	430	323–473	[92]
		$BaLaMgNbO_6:Mn^{4+}$, Dy^{3+}	^2E	2.43	437	355	230–470	[167]
	5+	$Ba_3(PO_4)_2:Mn^{5+}$.	1E	1	443	668	123–573	[173]
Iron	3+	$BaAl_4O_7:Fe^{3+}$	4 T1	3.52	180	266	123–583	[174]
Copper	2+	$EtNC(S)PPh_2NPPh_2C(S)NEt^-$,	S1	0.5	310	365	228–353	[184]

$$\tau = \frac{1}{k_R + k_{NR}}, \tag{5}$$

and the radiative lifetime is.

$$\tau_R = \frac{1}{k_R}. \tag{6}$$

Meanwhile, for phosphors activated by trivalent lanthanides, it is generally assumed that the radiative rate is temperature independent (k_R = const.) [18], in the case of TM ions, both k_R and k_{NR} vary with temperature. For clarity, we will designate as the 'temperature dependence' the effect that arises from the temperature dependences of both k_R and k_{NR}, whereas the term 'temperature quenching' (TQ) will be used to describe the effects due to the change in only the non-radiative relaxation rate. The most frequently used theoretical models are presented in Table 2 and illustrated in Fig. 5.

3.1. Temperature dependence of radiative relaxation rate

The radiative relaxation rate k_R exhibits temperature dependence in the case of transitions that are electron dipole-forbidden but are made partially allowed by coupling to the lattice asymmetric vibrations that induce odd-parity crystal field components. This behaviour is especially the case for TMs with the $3d^3$ electronic configuration in strong crystal fields of octahedral symmetry, such as Mn^{4+} in oxides in fluorides. The radiative rate, in this case, can be written as.

$$k_R = k_S + k_{AS}, \tag{7}$$

where k_S and k_{AS} represent the Stokes and anti-Stokes transition rates, respectively. These rates are proportional to the occupation of corresponding phonon modes n, so one can write.

$$k_{AS} = k_R(0)[n], \tag{8}$$

$$k_S = k_R(0)[n+1], \tag{9}$$

which leads to.

$$k_R = k_R(0)[2n+1]. \tag{10}$$

If one considers the coupling with a phonon mode of energy $h\nu$ at temperature T, then the occupation number n is.

$$n = \frac{1}{\exp(h\nu/k_BT) - 1}, \tag{11}$$

where $k_B = 0.695\ cm^{-1}K^{-1}$ is the Boltzmann constant. Finally, the radiative relaxation rate and radiative lifetime τ_R as functions of T can be written as.

$$\frac{1}{k_R(T)} = \tau_R(T) = \tau_0 \cdot \tanh\left(\frac{h\nu}{2k_BT}\right), \tag{12}$$

where $\tau_0 = 1/k_{R0}$is the radiative lifetime (1/radiative rate) at T = 0 K. The photoluminescence emission intensity is proportional to the number of occupied phonon modes and with the assumption that $k_{NR} \ll k_R$ ($\eta \approx 1$) can be described by (I_0– the emission intensity at 0 K) [57]:

$$I_{PL}(T) = I_0 \cdot \coth\left(\frac{h\nu}{2k_BT}\right). \tag{13}$$

3.2. Thermal quenching of luminescence

The thermal quenching of luminescence occurs when a non-radiative channel opens for the relaxation of optically excited electrons due to an increase in temperature. This behaviour leads to an increase in k_{NR} and, hence, emission intensity weakening and lifetime shortening.

The Mott-Seitz model is built on a configuration coordinate model that consists of two parabolas shifted with respect to each other (Fig. 5a) [58]. These parabolas represent potential curves, each of which indicates the total energy of the system in its ground or excited state as a function of the configurational coordinate R. Based on this model, an electron in the excited state, assisted by thermal energy, nonradiatively deexcites to the ground state through the parabola intersection point S with the temperature dependent rate [59]:

$$k_{NR}(T) = k_{NR0} \cdot \exp(-\Delta E/k_BT),$$

$$\tau_{NR}(T) = \tau_{NR0} \cdot \exp(\Delta E/k_BT), \tag{14}$$

Table 4
Comparison of the thermometric performance of TM based ratiometric luminescent thermometers.

TM	Valence	Host	LIR	S_R (%/K)	T (S_{RMAX}) (K)	λ_{exc} (nm)	Operating temperature range (K)	Reference
Titanium	3+	YAG:Ti^{3+},Ti^{4+}	Ti^{3+}/ Ti^{4+}	0.7	489	266	123–573	[64]
	4+	YAG:Ti^{3+},Ti4 + Nd^{3+}	Ti^{4+}/ Nd^{3+}	3.7	473	266	123–573	[64]
		YAG:Ti^{3+}, Ti^{4+}, Eu^{3+}	Eu^{3+}/ Ti^{4+}	2.2	323	266	123–573	[64]
		YAG:Ti^{3+},Ti^{4+}, Dy^{3+}	Dy^{3+} /Ti^{4+}	2.2	323	266	123–573	[64]
		YAG:Ti^{3+},Ti^{4+}	Ti^{3+}/ Ti^{4+}	0.7	523	266	123–573	[64]
		ZrO_2:Ti^{4+}, Eu^{3+}	Ti^{4+}/ Eu^{3+}	3.91	410	280	303–413	[67]
		$LiTaO_3$:Ti^{4+}, Eu^{3+}	Ti^{4+}/ Eu^{3+}	5.425	303 K	270	303–443	[66]
		$Ca_{14}Al_{10-x-y}Zn_6O_{35}$:x$Ti^{4+}$,y$Mn^{4+}$	Ti^{4+}/ Mn^{4+}	0.57	453	260	303–523	[209]
Vanadium	3+	$LaGaO_3$:V, Nd^{3+}	V^{3+}/ Nd^{3+}	1.44	448	266	123–573	[70]
		YAG:V^{3+}, V^{5+}, Eu^{3+}	V^{3+}/ Eu^{3+}	0.4	373	266	123–573	[32]
		YAG:V^{3+}, V^{5+}, Dy^{3+}	V^{3+}/ Dy^{3+}	4	123	266	123–573	[32]
		YAG:V^{3+}, V^{5+}, Nd^{3+}	V^{3+}/ Nd^{3+}	0.8	573	266	123–573	[32]
		YAG: V^{5+}, V^{3+}	V^{5+}/ V^{3+}	6	573	266	123–573	[32]
	4+	$Y_3Al_3Ga_2O_{12}$:V^{5+}, V^{4+}	V^{4+}/V^{5+}	1.68	273	266	123–573	[210]
		$Y_3Al_2Ga_3O_{12}$:V^{5+}, V^{4+}	V^{4+}/ V^{5+}	2.67	273	266	123–573	[210]
		$Y_3AlGa_4O_{12}$:V^{5+}, V^{4+}	V^{4+}/ V^{5+}	2.52	253	266	123–573	[210]
		$Y_3Ga_5O_{12}$:V^{5+}, V^{4+}	V^{4+}/V^{5+}	2.48	173	266	123–573	[210]
		$LaGaO_3$:V, Nd^{3+}	V^{4+}/ Nd^{3+}	0.49	253	266	123–573	[70]
	5+	$LaGaO_3$:V, Nd^{3+}	V^{5+}/ Nd^{3+}	1	268	266	123–573	[70]
		YAG: V^{5+}, V^{3+}	V^{5+}/ V^{3+}	6	573	266	123–573	[32]
		$Y_3Al_3Ga_2O_{12}$:V^{5+}, V^{4+}	V^{4+}/ V^{5+}	1.68	273	266	123–573	[69]
		$Y_3Al_2Ga_3O_{12}$:V^{5+}, V^{4+}	V^{4+}/ V^{5+}	2.67	273	266	123–573	[69]
		$Y_3AlGa_4O_{12}$:V^{5+}, V^{4+}	V^{4+}/ V^{5+}	2.52	253	266	123–573	[69]
		$Y_3Ga_5O_{12}$:V^{5+}, V^{4+}	V^{4+}/ V^{5+}	2.48	173	266	123–573	[69]
		YVO_4:Er^{3+}	V^{5+}/Er^{3+}	1.58	300	300	299–466	[71]
Chromium	3+	$Y_3Al_5O_{12}$:RE/TM	Dy^{3+}/ Cr^{3+}	2.32	450	384	293–573	[80]
		$Y_3Al_5O_{12}$:RE/TM	Eu^{3+}/ Cr^{3+}	2.43	573	393	293–573	[80]
		$LiLaP_4O_{12}$:Cr^{3+}, Nd^{3+}	Nd^{3+}/ Cr^{3+}	4.89	323	665	123–473	[77]
		$NaYF_4$:Yb^{3+}/RE^{3+} (RE^{3+} = Er^{3+}, Nd^{3+}) and $NaAlSiO_4$:Cr^{3+}	Cr^{3+}/ Nd^{3+}	2.25	385	420	300–575	[194]
		$Bi_2Al_4O_9$:Cr^{3+}	$^2E/^4T_2$	1.24	290	570	100–600	[117]
		EuF_3 + Ga_2O_3 Eu^{2+} Cr^{3+} glass ceramics	Eu^{2+}/ Cr^{3+}	0.8	NA	375	303–573	[211]
		Dual Phase glass ceramics	Cr^{3+}/ Eu^{3+}	SA = 15	463	396	300–573	[212]
		Dual Phase glass ceramics	Cr^{3+}, Dy^{3+}	SA = 16	428	386	300–573	[212]
		Dual Phase glass ceramics	Cr^{3+}/ Tb^{3+}	SA = 22	423	377	300–573	[212]
		GdP_5O_{14}: Cr^{3+}, Nd^{3+}	Cr^{3+} /Nd^{3+}	0.4	573	460	123–573	[213]
		Mg_2TiO_4:Cr^{3+}	$^2E/^4T_2$	1.73	300	473	100–400	[76]
		$LiLaP_4O_{12}$: Cr^{3+}, Yb^{3+}	Cr^{3+} /Yb^{3+}	1.2	450	650/ 920	77–450	[78]
		YAG Cr^{3+}, Nd^{3+}	Cr^{3+}/Nd^{3+}	3.48	200	590	100–850	[79]
		YAP:Cr^{3+}	Two colour excitation	0.37	123		123–573	[87]
		YAG:Cr^{3+}	Two colour excitation	0.175	123		123–573	[87]
		$LiLaP_4O_{12}$:Cr^{3+}	Two colour excitation	0.3	123		123–473	[87]
		$CaHfO_3$:Cr^{3+}	$^2E/^4T_2$	2	40	450	40–150	[75]
		$GdVO_4$:Eu^{3+} and Al_2O_3:Cr^{3+} hybrid particles	Eu^{3+} /Cr^{3+}	2.6	675	405	303–753	[83]
		$Bi_2Ga_4O_9$:Cr^{3+}	R_1 /R_2	2.74	80	442	77–450	[214]
		$Sr_2MgAl_{22}O_{36}$:Cr^{3+}	$^2E/^4T_2$	1.7	310	410	298–523	[215]
		$ZnGa_2O_4$:Cr^{3+}	$^2E/^4T_2$	2.8	310	405	100–800	[73]
		$LiGa_5O_8$ GC:Er^{3+}, Cr^{3+}	Cr^{3+}/ Er^{3+}	0.35	343	980	300–500	[86]
		$LiGa_5O_8$ GC:Ho^{3+}, Cr^{3+}	Cr^{3+}/ Ho^{3+}	0.25	348	980	300–500	[86]
		$Zn_2Ga_{3.98-4x/3}Ge_xO_8$:$Cr^{3+}_{0.02}$	$^2E/^4T_2$	1	295	254	295–328	[216]
		$ZnAl_2O_4$:Cr^{3+}, Mn^{2+}	R_1 /R_2	3.6	77	427	77–310	[74]
		$Gd_3Al_5O_{12}$	Cr^{3+}/ Nd^{3+}	1.2	123	445	123–573	[40]
		$Gd_3Al_4GaO_{12}$	Cr^{3+}/ Nd^{3+}	1.42	123	445	123–573	[40]
		$Gd_3Al_3Al_2O_{12}$	Cr^{3+}/ Nd^{3+}	1.55	123	445	123–573	[40]
		$Gd_3Al_2Ga_4O_{12}$	Cr^{3+}/Nd^{3+}	1.6	123	445	123–573	[40]
		$Gd_3Ga_5O_{12}$	Cr^{3+}/ Nd^{3+}	1.9	123	445	123–573	[40]
		$Bi_2Ga_4O_9$:Cr^{3+}	$^2E/^4T_2$	S_a = 0.28 K^{-1}	300	442	10–500	[27]
		Mg_2SiO_4:Cr^{3+}	$^2E/^4T_2$	0.7	310	450	10–330	[31]
		$ZnAl_2O_4$:Cr^{3+}, Bi^{3+}	persistent LIR	0.11–0.14	293–373	254	293–373	[92]
		ZrB_2/Al_2O_3:Cr^{3+}, Nd^{3+}	Cr^{3+}/ Nd^{3+}	2	623	445	123–773	[217]
		$Lu_3(BO_3)_4$:Cr^{3+}	$^2E/^4T_2$	0.42	423	450	303–473	[39]
		$Gd_3(BO_3)_4$:Cr^{3+}	$^2E/^4T_2$	0.27	423	450	303–473	[39]
		α-Ga_2O_3	$^2E/^4T_2$	1.05	300	455	200–450	[28]
		β-Ga_2O_3	$^2E/^4T_2$	0.64	300	455	200–450	[28]
		$MgAl_2O_4$:Cr^{3+}	$^2E/^4T_2$	3.5	300	550	300–550	[29]
		$LiAl_5O_8$: Cr^{3+} and $LuPO_4$: Tb^{3+}	Cr^{3+}/ Tb^{3+}	3.68	300	543.8	300–600	[85]
		YAG:Cr^{3+}, Dy^{3+}	Cr^{3+}/ Dy^{3+}	0.64	175	484	175–650	[82]

Table 4 (*continued*)

TM	Valence	Host	LIR	S_R (%/K)	T (S_{RMAX}) (K)	λ_{exc} (nm)	Operating temperature range (K)	Reference
		YAG:Cr^{3+}, Dy^{3+}	^2E /$^4T_2$	2.2	200	484	175–650	[82]
		$MgTiO_3$:Cr^{3+}	^2E /defect	2.62	310	385	100–350	[30]
		Al_2O_3:Cr^{3+}	R_1/ R_2	4.8	20	473	10–540	[88]
		$La_2LuGa_5O_{12}$:1%Cr^{3+},5%Nd^{3+}	Cr^{3+}/Nd^{3+}	1.47	260	445	123–573	[41]
Manganese	2+	GdF_3: Ce^{3+}, Mn^{3+}, Eu^{3+}	Mn^{2+}, Eu^{3+}	1.32	340	254	298–433	[124]
		Zn_2SiO_4:Mn^{2+}	Mn^{2+}/ defects	6.5	573	370	303–573	[129]
		$NaBa_{0.6}Sr_{0.4}B$:0.03Ce^{3+},0.03Mn^{2+}	Ce^{3+} /Mn^{2+}	0.83	323	297	323–523	[218]
		Zn_2GeO_4:Mn^{2+}, Eu^{3+}	Mn^{4+} /Eu^{3+}	1.96	353	315	293–353	[123]
		Ga_2O_3:Mn^{2+}+ GdF_3:Tm^{3+}	Mn^{2+} /Tm^{3+}	1.78	543	360	123–663	[137]
		$Ba_{0.5}Sr_{0.5}Al_{11.93}O_{19}$: Mn^{2+}, Mn^{4+}	Mn^{2+}/ Mn^{4+}	4.37	293	370	293–406	[131]
		$CsPb(Cl/Br)_3$	Mn^{2+} / exciton	10.04	143	365	83–143	[219]
		$(Ca,Sr)_{10}Li(PO_4)_7$:Ce^{3+},Mn^{2+}	Mn^{2+} /Ce^{3+}	0.4	4.73	310	293–473	[124]
		Zn_2SiO_4:Mn^{2+}	Mn^{2+} / host	12.2		310	293–573	[129]
		$Ca_8BaCe(PO_4)_7$:Mn^{2+}	Mn^{2+}/Ce^{3+}	2.17	573	315	300–560	[201]
		$Ca_9La(PO_4)_5SiO_4F_2$:Ce^{3+}, Tb^{3+}, Mn^{2+}	Ce^{3+}/ Mn^{2+}	0.28	520	300	303–523	[220]
		$Ca_2Sr(PO_4)_2$ Eu^{2+} Mn^{2+}	Mn^{2+}/ Eu^{2+}	0.099	463	303	290–460	[221]
		$Ca_9Tb(PO_4)_5(SiO_4)F_2$:Mn^{2+}	Mn^{2+}/ Tb^{3+}	1.92	423	377	298–573	[222]
		MOF Eu-BTC (BTC = 1,3,5-benzenetricarboxylic acid) + Zn_2GeO_4:Mn^{2+}	Eu^{3+}/Mn^{2+}	4.1	318	313	293–363	[223]
		Zn_2SiO_4:Mn^{2+}-Gd_2O_3:Eu^{3+}	Eu^{3+}/ Mn^{2+}	3.05	303	260	300–620	[138]
		$ZnGa_2O_4$:Mn^{2+},Mn^{4+}	Mn^{2+}/ Mn^{4+}	4.345	350	340	100–475	[52]
		$Sr_3Ce(PO_4)_3$:Tb^{3+}, Mn^{2+}	Mn^{2+}/ Tb^{3+}	0.612	298	280	300–570	[224]
		$Ca_8Al_2(PO_4)_6(SiO_4)$:Ce^{3+}, Mn^{2+}	Ce^{3+}/ Mn^{2+}	2.1	~390	254	300–525	[225]
		$Ca_9Y(PO_4)_7$:Ce^{3+},Mn^{2+} and g-C_3N_4 composite	Ce^{3+}/ Mn^{2+}	1.673	547	318	300–550	[136]
		$Li_5Zn_8Al_5Ge_9O_{36}$ Mn^{2+} Mn^{2+}	Mn^{2+}/ Mn^{2+}	8.489	323	254	298–523	[226]
		$Na_3Sc_2P_3O_{12}$: Eu^{2+}, Mn^{2+}	Eu^{2+}/ Mn^{2+}	1.556	473	340	293–473	[134]
		$LaMg_{1-x}Al_{11-y}O_{19}$ (M = Mg, Zn)	Mn^{2+}/ Mn^{4+}	1.5	198	365	100–550	[133]
		$LaZn_{1-x}Al_{11-y}O_{19}$ (M = Mg, Zn)	Mn^{2+}/ Mn^{4+}	9	98	365	100–550	[133]
		$GdPO_4$:Mn^{2+}, Eu^{3+}	Mn^{2+}/ Eu^{3+}	8.88	305	375	303–323	[227]
		$BaAl_{12}O_{19}$:Mn^{4+}:$SrAl_{12}O_{19}$	Mn^{2+}/Mn^{4+}	4.37	293 K	426	293–406	[131]
		$K_7ZnSc_2B_{15}O_{30}$:Mn^{2+}	Mn^{2+}/ Mn^{2+}	1.84	520	410	300–520	[125]
		$ZnGa_{2-y}Al_yO_4$:Mn^{2+},Mn^{4+}	Mn^{4+}/ Mn^{2+}	4.345	350	340	100–375	[52]
	3+	YAG:Mn^{3+},Mn^{4+}	Mn^{3+}/Mn^{4+}	1.6	220	266	123–603	[139]
		$La_2Zr_2O_7$:Tb^{3+},Mn^{3+}	Tb^{3+},Mn^{3+}	1.82	298	240	98–338	[141]
	4+	GdF_3 and Ga_2O_3 nano-crystals glass ceramic	Tm^{3+} /Mn^{4+}	0.28	353 K	360	123–663	[137]
		$BaAl_{12}O_{19}$:Mn^{4+}:$SrAl_{12}O_{19}$	Mn^{2+}/Mn^{4+}	4.37	293 K	426	293–406 K	[131]
		$Ca_{14}Al_{10}Zn_6O_{35}$:Bi^{3+},Mn^{4+}	Bi^{3+} /Mn^{4+}	1.21	523	340	303–563	[158]
		$Mg_{28}Ge_{7.55-x}Ga_xO_{32}F_{15.04}$:$Mn^{4+}$	antiStokes/ Stokes	0.42	303	410	303–473	[145]
		$Mg_{28}Ge_{7.55-x}Ga_xO_{32}F_{15.04}$:$Mn^{4+}$	antiStokes/ Stokes	0.68	303	460	303–473	[145]
		Ba_2LaNbO_6:Mn^{4+},Eu^{3+}	Mn^{4+} /Eu^{3+}	2.08	398	396	300–500	[228228]
		Ca_2LaNbO_6:Mn^{4+},Eu^{3+}	Mn^{4+} /Eu^{3+}	1.51	398	396	298–498	
		$Y_3Al_5O_{12}$:RE/TM	Eu^{3+} /Mn^{4+}	4.81	320	393	293–393	[80]v
		Y_2MgTiO_6:Mn^{4+}	antiStokes/ Stokes	0.14	153	365	10–513	[144]
		$Y_3Al_5O_{12}$: Tb^{3+} /Mn^{4+}	Tb^{3+} /Mn^{4+}	3.73	320	378	293–393	[80]
		$Y_3Al_5O_{12}$: Dy^{3+} /Mn^{4+}	Dy^{3+} /Mn^{4+}	3.16	320	365	293–393	[80]
		$Y_3Al_5O_{12}$: Sm^{3+} /Mn^{4+}	Sm^{3+} /Mn^{4+}	1.53	473	406	293–393	[80]
		$MgTiO_4$:Mn^{4+} +Y_2O_3:Ho^{3+}	Ho^{3+} /Mn^{4+}	4.34	288	355	273–373	[170]
		$Lu_3Al_5O_{12}$:Ce^{3+}, Mn^{4+}	Mn^{4+} /Ce^{3+}	4.37	350	348	100–350	[154]
		Ca_2GdSbO_6:Mn^{4+}, Eu^{3+}	Mn^{4+} /Eu^{3+}	1.38	420	393	303–503	[206]
		Ca_2GdSbO_6:Mn^{4+}, Eu^{3+}	Mn^{4+} /Sm^{3+}	1.55	430	404	303–503	[206]
		SrLaLiTeO$_6$:Mn^{4+},Dy^{3+}	Mn^{4+} /Dy^{3+}	1.6	673	351	298–683	[51]
		Carbon Dot-Grafted $CaAl_{12}O_{19}$:Mn^{4+}	Mn^{4+} /CDs	0.18	300	365	50–300	[229]
		$Mg_{14}Ge_5O_{24}$:Mn^{4+}	anti-Stokes /Stokes	2.71	97	440	6.9–303	[150]
		YAP:Yb^{3+}, Er^{3+}, Mn^{4+}	Mn^{4+} /Er^{3+}	1.95	530	980	293–563	[205]
		YAP:Yb^{3+}, Mn^{4+} Ho^{3+}	Mn^{4+} /Ho^{3+}	1.17	450	980	290–570	[205]
		$Cs_2WO_2F_4$:Mn^{4+}	Stokes / anitstokes	0.21	167	488	10–433	[147]
		$MgTiO_3$:Mn^{4+}	R_1/R_2	0.9	93	550	23–373	[171]
		$MgTiO_3$:Mn^{4+}	^2E / $^4T_2$	1.2	93	550	73–323	[171]
		Gd_2ZnTiO_6: Bi^{3+}, Mn^{4+}	Bi^{3+} /Mn^{4+}	2.4	423	375	313–473	[159]
		$Ba_{0.75}Al_{11}O_{17.25}$–$BaMgAl_{10}O_{17}$ Mn^{2+}, Mn^{4+}	Mn^{4+}/Mn^{2+}	1.63	453	315	310–450	[230]
		$Ca_{14}Al_{10-x-y}Zn_6O_{35}$:x$Ti^{4+}$,y$Mn^{4+}$	Ti^{4+}/ Mn^{4+}	0.57	523	260	303–523	[209]
		$NaLaMgWO_6$ Mn^{4+}, Eu^{3+}	Mn^{4+}/ Eu^{3+}	0.86	523	320	303–525	[231]
		La_2LiSbO_6 Mn^{4+}, Eu^{3+}	Mn^{4+}/ Eu^{3+}	0.891	523	282	303–523	[152]

(*continued on next page*)

Table 4 (*continued*)

TM	Valence	Host	LIR	S_R (%/K)	T (S_{RMAX}) (K)	λ_{exc} (nm)	Operating temperature range (K)	Reference
		Y_2O_3:Ho^{3+} and Mg_2TiO_4:Mn^{4+} powders	Ho^{3+}/ Mn^{4+}	4.6	298–373	465	298–373	[169]
		LuAG:Mn^{4+}, Tb^{3+}	Mn^{4+}/ Tb^{3+}	4.3	333	355	270–420	[155]
		Li_2TiO_3: Mn^{4+} and Y_2O_3: Dy^{3+}	Mn^{4+} /Dy^{3+}	4.34	288	355	273–373	[170]
		$BaLaMgNbO_6$:Mn^{4+}, Dy^{3+}	Dy^{3+} /Mn^{4+}	1.82	457	355	230–470	[167]
		$NaMgBO_3$: Ce^{3+}, Mn^{2+}	Ce^{3+}, Mn^{2+}	0.69	473	375	298–473	[126]
		$Y_3Al_5O_{12}$:Mn^{3+},Mn^{4+},Nd^{3+}	Mn^{4+} /Nd^{3+}	1.69	220	355	90–800	[139]
		$Sr_4Al_{14}O_{25}$:Mn^{4+},Tb^{3+}	Mn^{4+} /Tb^{3+}	2.8	423	266	123–573	[53]
		$SrTiO_3$:Mn^{4+}	$^2E/^4T_2$	4.5	253	387	123–365	[47]
		$SrAl_{12}O_{19}$:Mn^{4+}	antiStokes / Stokes	0.27	393	397	293–393	[146]
		$ZnGa_{2-y}Al_yO_4$:Mn^{2+},Mn^{4+}	Mn^{4+}/ Mn^{2+}	4.345	350	340	100–375	[52]
		$Mg_3Y_2Ge_3O_{12}$: Eu^{3+},Mn^{4+}	antiStokes/ Stokes	0.014	200	420	7–300	[232]
		$Mg_3Eu_2Ge_3O_{12}$: Mn^{4+}	antiStokes/ Stokes	0.019	300	420	7–300	[232]
		$MgTiO_4$:Mn^{4+} +Y_2O_3:Ho^{3+}	Mn^{4+}/Ho^{3+}	4.61	293–373	465	293–373	[169]
		$Lu_3Al_5O_{12}$:Eu^{3+}, Mn^{4+}	Eu^{3+}/ Mn^{4+}	0.7	303	393	303–358	[151]
		SrGdLiTeO$_6$: Mn^{4+},Eu^{3+}	Eu^{3+}/ Mn^{4+}	4.9	550	302	300–550	[208]
	5+	BaPOMn consisting of 3:1 $Ba_3(PO_4)_2$ and $Ba_5(PO_4)_3OH$: Mn^{5+}	Mn^{5+} vibronic sideband	0.43	423	808	283–423	[172]
iron	3+	$Lu_3Ga_5O_{12}$: Fe^{3+},Cr^{3+},Nd^{3+}	Fe^{3+}/ Nd^{3+}	5.9	373	266	123–573	[176]
		Y3Ga_5O_{12}: Fe^{3+},Cr^{3+},Nd^{3+}	Fe^{3+}/ Nd^{3+}	1.68	323	266	123–573	[176]
		$Gd_3Ga_5O_{12}$: Fe^{3+},Cr^{3+},Nd^{3+}	Fe^{3+}/ Nd^{3+}	1.57	323	266	123–573	[176]
		$BaAl_4O_7$:Fe^{3+},Tb^{3+}	Fe^{3+}/Tb^{3+}	1.56	143	266	123–573	[174]
		$BaAl_4O_7$:Fe^{3+}	Fe^{3+}/Fe^{3+}	3.52	180	266	123–593	[174]
		$CaAl_4O_7$:Fe^{3+},Tb^{3+}	Fe^{3+}/Tb^{3+}	2.08	373	266	123–473	[174]
		$CaGa_2O_4$:Fe^{3+}, Tb^{3+}	Fe^{3+}/Tb^{3+}	2.02	279	266	123–423	[175]
		$MgAl_2O_4$:Fe^{3+}, Tb^{3+}	Fe^{3+}/Tb^{3+}	0.74	573	266	123–583	[175]
		$MgGa_2O_4$:Fe^{3+}, Tb^{3+}	Fe^{3+}/Tb^{3+}	0.27	433	266	123–583	[175]
		$CaAl_2O_4$:Fe^{3+}, Tb^{3+}	Fe^{3+}/Tb^{3+}	2.58	283	266	123–383	[175]
		$LiAl_5O_8$:Fe^{3+}, Nd^{3+}	Fe^{3+} /Nd^{3+}	0.56	193	266	123–573	[177]
Cobalt	2+	$MgAl_2O_4$:Co^{2+}, Nd^{3+}	Co^{2+}/Nd^{3+}	0.28	223	266	163–373 K	[178]
Copper	2+	Cu_6-Cu_2-Cu_6 [$Cu_6L_3(Cu_2I_2)Cu_6L_3$] (H_2L = 3,5-bis((3,5-dimethyl-pyrazol-4-yl)methyl)-2,6- dimethylpyridine, Cu_2I_2= (2,6-lutidine)$_2$)	Cu^{2+}/Cu^{2+}	0.285	260	310	100–450	[185]
Nickel	2+	$SrTiO_3$: Ni^{2+}, Er^{3+}	Ni^{2+} /Er^{3+}	0.44	303	450	203–483	[179]
		$CaTiO_3$: Ni^{2+}, Er^{3+}	Ni^{2+}/ Er^{3+}	0.37	303	450	203–483	[179]
		$SrTiO_3$:Ni^{2+}, Er^{3+} microcrystals	Ni^{2+}, Er^{3+}	0.8	318	375	113–483	[182]

where ΔE is the energy difference between the lowest level of the excited state and parabola intersection point S (sometimes called the activation energy of the process in literature), k_B is the Boltzmann constant, and k_{NR0} and τ_{NR0} are non-radiative relaxation rate and lifetime at 0 K, respectively. The nonradiative relaxation rate is lower for larger ΔE and increases with increasing temperature. Considering that the radiative lifetime is a constant, $\tau_R(T) = \tau_0$, the expressions for the temperature dependencies of the emission intensity and lifetime are.

$$I_{MS}(T) = \frac{I_0}{1 + \frac{\tau_0}{\tau_{NR0}} \cdot \exp(-\Delta E/k_B T)},$$

$$\tau_{MS}(T) = \frac{\tau_0}{1 + \frac{\tau_0}{\tau_{NR0}} \cdot \exp(-\Delta E/k_B T)}, \quad (15)$$

where τ_0/τ_{NR0} is a constant, which is commonly called the frequency constant in the literature and has values on the order of 10^{13} s^{-1}. The Mott–Seitz theory is suitable for explaining the quenching of broadband emissions, where ΔR is large, for example, in molecular fluorescence. It is not suitable for describing the thermal quenching of narrow-line *f-f* emissions in trivalent lanthanides or the emissions of TM ions from excited states that have no configuration coordination parabola shifts against the ground state, i.e., where $\Delta R \approx 0$.

In the multiphonon relaxation model, the energy of the excited state is relaxed by phonon emission to the lattice mode (which may or may not be the ground state; Fig. 5b) and is described by the following formula:

$$k_{NR}(T) = k_{NR0} \cdot \left[\frac{\exp(h\nu/k_B T)}{\exp(h\nu/k_B T) - 1}\right]^{\frac{\Delta E}{h\nu}},$$

$$\tau_{NR}(T) = \tau_{NR0} \cdot \left[\frac{\exp(h\nu/k_B T)}{\exp(h\nu/k_B T) - 1}\right]^{-\frac{\Delta E}{h\nu}}, \quad (16)$$

where ΔE is the energy difference between the excited level and the next lowest level, $h\nu$is the dominant phonon energy of the lattice, and k_{NR0} is the value of the nonradiative transition rate at zero temperature that depends on the electron–lattice coupling strength. $\Delta\Delta E/h\nu = p$ represents the number of effective phonons that need to be emitted to bridge the energy gap difference. However, when numerous phonons are needed to bridge a gap, the process has a low probability; it is believed that processes involving more than seven effective phonons are quite improbable. When assuming that the radiative lifetime is temperature independent, $\tau_R(T) = \tau_0$, the expressions for the temperature dependencies of the emission intensity and lifetime are[60]:

$$I_{MPR}(T) = \frac{I_0}{1 + \frac{\tau_0}{\tau_{NR0}} \cdot \left[\frac{\exp(h\nu/k_B T)}{\exp(h\nu/k_B T) - 1}\right]^{\frac{\Delta E}{h\nu}}},$$

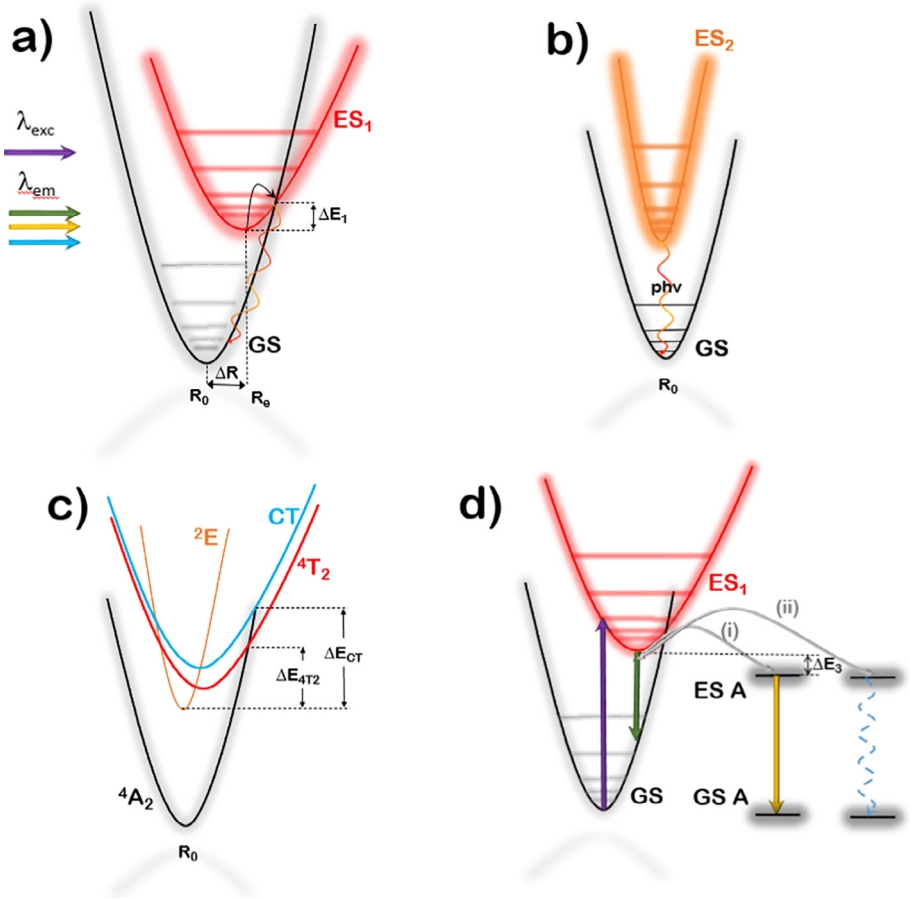

Fig. 5. Configuration coordinate diagram representation of the emission thermal quenching by Mott-Seitz model-a), Multi-phonon relaxation model -b), thermally activated cross-over via the charge transfer (CT) or excited states -c); energy transfer to Ln^{3+} ions-d).

$$\tau_{MPR}(T) = \frac{\tau_0}{1 + \frac{\tau_0}{\tau_{NR0}} \cdot \left[\frac{\exp(h\nu/k_BT)}{\exp(h\nu/k_BT)-1}\right]^{\frac{\Delta E}{h\nu}}}. \quad (17)$$

The previous equation can be written in terms of effective phonons and energy gap as.

$$I_{MPR}(T) = \frac{I_0}{1 + \frac{\tau_0}{\tau_{NR0}} \cdot [1 - \exp(-\Delta E/pk_BT)]^{-p}},$$

$$\tau_{MPR}(T) = \frac{\tau_0}{1 + \frac{\tau_0}{\tau_{NR0}} \cdot [1 - \exp(-\Delta E/pk_BT)]^{-p}}. \quad (18)$$

Relaxation by energy crossover from the excited state to a higher energy excited state, charge transfer (CT) band, or the host material conduction band (autoionization) successfully describes thermal quenching of the luminescence of TM ions with the $3d^3$ electron configuration (Fig. 5c). In this model, the radiative lifetime is considered to be temperature dependent, whereas the nonradiative relaxation rate has the same form as in the Mott-Seitz model:

$$k_R(T) = k_0 \cdot \coth\,(h\nu/2k_BT),$$

$$\tau_R(T) = \tau_0 \cdot \tanh\,(h\nu/2k_BT),$$

$$k_{NR}(T) = k_{NR0} \cdot \exp(-\Delta E/k_BT),$$

$$\tau_{NR}(T) = \tau_{NR0} \cdot \exp(\Delta E/k_BT). \quad (19)$$

Then, the expressions for the temperature dependencies of the emission intensity and lifetime are [61]:

$$I_{CO}(T) = \frac{I_0}{1 + \frac{\tau_0 \cdot \tanh\,(h\nu/2k_BT)}{\tau_{NR0}} \cdot \exp(-\Delta E/k_BT)},$$

$$\tau_{CO}(T) = \frac{\tau_0 \cdot \tanh\,(h\nu/2k_BT)}{1 + \frac{\tau_0 \cdot \tanh\,(h\nu/2k_BT)}{\tau_{NR0}} \cdot \exp(-\Delta E/k_BT)}. \quad (20)$$

The higher the configuration coordinate parabola offset between the ground state and the CT or the excited state, the larger the cross-over energy ΔE needed to activate the non-radiative de-excitation process. For example, the emission of Mn^{4+} activated phosphors, which have large $^4T_{2g}$ energies, starts to quench at high temperatures. Thermally activated auto-ionization occurs when the excited state of the optically active centre is very close to the conduction band minimum of the host material. Once the thermal energy is sufficiently high for the excited electron to overcome this energy gap, the electron becomes delocalized and can relax through several non-radiative channels (defects, trapping, etc.). This mechanism may drastically decrease the expected quenching temperature compared to that occurring due to energy band cross-over. Moreover, in a TM, Ln^{3+} co-doped the presence of Ln^{3+} may activate an additional channel of quenching of TM excited state (Fig. 5d). This type of energy transfer is described by Miyakava-Dexter formalism.

4. Figures of merit of luminescence thermometry

As a **measurand** (the quantity intended to be measured), temperature follows the universal guidelines for the evaluation of

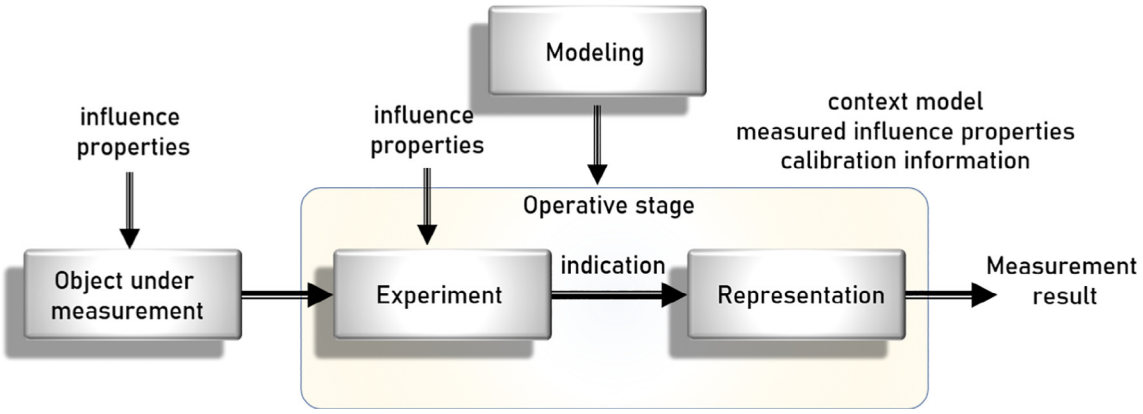

Fig. 6. Schematics of a typical measuring system.

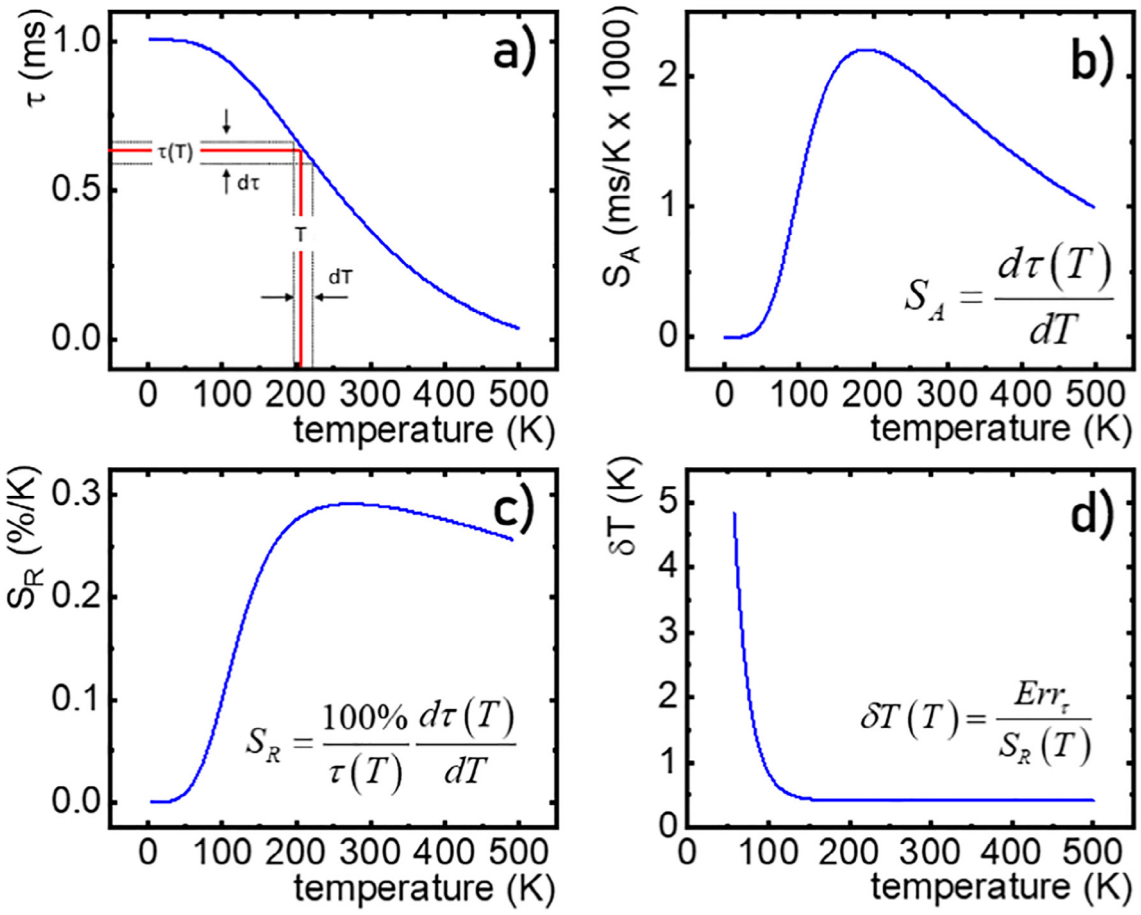

Fig. 7. Schematics of typical measuring system figures of merit when indication Q an excited state lifetime τ.

measured data. Using a standardized metrological approach enables consistent comparison of the performance and characteristics of different luminescence thermometry measurement systems and materials. Thus, most of the terminology used in this review is derived from the International Vocabulary of Metrology. Fig. 6 illustrates the general measurement processes that are performed to describe a typical luminescence thermometry measurement system. Here, the temperature is not measured directly, but instead an **indicator** *Q* is obtained experimentally (e.g., the emission lifetime, emission intensity, or wavelength of the emission line).Fig. 7..

The measurement process produces two essential components: **a numerical value** (measurement result, i.e., the temperature) as an estimate of the quantity measured and **the degree of uncertainty—**a parameter characterizing the range of values within which the value of the measurand can be said to lie within. Both are obtained from a measurement model, that is, from the mathematical relation among the temperature, indicator, and other quantities involved in the measurement. The terms **accuracy** and **precision** are closely associated with the measurement process and should be distinguished, as they are often sources of confusion. Because the measurement accuracy is the closeness of agreement

between the measured temperature and the true, unknown value, it is not possible to assign to it a numerical value; hence, it is a descriptive parameter. On the other hand, as the measurement precision is the closeness of agreement between independent measurements of a quantity under the same conditions, it can be expressed numerically using measures of imprecision such as the standard deviation or variance. Accordingly, **repeatability** is the measurement precision achieved by replicate measurements over a short period of time under repeatable measurement conditions using the same measurement procedure, measurement system, operator, operating conditions, and location. Similarly, **reproducibility** is the measurement precision under reproducible measurement conditions while repeating the measurements at distinct locations and using different measurement systems and operators.

Presented here are the typical figures of merit employed in luminescence thermometry using the lifetime temperature dependence as the indicator ($Q(T) = \tau(T)$) and the temperature as the measurand. The absolute **sensitivity** S of a luminescence thermometry measurement system is defined as the quotient of the change in the indicator and the change in temperature, and it is expressed in the units of the indicator over Kelvin:

$$S = \left|\frac{dQ(T)}{dT}\right|. \tag{21}$$

As luminescence thermometry indicators can be various physical properties with very different value ranges, they are not particularly suitable quantities for comparing results between measurement systems. Even if the same physical property is used as an indicator for the same measurement system, the indicator may vary if measured with different detection parameters. For example, if the indicator is the emission intensity, then amplification gains or different intensities of excitation will lead to different indicator values and ranges. Consequently, the change in the indicator with temperature, i.e., the sensitivity, will be different. We refer to this definition of sensitivity as absolute sensitivity. To circumvent this issue, the **relative sensitivity** is introduced as the ratio between the absolute sensitivity and indicator:

$$S_R = \left|\frac{1}{Q(T)}\frac{dQ(T)}{dT}\right|. \tag{22}$$

The relative sensitivity is the normalized sensitivity with respect to the indicator; it is expressed in units of inverse Kelvin or percent over Kelvin and is suitable for comparing results. Finally, the **temperature resolution** ($\delta T(T)$) is the smallest change in temperature that causes a perceptible change in the indicator; it is presented in Kelvin and is calculated as the ratio of the indicator uncertainty (expressed by the standard deviation) to the relative sensitivity:

$$\delta \mathrm{T} = \frac{\sigma}{S} = \frac{\sigma_R}{S_R}. \tag{23}$$

The temperature resolution strongly depends on the characteristics of the measurement system (for example, the noise), as well as on the indicator value.

Finally, the **spatial and temporal resolutions** of the measurement system can be defined as the minimum difference between points of a spatial or temporal measurement (δx or δt) that can be resolved under the temperature resolution of the system (δT), and they can be calculated as.

$$\delta x = \frac{\delta \mathrm{T}}{\left|\frac{dT}{dx}\right|}; \delta t = \frac{\delta \mathrm{T}}{\left|\frac{dT}{dt}\right|}. \tag{24}$$

However, the spatial resolution is restricted by the Rayleigh diffraction limit, which can be calculated from the maximum wavelength of the emission used in the measurement system and its numerical aperture.

5. Luminescent thermometers based on TM ions

5.1. Titanium

Titanium is one of the less frequently used TMs in luminescence thermometry, and only a few reports on its application can be found. The luminescence properties of two oxidation states of titanium have been described in the literature, namely, Ti^{3+} and Ti^{4+}, which have the d^1 and d^0 electronic configurations, respectively. The emission spectrum of Ti^{3+}, which prefers the octahedral coordination, consists of only one emission band assigned to the $^2E_g \rightarrow {}^2T_{2g}$ electronic transition usually localized in the red–near infrared (NIR) spectral range. On the other hand, the lack of electrons in the d orbital of Ti^{4+} causes its luminescence to be associated with the CT transition and usually localized in the ultraviolet (UV)–blue spectral range. The first works describing luminescent temperature sensors based on the emission of Ti^{3+} ions were presented by Katsumata et al. in 2007 [62] and 2008 [63] for sapphire (Al_2O_3) crystals. They found that the Ti^{3+} emission intensity decreased sublinearly at elevated temperatures in the 25–250 °C range, which suggests that a single emission band can be used for temperature sensing. After that, titanium was not used for temperature sensing for a relatively long time. Since 2018, there has been increasing interest in exploiting the properties of these ions in nanoscale luminescent materials. For instance, Drabik et al. [64,65] showed that by doping yttrium–aluminium garnet with titanium ions, it was possible to obtain both described oxidation states (Ti^{3+} and Ti^{4+}), whose emission bands occur in a spectrally non-overlapping range, and the intensity of each varied differently with temperature. This characteristic enabled the development of a thermometer using the intensity ratio with a low relative sensitivity of S_R = 0.7 %/K. To increase the accuracy of the temperature readout, the authors proposed using the Ln^{3+} (Ln^{3+} = Nd^{3+}, Eu^{3+}, Dy^{3+}) co-dopant emission intensity as a luminescence internal reference signal. This approach enabled S_R to be enhanced up to 2.26 %/K at 323 K and 3.70 %/K at 473 K. Wang et al. [66] proposed utilizing Ti^{4+}/Eu^{3+} co-doped $LiTaO_3$ micro rod arrays for ratiometric and temporal luminescence thermometry (Fig. 8c). The maximum obtained sensitivities (5.425 %/K for ratiometric luminescence thermometry and 3.637 %/K for temporal luminescence thermometry) enabled the development of an anti-counterfeiting system based on the temperature and time-domain response. Pan et al. proposed a very similar approach employing Ti^{4+} and Eu^{3+} co-doped ZrO_2 and achieved a sensitivity of 3.84 %/K using a ratiometric approach [67]. A peculiar effect was recently reported by Piotrowski et al. [45,68] who showed that the introduction of Ln^{3+} ions into $SrTiO_3$ nanocrystals due to the ionic compensation effect enhances the emission intensity of Ti^{3+} ions. The high susceptibility of the lifetime of the ^2E_g excited state to temperature changes enabled the development of a lifetime-based thermometer of very high sensitivity reaching S_R = 8.83 %/K at 180 K (Fig. 8d).

5.2. Vanadium

The luminescence properties of vanadium ions have been reported for V^{2+}(d^3), V^{3+} (d^2), V^{4+} (d^1), and V^{5+}; however, only the last three oxidation states have been used for luminescence thermometry to date. The first report on a vanadium-based luminescent thermometer was presented in 2018 for YAG:V^{3+}, V^{5+} nanocrystals [32]. It was found that in the nanosized particles, doping with vanadium ions led to the occurrence of two spatially segregated oxidation states. V^{5+} preferentially occupied the

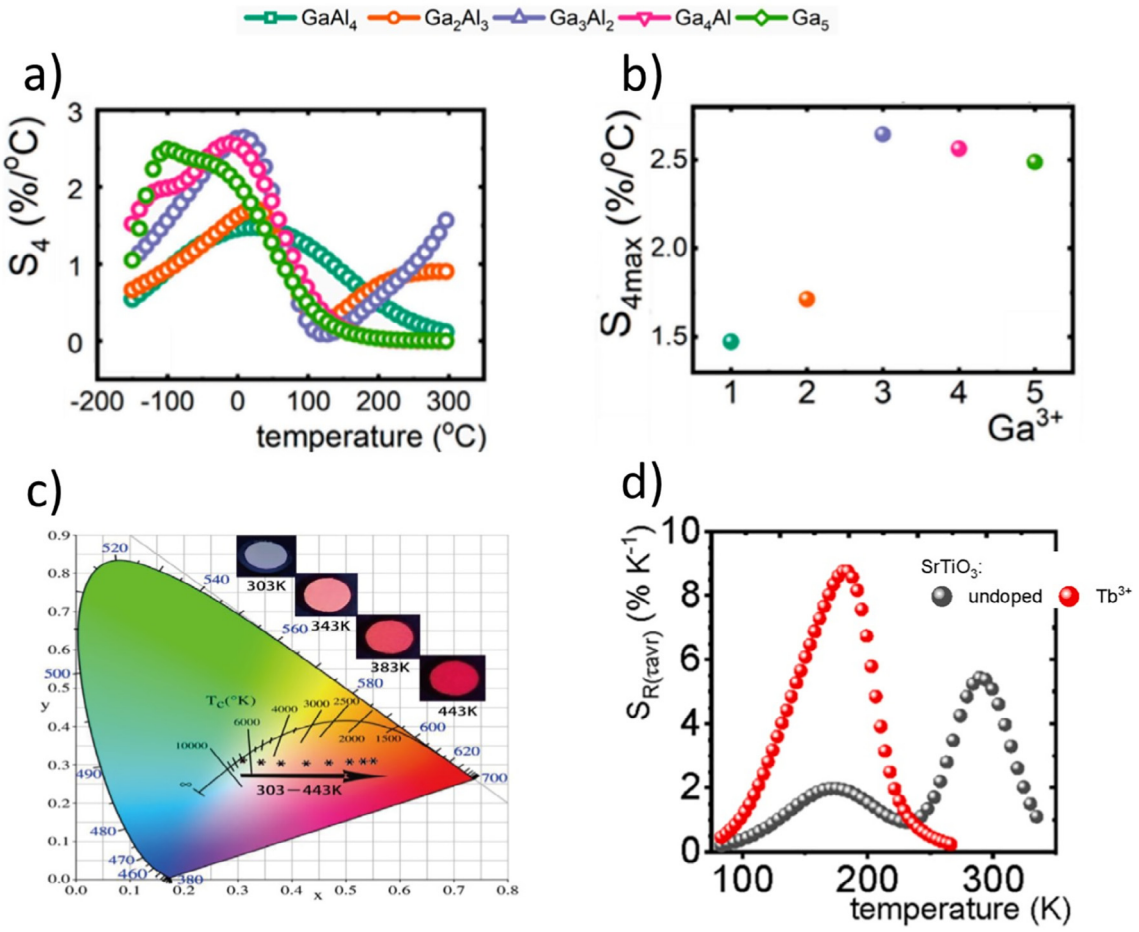

Fig. 8. The influence of the chemical composition on the thermal dependence of the S_R of ratiometric luminescence thermometer based on LIR of V^{5+} and V^{4+} ions-a) and the maximal S_R as a function of the Ga^{5+} concentration -b) in $Y_3Al_{5-x}Ga_xO_{12}$ nanocrystals [69]; thermal dependence of the CIE coordinates of the luminescence from $LiTaO_3$:Ti^{4+}, Eu^{3+}@PDMS -c) [66]; thermal dependence of the S_R of the lifetime based luminescent thermometer on Ti^{3+} emission in $SrTiO_3$ and the $SrTiO_3$:Tb^{3+} nanocrystals-d) [45].

nanocrystal surfaces, whereas V^{3+} occupied the inner part. In this case, the emission spectra consisted of two broad bands centred at 520 nm and 820 nm, which could be attributed to the CT transition of V^{5+} and the $^3T_{1g} \rightarrow {}^3T_{1g}$ transition of V^{3+}, respectively. Due to the much lower activation energy of thermal quenching in V^{3+} compared to that in V^{5+}, a highly sensitive LIR-based thermometer was developed (S_R = 4–6 %/K at 250–300 °C). The co-doping with Ln^{3+} did not enhance the sensitivity in this case. In the case of $LaGaO_3$:V nanocrystals, the V^{3+}, V^{4+}, and V^{5+} oxidation states even occurred simultaneously [70]. Hence, the nanoparticle emission spectra consisted of three emission bands at 497 nm, 633 nm, and 733 nm attributed to the CT transition (V^{5+}), $^2E \rightarrow {}^2T_2$ (V^{4+}), and $^3T_{1g} \rightarrow {}^3T_{1g}$ (V^{3+}), respectively. The differences between the thermal quenching rates of these oxidation states enable the development of ratiometric thermometers, although they have low relative sensitivity. The introduction of Nd^{3+} as a luminescent reference ion led to the development of a thermometric phosphor with different thermometric performance depending on the selection of the particular emission band of different oxidation states of vanadium ions (S_R = 1 %/K (at 268 K), 0.49 %/K (at 253 K) and 1.44 %/K (at 348 K) for $LaGaO_3$:V^{5+}, Nd^{3+}, $LaGaO_3$:V^{4+}, Nd^{3+}, and $LaGaO_3$:V^{3+}, Nd^{3+}, respectively). It was also found that the relative sensitivities of both vanadium-based luminescent nanothermometers could be modulated by the grain size (annealing temperature) and dopant concentration. The thermometric performance of the V-based luminescent thermometer can be also modulated by the Ga^{3+} to Al^{3+} ionic ratio (Fig. 8 a b). V^{5+} luminescence is often observed in vanadates (also identified as a host material luminescence), where V^{5+} is tetrahedrally coordinated in the $(VO_4)^{3-}$ polyhedra. Kolesnikov exploited the V^{5+} to Er^{3+} emission intensity ratio for temperature sensing in YVO_4:Er^{3+}, achieving a sensitivity of 1.58 %/K at 300 K [71].

5.3. Chromium

5.3.1. Cr^{3+}

Chromium ions are the most readily and widely used TM ions in luminescence thermometry, due to the high emission intensity and numerous advantages resulting directly from the $3d^3$ electron configuration of Cr^{3+}. In the case of Cr^{3+} ions, luminescence occurs by radiative depopulation of the ^2E and/or $^4T_2$ energy levels. In contrast to the configuration coordination parabola of the ^2E level, that of the $^4T_2$ state is shifted with respect to the parabola of the ground $^4A_2$ level in the wave vector domain. This shift results in the spectral representation of the $^2E \rightarrow {}^4A_2$ electron transition being a narrow spectral emission band, whereas the $^4T_2 \rightarrow {}^4A_2$ transition corresponds to a broad emission band. Moreover, the energy of the $^4T_2$ level strongly depends on the local crystal field affecting the Cr^{3+} ions. These ions preferentially occupy octahedral crystallographic positions; hence, according to the Tanabe-Sugano diagram for the d^3 electron configuration, an increase in CFS causes an increase in the $^4T_2$ level energy. When Cr^{3+} ions experience a weak crystal field ($Dq/B < 2.1$), the energy of the $^4T_2$ level is below that of the ^2E level and the emission spectrum of Cr^{3+} ions consists of a

broad emission band. In the case of a strong crystal field, the energy of the ^2E level is lower; hence, the emission spectrum consists of a spectrally narrow emission line. In cases of intermediate crystal fields, both emission bands are observed in the luminescence spectra. An important advantage of Cr^{3+} ions is the simple correlation associating the strength of the crystal field to the Cr^{3+}–ligand distance in the matrix (R, usually Cr^{3+}–O^{2-} or Cr^{3+}–F^-) $Dq/B \sim R^{-5}$. Hence, appropriate choices of the structural parameters of the host material enable the optimization of the spectroscopic properties of the phosphor according to the application requirements. This has important implications from a thermometric perspective because the activation energy of the nonradiative depopulation of the ^2E and $^4T_2$ levels can also be controlled by the strength of the crystal field and thus enables optimization of the thermometric parameters of the luminescent thermometer. Moreover, two broad absorption bands of Cr^{3+} ions localized in the visible spectral range facilitate excitation wavelength selection to match the application requirements [72].

Two main strategies have been observed in luminescence thermometry applications using the emission intensity of Cr^{3+} ions. The first one is ratiometric thermometry using the LIR of the ratio between the emission intensities of the $^2E \rightarrow {}^4A_2$ and $^4T_2 \rightarrow {}^4A_2$ bands. The second utilizes the luminescence of Cr^{3+} ions as a temperature probe and a reference luminescence signal. The former approach typically exploits intermediate crystal field materials in which a quasi-thermal coupling between the ^2E and $^4T_2$ levels is observed. Typically, an increase in temperature causes an increase in the population of the $^4T_2$ level relative to that of the ^2E level.

The energy separation between these states can be modified by varying the CFS, which in turn adjusts the thermometric properties of the $^2E \rightarrow {}^4A_2/\,{}^4T_2 \rightarrow {}^4A_2$ ratiometric thermometer. Shi et al. verified this hypothesis in a series of $Al_3(BO_3)_4:Cr^{3+}$ (A = Y, Lu, Gd) [39]. The performed studies revealed that S_R was proportional to the energy separation between the considered energy levels and changed from S_R = 0.8 %/K at 310 K for $Lu_3(BO_3)_4:Cr^{3+}$ (Dq/B = 2.34) to S_R = 0.5 %/K for $Gd_3(BO_3)_4:Cr^{3+}$ (Dq/B = 2.3). Back et al. investigated the role of the crystallographic symmetry of the host material on a Boltzmann type Cr^{3+}-based luminescent thermometer in $Ga_2O_3:Cr^{3+}$ [28]. The authors revealed that the change in symmetry from trigonal (α-Ga_2O_3) to monoclinic (β-Ga_2O_3) decreased Dq/B from 2.97 to 2.58 and enhanced the relative sensitivity of the former (S_R = 1.05 %/K for α-$Ga_2O_3:Cr^{3+}$ compared to S_R = 0.64 %/K for β-$Ga_2O_3:Cr^{3+}$ at 300 K). Thus, the temperature uncertainty was 0.42 K for β-Ga_2O_3 and 0.25 K for α-Ga_2O_3. In addition, in the case of β-$Ga_2O_3:Cr^{3+}$, the LIR dependence followed the Boltzmann law throughout the analysed temperature range (200–450 K), whereas it did so only above 270 K for the α polymorph. This finding is important as this thermal relation facilitates the theoretical prediction of the calibration curve. The correlation between S_R and the energy separation between the energies of the ^2E and $^4T_2$ states revealed that S_R increased with ΔE. However, there seemed to an asymptote around S_R = 4 %/K, indicating that there is a limit to the S_R that can be realized with this type of thermometer. The authors also demonstrated that this compound can be used for operando monitoring of the catalytic reaction temperature (ethylene hydrogenation over platinum nanoparticles). An even wider temperature range (270–700 K) in which the $^2E \rightarrow {}^4A_2/{}^4T_2 \rightarrow {}^4A_2$ luminescent thermometer follows the Boltzmann distribution was reported by Ueda et al. in $ZnGa_2O_4:Cr^{3+}$ [73]. In this material, due to the spectral overlap between the considered emission bands, the intensities of the individual bands were obtained by deconvolution. The high relative sensitivity (S_R = 2.8 %/K at 310 K) resulted from the relatively large energy distance between the ^2E and $^4T_2$ states (1640 cm^{-1}). An even higher sensitivity was reported for $MgAl_2O_4:Cr^{3+}$ using the same approach, where S_R = 3.5 %/K to S_R = 2.9 %/K in the 300–330 K range was obtained with 0.3 K temperature uncertainty [29]. Zhu et al. [74] utilized the LIR of the R_1 and R_2 emission lines of Cr^{3+} in $ZnAl_2O_4:Cr^{3+}$ and $ZnAl_2O_4:Cr^{3+}$, Mn^{2+}. Their studies indicated that introducing the Mn^{2+} co-dopant reduced the formation probability of inversion defects in the spinel structure and thus increased the energy separation between the R_1 and R_2 lines from 32 cm^{-1} to 165 cm^{-1}. Considering this small energy separation, the authors obtained surprisingly high values of $S_R \sim$ 3.6 %/K and $S_R \sim$ 0.75 %/K at 77 K for $ZnAl_2O_4:Cr^{3+}$, Mn^{2+} and $ZnAl_2O_4:Cr^{3+}$, respectively. These results indicate the beneficial effect of the structural ordering on the thermometric performance of Cr^{3+}-based luminescent thermometers. Back et al. developed a ratiometric Cr^{3+}-based thermometer for the cryogenic temperature range that follows the Boltzmann distribution in the 40–150 K range. The relatively high S_R ($S_R \sim$ 2 %/K at 40 K and temperature uncertainty of 0.045–0.77 K in the 40–150 K temperature range) was achieved by the intentional design of a host material with a small energy gap between the ^2E and $^4T_2$ states ($CaHfO_3:Cr^{3+}$) based on theoretical calculations (Fig. 9a and b) [75].

In general, the limitation of the $^2E \rightarrow {}^4A_2/{}^4T_2 \rightarrow {}^4A_2$ ratiometric approach is that the operating temperature range in which such a thermometer can be used must be limited to prevent thermal coupling between the ^2E and $^4T_2$ levels. Moreover, the fact that the two bands spectrally overlap presents additional difficulties in separating the signals being analysed and thus limits the accuracy of the temperature determination. Finally, as shown by Back et al., the maximum S_R achievable by this approach is limited to $\sim$ 4 %/K.

Another luminescence thermometry solution using Cr^{3+} ions involves exploiting the strongly temperature-dependent Cr^{3+} ion emission as a temperature probe with the additional luminescence signal as a reference. For this purpose, the luminescence of lanthanide ions, which are characterized by lower susceptibility to thermal quenching of luminescence than Cr^{3+} ions, is the most commonly applied. Similarly, the emission from defects in the host materials can be used as an internal reference [76]. From an application perspective, it is beneficial to exploit host materials in which the CFS affecting the Cr^{3+} ions is weak, so that an increase in temperature causes rapid temperature quenching of the luminescence. An example of such a thermometer is $LiLaP_4O_{12}:Cr^{3+}$, Nd^{3+} [77]. In this case, the Cr^{3+} ions occupy interstitial positions due to the lack of octahedrally coordinated crystallographic positions, which results in an emission spectrum consisting of a broad band typical of the $^4T_2 \rightarrow {}^4A_2$ transition. The efficient thermal quenching of the luminescence resulted in a high relative sensitivity of S_R = 4.89 %/K at 323 K and sensitivities S_R > 15 %/K for temperatures in the 423–473 K range of a ratiometric Cr^{3+} to Nd^{3+} ($^4F_{3/2} \rightarrow {}^4I_{11/2}$) luminescent thermometer. However, the low luminescence intensity at temperatures above 423 K negatively affected the precision of the temperature readout. For luminescent thermometers based on the intensity ratio between Cr^{3+} and the luminescence reference, it is important that the optical excitation be selected to excite both types of ions simultaneously and independently to maximize sensitivity. Otherwise, the dominant process through which the excited states of Ln^{3+} ions will be populated will be the $Cr^{3+} \rightarrow Ln^{3+}$ energy transfer, which will negatively affect the sensitivity of the thermometer. An example of this effect is the result reported for $LiLaP_4O_{12}:Cr^{3+}$, Yb^{3+}. Although the energy separation between the $^2F_{5/2}$ and $^2F_{7/2}$ levels of Yb^{3+} ions ($\sim$10 000 cm^{-1}) limits the probability of nonradiative depopulation of the $^2F_{5/2}$ level, the lack of higher energy levels enabling simultaneous excitation of Cr^{3+} and Yb^{3+} caused the sensitivity of the thermometer to drop to S_R = 0.32 %/K [78] compared to S_R = 4.89 %/K for its counterpart co-doped with Nd^{3+} ions [77]. The importance of the population channel of the excited level of the luminescent reference ion through the appropriate choice of optical excitation wavelength has been proven for the YAG:Cr^{3+},

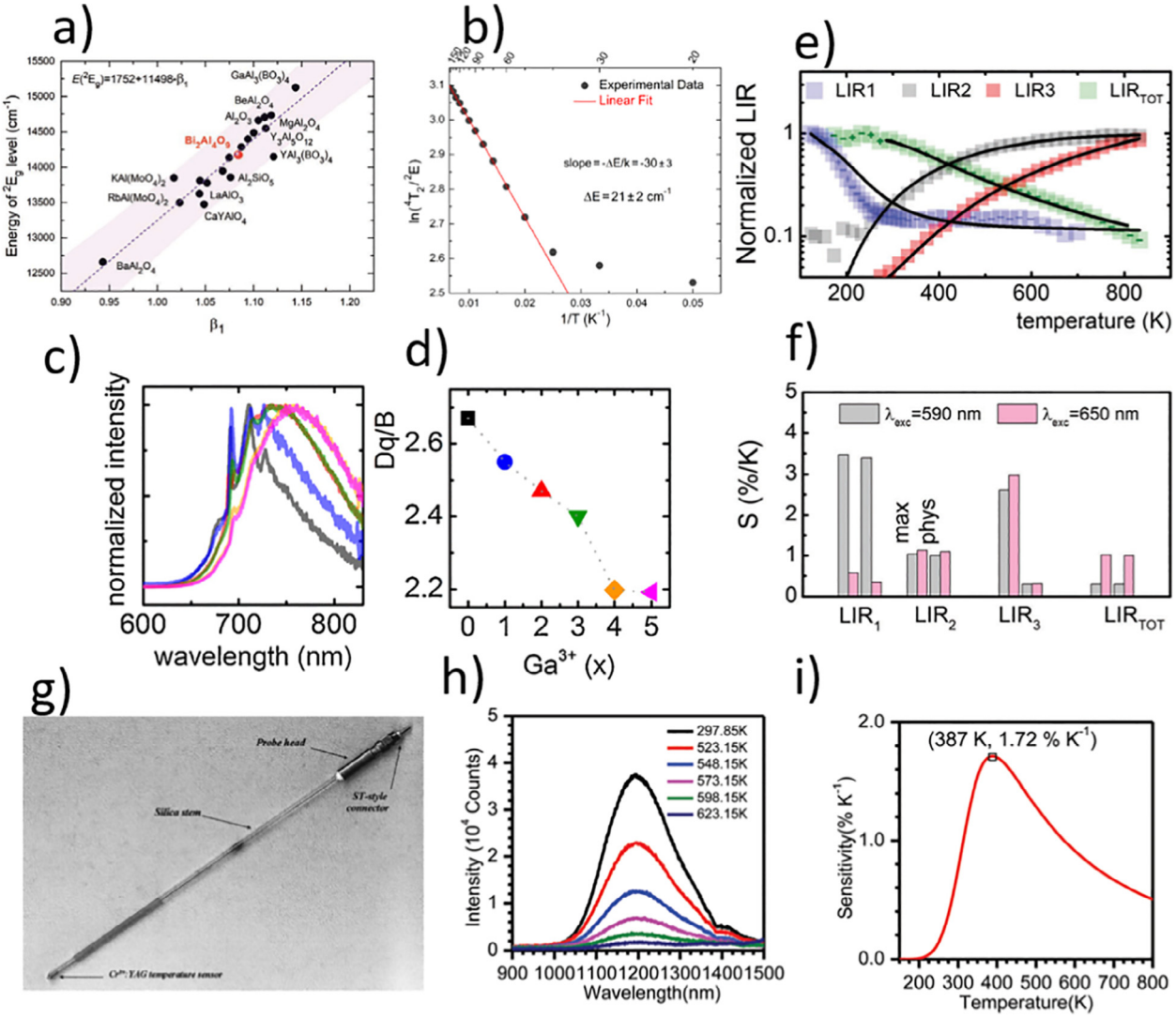

Fig. 9. The ^{2}E energy as a function of the nephelauxetic parameter β_1 for various Cr^{3+}-doped aluminate-based materials.-a) [117]; Arrhenius ln(LIR) versus T^{-1} plot for $CaHfO_3$:Cr^{3+} used to calibrate the thermometer -b) [75]; a comparison of normalized emission in $Gd_3Al_{5-x}Ga_xO_{12}$ Cr^{3+}-c)[40]; the influence of Ga^{3+} concentration on the Dq/B parameter (■ $Gd_3Al_5O_{12}$ $Gd_3Al_4GaO_{12}$ $Gd_3Al_3Ga_2O_{12}$ $Gd_3Al_2Ga_3O_{12}$ $Gd_3AlGa_4O_{12}$ $Gd_3Ga_5O_{12}$) doped with Cr^{3+} ions-d)[40]; a comparison between thermal dependence of LIR_1 [Cr^{3+} to $^4F_{3/2} \rightarrow {}^4I_{9/2}$ of Nd^{3+}] (blue), LIR_2 [Cr^{3+} to $^4F_{5/2}$,$^2H_{9/2} \rightarrow {}^4I_{9/2}$ of Nd^{3+}] (gray), LIR_3 [Cr^{3+} to $^4F_{7/2}$,$^4S_{3/2} \rightarrow 4I_{9/2}$ of Nd^{3+}](red) and LIR_{TOT} [Cr^{3+} to integral emission intensities of all Nd^{3+} emission bands] (green) in YAG:Cr^{3+},Nd^{3+} e)[79]; and corresponding maximal (max; at 200 K) physiological (phys; at 303 K) S_R of luminescent thermometer upon λ_{exc} = 590 nm (grey) and λ_{exc} = 650 (pink) nm in YAG:Cr^{3+},Nd^{3+}-f)[79]; one of the first YAG:Cr^{3+} luminescent temperature sensor device -g)[109]; emission spectra of Cr^{4+} in SiO_2–$10Al_2O_3$–20ZnO–19.9SrO–$0.1Cr_2O$ measured as a function of temperature-h)[118]; and corresponding S_R of the Cr^{4+} intensity based luminescent thermometer-i)[118].

Nd^{3+} system, for which the excitation spectral shift from the excitation wavelength of the energy level of the Nd^{3+} ions (λ_{exc} = 590-nm) to the wavelength inducing the population of the emitting level through the $Cr^{3+} \rightarrow Nd^{3+}$ energy transfer pathway (λ_{exc} = 650-nm) resulted in a reduction of the maximum sensitivity from S_R = 3.3 %/K to S_R = 0.58 %/K (Fig. 9e and f) [79].

As already mentioned, the variation of the Cr^{3+}–O^{2-} distance significantly modifies the strength of the crystal field interacting with the Cr^{3+} ions and, thus, changes the activation energy of non-radiative processes. This significantly affects the properties of the thermometer based on the LIR of Cr^{3+} and Nd^{3+}. The change in CFS is often accomplished by substituting Al^{3+} ions of smaller ionic radii for Ga^{3+} or Sc^{3+} ions of larger ionic radii. As experimentally confirmed, Cr^{3+} ions occupying Ga^{3+} and Sc^{3+} crystallographic positions are more susceptible to temperature quenching of luminescence. An example of this effect is the increase in relative sensitivity for $Gd_3Al_5O_{12}$:Cr^{3+}, Nd^{3+} from S_R = 1.2 %/K to S_R = 1.9 %/K for $Gd_3Ga_5O_{12}$:Cr^{3+}, Nd^{3+} (Fig. 9c and d) [40]. Chen et al. used a similar approach for YAG:Cr^{3+}, Dy^{3+} and YAG:Cr^{3+}, Eu^{3+}, for which S_R = 2.32 %/K and S_R = 2.43 %/K, respectively [80]. However, in this case, the lower intensity difference between the Ln^{3+} and Cr^{3+} emission bands for Dy^{3+} co-doped phosphors should result in more accurate temperature determination. Relatively low relative sensitivity (S_R = 0.259 %/K) was found for $BaAl_{12}O_{19}$:Eu^{2+}, Cr^{3+} with the ratiometric approach [81]. Such low sensitivity is probably associated with the population of the Eu^{3+} excited state via the $Cr^{3+} \rightarrow Eu^{3+}$ energy transfer. However, also changing the cations located in the second coordination zone may significantly influence the thermometric parameters, as in the case of the change from $La_3Ga_5O_{12}$:Cr^{3+} to $La_2LuGa_5O_{12}$:Cr^{3+} [41]. In addition, the difference in ionic radii between the substituent and dopant ions enables the luminescence properties and thermometric parameters of Cr^{3+} ion doped materials to be altered by increasing the dopant ion concentration. Therefore, upon increasing the concentration of Cr^{3+} ions from 0.06 %Cr^{3+} to 12 %Cr^{3+} in $Y_3Al_2Ga_3O_{12}$, a change in the emission spectrum from narrowband emission

characteristic of a strong crystal field to broadband emission associated with depopulation of the $^4T_2$ level and a simultaneous an increase in relative sensitivity from S_R = 0.17 %/K to S_R = 1.17 %/K at 423 K were observed [42]. Perisa et al. merged both ratiometric approaches by showing that in YAG:Cr^{3+}, Dy^{3+}, both LIR of Cr^{3+} to Dy^{3+} and LIR of $^2E \rightarrow {}^4A_2$ to $^4T_2 \rightarrow {}^4A_2$ can be implemented, yielding S_R = 0.64 %/K at 175 K and S_R = 2.2 %/K at 200 K, respectively [82]. Utilizing the luminescence of Ln^{3+} ions is not the only means of providing a reference signal for ratiometric thermometers based on Cr^{3+} emission. Ciric et al. proposed the use of emission associated with structural defects in $MgTiO_3$:Cr^{3+} as a reference luminescence signal for Cr^{3+} ions [30]. As has been shown, the emission band at approximately 480 nm (defect emission) exhibits much lower susceptibility to temperature changes than the $^2E \rightarrow {}^4A_2$ band luminescence. The intensity ratio between these bands yielded S_R = 2.62 %/K at 301 K.

One of the trends found in the literature related to the search for a luminescent reference signal for Cr^{3+} ion emission is a mixing of two phosphors, one doped with Cr^{3+} ions and the other usually doped with Ln^{3+} ions. One advantage of this approach is the possibility of optimizing the stoichiometry of the matrix for the requirements of each dopant ion separately. As already mentioned, Cr^{3+} prefers the octahedral crystallographic position, which is not present in all matrices. In addition, the desire to reduce the probability of nonradiative processes, which can lead to a decrease in the emission intensity of Ln^{3+} ions, necessitates the selection of matrices with low phonon energy, which often involves the lack of crystallographic positions that can be occupied by Cr^{3+} ions. In addition, the use of two separate phosphors practically eliminates the risk of energy transfers that may occur between Cr^{3+} and Ln^{3+} and that may negatively influence the thermometric parameters. However, this solution has the drawback of requiring the homogeneity of these phosphors to be maintained in practical applications. As the ratio between the intensities of these ions is a thermometric parameter and the emission intensity depends on the phosphor concentration, even small local fluctuations in the ratio of phosphors can contribute to an unreliable and inaccurate temperature readout. Zhou et al. proposed using a mixture of Al_2O_3:Cr^{3+} and $GdVO_4$:Eu^{3+} for temperature sensing [83,84]. An interesting aspect of this study was that the researchers used an excitation wavelength in the sideband of the Eu^{3+} absorption band. Thus, an increase in temperature due to the spectral broadening of this band resulted in an increase in the emission intensity of the Eu^{3+} ions and, thus, luminescence signals of opposite monotonicity. The maximum sensitivity, in this case, was S_R = 2.4 %/K in the 300–753 K temperature range. Qiu et al. reported a much higher sensitivity of S_R = 3.68 %/K for $LiAl_5O_8$:Cr^{3+} and $LuPO_4$:Tb^3 [85]. Meanwhile, Chen et al. presented ratiometric luminescent thermometers based on the up-conversion process and reported low sensitivities of S_R = 0.35 %/K and S_R = 0.25 %/K at ~ 345 K for $LiGa_5O_8$:Cr^{3+}, Yb^{3+}, Ho^{3+} and $LiGa_5O_8$:Cr^{3+}, Yb^{3+}, Er^{3+}, respectively [86] The important aspect of these studies is that the Cr^{3+} emission was obtained using NIR excitation via up-conversion.

Another interesting idea was to employ the absorption from the excited state (higher vibronic components) of Cr^{3+} ions for luminescence thermometry. In this way, by using appropriately selected excitation wavelengths (one matched to the absorption from the ground state and the other from the excited state), it was possible to obtain opposite thermal monotonicities of the intensity of the same emission band [87]. This enabled the development of single-band ratiometric luminescent thermometers in YAG:Cr^{3+}, $YAlO_3$:Cr^{3+}, and $LiLaP_4O_{12}$:Cr^{3+}. The relatively low sensitivities obtained with this approach (max S_R = 0.35 %/K for $YAlO_3$:Cr^{3+}) did not prevent 2D thermal imaging of the temperature distribution around the resistance wire from being conducted. Ciric et al. developed a multiparametrical luminescent thermometer based on the LIR of the R_1 and R_2 emission lines, lifetime of the ^2E state, and spectral position of the emission line in Al_2O_3:Cr^{3+} coatings created by plasma electrolytic oxidation (S_R = 4.8 %/K at 20 K, S_R = 0.9 %/K at 450 K, and S_A = 0.2 cm^{-1}/K at 550 K, respectively) [88]. These studies indicate that the temperature determination uncertainties using the lifetime and ratiometric approaches can be as small as 0.08 K and 0.06 K, respectively. However, when this approach was applied for Mg_2TiO_4:Cr^{3+}, much lower sensitivities were obtained (S_R = 1.73 %K, S_R = 0.75 %/K, and S_A = 65 cm^{-1} for the ratiometric, lifetime, and bandshift approaches, respectively) [76]. These values decreased even further to S_R = 0.7 %/K at 310, S_R = 0.92 %/K, and S_A = 0.254 cm^{-1}/K for the ratiometric, lifetime, and bandshift approaches, respectively, in $MgSiO_4$:Cr^{3+} [31] due to the high thermal stability of the luminescence in this phosphor. Mykhaylyk et al. [89] developed multiparametric luminescent thermometers on Al_2O_3:Cr^{3+}, Mn^{4+} and analysed the ratiometric (R_1 to R_2), lifetime, and bandshift thermometric approaches. The authors concluded that the lowest temperature uncertainty was obtained with the ratiometric approach and was much smaller when the emission of Cr^{3+} (0.1 K at 20 K) was considered than for Mn^{4+} (0.35 K at 40 K). In a follow-up study, the authors compared multimodal thermometers based on Cr^{3+} emission (Al_2O_3:Cr^{3+}, Ga_2O_3:Cr^{3+}, $Y_3Al_5O_{12}$:Cr^{3+}, $YAlO_3$:Cr^{3+}) [90,91]. Their research revealed that the lowest temperature determination uncertainty for the ratiometric approach (R_1 to R_2) occurred for Al_2O_3:Cr^{3+} (0.06 K), whereas that for the lifetime-based approach (0.3 K) occurred for Ga_2O_3:Cr^{3+}. No significant difference in the temperature uncertainty was found with the bandshift approach. Glais et al. [92] proposed a unique multiparametric luminescent thermometer based on the persistent luminescence of Cr^{3+} ions in $ZnGa_2O_4$:Cr^{3+}, Bi^{3+} nanocrystals. The authors evaluated the applicative potential of band broadening, luminescence intensity ratio between the R_1 and R_2 lines, lifetime of the ^2E state, and decay of the persistent luminescence. The highest S_R was found in the case of the lifetime-based thermometer (S_R = 1.93/K). The fact that such a high value was achieved (S_R = 1.6 %/K) for the case of persistent luminescence decay makes this phosphor interesting for biomedical applications. This is because the application of persistent luminescence eliminates the requirement of phosphor excitation during in vivo temperature sensing. Some of the first studies directly suggesting the use of the luminescence decay times of Cr^{3+} ions were presented by Grattan et al. [93] in Al_2O_3:Cr^{3+} in 1991 and by Zhang et al [94] in $BeAl_2O_4$:Cr^{3+} in 1992. These researchers showed that the luminescence kinetics exhibits a monotonic temperature dependence over the wide temperature range (10–700 K), enabling very good theoretical description by using a two-level kinetic model. A relatively large group of Cr^{3+}-based luminescent thermometers exploits the luminescence kinetics (generally of the ^2E state). In the case of a lifetime-based thermometer using $BaAl_{12}O_{19}$:Eu^{2+}, Cr^{3+}, only S_R = 0.466 %/K at 366 K has been reported [81]. Another example exploiting the multiphase glass ceramics was the combination of CaF_2:Er^{3+} with $ZnAl_2O_4$:Cr^{3+} [95]. By placing each dopant ion in a separate structure, it was possible to eliminate the energy transfer between them. The maximum sensitivity of the thermometer based on the luminescence kinetics of Cr^{3+} ions was S_R = 0.67 %/K at 535 K. In the case of Ga_2O_3:Cr^{3+} in the glass ceramic of Ga_2O_3:Cr^{3+}, YF_3:Er^{3+}, Yb^{3+} composition, S_R = 0.59 %/K was obtained at 386 K [96], whereas the modification of one glass ceramic component (Ga_2O_3:Cr^{3+}, LaF_3:Er^{3+}, Yb^{3+}) slightly increased S_R to 0.66 %/K at 500 K [97]. Chen used lifetime-based thermometry to assess the thermometric properties of the ^2E state level of Cr^{3+} ions in ceramics, achieving maximum S_R of 0.76 %/K (at 295 K), 0.46 %/K (at 370 K), and 0.58 %/K (at 420 K). Similarly, Borisov et al. reported S_R = 0.97 %/K at 274 K for $YAl_3(BO_3)_4$:Cr^{3+} [43]. Elzbieciak et al. conducted systematic studies of the thermometric performance of

lifetime-based Cr^{3+}-doped thermometers using the average lifetime estimation method and a high concentration of Cr^{3+} (2 %molar) to achieve a nonexponential decay profile shape. The most important conclusion was that the lifetime estimation method may affect not only the lifetime itself, but also its thermal dependence and thus the relative sensitivity [98].

Although not discussed by the authors, some general tendencies can be observed from the presented studies. It appears that the higher the CFS, the higher the temperature at which the maximum S_R is achieved. This tendency is expected because, except in the low crystal field approximation, the CFS defines the energy separation between the ^2E and $^4T_2$ states. Qiu et al. [85] and Li et al. [99] reported S_R = 0.8 %/K for $LiAl_5O_8$: Cr^{3+} [100]. Li et al. obtained a similar value of S_R = 0.81 %/K at 503 K for $ZnAl_2O_4$:Cr^{3+} nanocrystals [101]. However, as shown by Chen et al., changing host material composition to $LiGa_5O_8$:Cr^{3+} enables *SR* to be increased to 1.1 %/K, which can be explained by the lower activation energy associated with the lowering of the CFS [102]. An even more illustrative example of this tendency was presented by the same group for $Bi_2(Al/Ga)_4O_9$:Cr^{3+} when the lowering the CFS associated with the change of the Al^{3+} to Ga^{3+} molar ratio led to an increase in the sensitivity of the lifetime-based thermometer from $\sim S_R$ = 0.7 %/K for $Bi_2Al_4O_9$:Cr^{3+} to S_R = 3.26 %/K for $Bi_2Ga_2Al_2O_9$ [44]. Wang et al. presented very interesting studies for the CaF_2:Cr^{3+} glass ceramic, in which they demonstrated the influence of replacing O^{2-} with F^- on the thermometric performance of the lifetime-based luminescent thermometers [103]. The enriching of the glass ceramics with F^- ions led to a decrease in the CFS, inducing greater separation between the ^2E and $^4T_2$ states. Meanwhile, for the O^{2-} coordinated Cr^{3+}, the emission from the ^2E state was dominant, and enriching the glass ceramic with F^- ions led to emission spectrum changes including the occurrence of the $^4T_2 \rightarrow {}^4A_2$ emission band. The relative sensitivity of the O^{2-} coordinated Cr^{3+} was found to be higher (S_R = 0.76 %/K at 498 K) than that of the F^- coordinated one (S_R = 0.47 %/K at 351 K). Mondal et al. reported a highly sensitive Cr^{3+}-based lifetime luminescent thermometer for $ZnGa_2O_4$:Cr^{3+}, which achieved S_R = 1.8 %/K at 450 K. However, as discussed by the authors, the defect contribution to the Cr^{3+} excited level population was responsible for the high thermal dependence of the Cr^{3+} lifetime. As confirmation of this hypothesis, the thermal dependences of the ^2E state lifetime for different excitation wavelengths used for thermometry were presented [104]. Although most scholars investigating lifetime-based luminescent thermometers have employed time-domain methods, Venturini et al. showed that the results obtained with frequency-domain detection schemes are also promising, using the example of $YAl_3(BO_3)_4$:Cr^{3+} [105]. Seeking new temperature sensors based on luminescence phenomena for use in imaging engine compartments during combustion, whose temperature readings should be independent of the gas composition and its pressure in the compartment, Fuhrmann et al. presented a $Gd_3Ga_5O_{12}$:Cr^{3+} lifetime-based thermometer [106].

The early work on thermometry based on the luminescence decay times of Cr^{3+} ions was not limited to materials research, but rather was mainly motivated by applications. Simple Cr^{3+}-based fiber optic thermometers were constructed and described in the second half of the 20th century. Anghel et al. confirmed that the calibration curve of an Al_2O_3:Cr^{3+}-based fiber optic temperature probe perfectly matched the previously reported data for a single crystal in the 200–350 K temperature range [107] and even up to 700 K [108]. Also YAG:Cr^{3+} was used as for this purpose (Fig. 9g) [109].

The performed tests confirmed the high reliability of temperature determination using this system. Similar investigations performed on magnesium-rich olivine (Mg,Fe)SiO_4:Cr^{3+} indicated that much shorter lifetimes occurred in the latter case ($\tau \sim 20$ μs at 200 K) and that the lifetime was shortened only above 250 K [110]. The lifetime of the ^2E state obtained using the time domain in Al_2O_3:Cr^{3+} coating on an alumina plate was applied to study the wall temperatures and heat fluxes from nearly-one-dimensional flat premixed flames [111] and in a form of Al_2O_3:Cr^{3+} sheet using a phase-shift technique [112]. Pflitsch et al. revealed that this phosphor material can be successfully used for temperature sensing in the form of thin films deposited by thermal CVD on Si(100) and stainless steel [113]. Glais et al. demonstrated that the luminescence decay kinetics of Cr^{3+} ions can be successfully used to take temperature readings during light-stimulated system heating [114]. For this purpose, gold nanorods were used as light-to-heat converters and $ZnGa_2O_4$:Cr^{3+} was utilized as a temperature probe.

5.3.2. Cr^{4+}

The use of chromium in the Cr^{4+} oxidation state for luminescence thermometry has only been described in one paper so far, due to the relatively stringent material parameters that the luminescent matrix must satisfy in order for Cr^{4+} luminescence to be observed. First of all, Cr^{4+} ions with the d^2 electron configuration preferentially occupy tetrahedral crystallographic positions. In addition, the small energy distance between the $^3B_2$ ($^3T_2$) and $^3B_1$ ($^3A_2$) levels makes the $^3B_2$ ($^3T_2$) level strongly susceptible to nonradiative luminescence quenching. In addition, the fact that these ions are characterized by d^2 electronic configurations results in the $^3T_2$ emitting level being very often efficiently quenched by non-radiative processes. In order to increase the energy distance between the $^3T_2$ and ground $^3A_2$ levels, host material with a high crystal field strength should be chosen. In addition, host materials with low phonon energies should favorably reduce the nonradiative depopulation of the excited level. Moreover, Cr^{3+} is thermodynamically a much more stable oxidation state than Cr^{4+}; hence, stabilizing Cr^{4+} involves a charge compensation procedure. Chen et al. developed a luminescence thermometer using the luminescence intensity of the $^3B_2$ ($^3T_2$) $\rightarrow$ $^3B_1$ ($^3A_2$) band occurring at approximately 1230 nm to measure the temperature in $Ca_2Al_2SiO_7$:Cr^{4+} [115]. Although the luminescence intensity decreased monotonically as a function of temperature, the resulting sensitivities were relatively low, reaching 0.61 %/K, with relatively low measurement reliability of the intensity-based luminescence thermometers (Fig. 9 h and i). Thermal shortening of the luminescence lifetime enabled the development of a lifetime-based thermometer with S_R = 0.25 %/K. In addition to this study, Cr^{4+} was used as an energy mediating ion between Nd^{3+} and Er^{3+} ions, increasing the sensitivity of the ratiometric luminescence thermometer to Nd^{3+} and Er^{3+}, but this issue is not the focus of the present work [116].

5.4. Manganese

Manganese luminescence centres occur in many oxidation states, from 1 + to 7 +. So far, the luminescence properties of manganese have been mostly exploited for Mn^{2+}, Mn^{3+}, Mn^{4+}, and Mn^{5+}. This great diversity in electronic configurations (from $3d^5$ for Mn^{2+} to $3d^2$ for Mn^{5+}) together with the possibility of Mn ion positioning in tetrahedrally and octahedrally coordinated crystallographic sites allows enables the tuning of the spectroscopic properties of manganese-activated materials over a wide spectral range. Hence, the immense popularity of luminescent thermometers using manganese ions is evidenced by the number of papers on this topic.

5.4.1. Mn^{2+}

Mn^{2+} ions with the d^5 electron configuration are among the most popular luminescent centres used for luminescence thermometry, along with Mn^{4+} [119]. The high susceptibility of the

Mn^{2+} emission intensity ($^4T_1 \rightarrow {}^6A_1$ electronic transition) to the temperature provides intensity-based luminescent thermometers with high relative sensitivities, such as those of ZnS:Mn^{2+} [120] or $Zn_2G_2O_4$:Mn^{2+} (S_R = 4.9 %/K) [121] and Ca_2SiO_4:Mn^{2+} (S_R = 4.18 %/K at 370 K) [122]. However, the reliability of the single band intensity thermometry approach is very low.

The spectral position of the $^4T_1 \rightarrow {}^6A_1$ emission band of Mn^{2+} ions depends on the strength of the crystal field acting on the Mn^{2+} ions and their coordination and varies among different host materials from the green to red spectral region. As most known Mn^{2+}-activated phosphors emit in the green spectral region, red emitting phosphors are typically utilized to obtain emission references in ratiometric intensity thermometry. Among the most popular solutions are Eu^{3+}-activated phosphors. These materials have low susceptibility to temperature quenching of emission, which results from a large separation in energy between the emitting $^5D_0$ level and the lower $^7F_6$ level of Eu^{3+}. The typical example of such a luminescent thermometer was presented by Yao et al., who employed Zn_2GeO_4:Mn^{2+}, Eu^{3+} [123]. The high temperature stability of the Eu^{3+} emission of this phosphor produced S_R = 1.96 %/K over the 293–353 K temperature range. In the case of GdF_3:Ce^{3+}, Mn^{2+}, Eu^{3+}, a much lower S_R = 1.32 %/K was achieved [124].

In addition to Eu^{3+}, many other co-dopant ions are used to develop ratiometric thermometers. Fu et al. presented very interesting results for $K_7ZnSc_2B_{15}O_{30}$:Mn^{2+} [125]. In this material, Mn^{2+} ions occupy the crystallographic positions of Zn^{2+} and Sc^{3+} ions. As the Mn^{2+} concentration increases, the luminescence intensity of the Mn^{2+} ions located at the Sc^{3+} position increases with a respect to the luminescence of Mn^{2+} at the Zn^{2+} sites. In addition, the luminescence intensities of Mn^{2+} ions in these two types of sites have different dependences on temperature changes, so the ratio of their emission intensities can be used as a thermometric parameter that reaches a sensitivity of S_R = 1.84 %/K at 520 K. Much lower sensitivity was reported when the Ce^{3+} emission intensity was used as a reference in $NaMgBO_3$:Ce^{3+}, Mn^{2+} (S_R = 0.69 %/K) [126]. In $Sr_2P_2O_7$:Mn^{2+}, Sn^{2+}, the emission intensity of Mn^{2+} was quenched much more rapidly at elevated temperatures than the emission band of Sn^{2+} [127]. Hence, the emission color changes from white at 293 K to blue at 623 K. Unfortunately, the authors only calculated S_A = 0.027 K^{-1} at 623 K. A very interesting effect was found for $(Ca,Sr)_{10}Li(PO_4)_7$:Ce^{3+}, Mn^{2+} at elevated temperatures [128]. In this material, the increase in temperature results in a slight decrease in the Ce^{3+} emission intensity and intensity enhancement and a spectral position shift of the Mn^{2+} emission band. Opposite trends of the luminescence signal dependences on temperature were exploited for the temperature readout. Unfortunately, the small thermal variation of LIR yielded a low S_R = 0.40 %/K at 470 K. Lojpur et al. exploited the defect emission as a reference signal for Mn^{2+}-based luminescent thermometers in $ZnSiO_4$:Mn^{2+} reporting S_R = 6.5 %/K at 573 K [129]. A similar approach was been proposed by Jiang et al [130] for the $(C_4H_9NH_3)_2MnI_4$.

The point symmetry of the crystallographic position often induces the oxidation state on which the manganese ions occur. Therefore, when both tetrahedral and octahedral crystallographic positions are present in the structure, the emission of both Mn^{2+} and Mn^{4+} may be observed. The difference between the electronic configurations of these luminescence centres affects the different sensitivities of their emission intensities to temperature changes, and ratiometric Mn^{2+}/Mn^{4+} thermometers can be developed. This exact approach was proposed in $Ba_{0.5}Sr_{0.5}Al_{11.93}O_{19}$: Mn^{2+}, Mn^{4+} yielding S_R = 4.37 %/K [131]. The Mn^{4+}-to-Mn^{2+} emission intensity ratio strongly depends on the host material composition. For a host material with a high molar ratio of Ba^{2+} ions, the Mn^{2+} emission intensity is dominant, whereas when the Sr^{2+} ions are dominant, the Mn^{4+} emission intensity is much stronger than that of Mn^{2+}. In this case, the high thermal stability of the Mn^{2+} emission with respect to the Mn^{4+} emission is responsible for a high S_R. As shown by Dong et al., the substitution of Ga^{3+} with Al^{3+} significantly decreases the luminescence intensity of Mn^{2+} with respect to Mn^{4+} in $Zn(Ga/Al)_2O_4$, which may affect the accuracy of thermometry at low temperatures in $ZnAl_2O_4$:Mn (Fig. 10a) [52]. Slightly lower values of S_R (S_R = 3.47 %/K) have been obtained using the same approach for $ZnGa_2O_4$:Mn^{2+}, Mn^{4+} [132]. In $LaM_{1-x}Al_{11-y}O_{19}$ (M = Mg, Zn) materials, a much higher S_R was obtained with zinc (S_R = 9 %/K) than with magnesium (S_R = 1.5 %/K) [133]. The higher resistance of Mn^{2+} emission to the thermal quenching of the zinc-based host material is responsible for the high sensitivity. For $Na_3Sc_2P_3O_{12}$: Eu^{2+}, Mn^{2+}, only S_R = 1.556 %/K [134] has been found due to the strong thermal susceptibility of the emission of both ions. However, as demonstrated previously, the luminescence intensity of Mn^{2+} is strongly dependent on temperature variations, and the intensity of the $^4T_1 \rightarrow {}^6A_1$ transition has been used as a luminescence reference with semiconductor quantum dots. The higher variability of the emission of quantum dots with respect to Mn^{2+} enabled the creation of a ratiometric thermometer with a sensitivity of S_R = 0.58 %/K [135].

The $^4T_1$ level of Mn^{2+} ions is known for its long excited state lifetime, which is very beneficial for luminescence thermal imaging as long lifetimes enable the use of long time delays and gates during signal acquisition. This in turn increases the imaging accuracy by improving the signal-to-noise ratio. It is therefore surprising that, to the best of our knowledge, only one study has dealt with luminescent thermometers based on the lifetime of this level. Specifically, Xue et al. demonstrated that the use of Mn^{2+} ion lifetimes in Zn_2GeO_4:Mn^{2+} provides S_R = 0.74 %/K [121].

The strategy of mixing two phosphors discussed for Cr^{3+} has been also employed for Mn^{2+} ratiometric thermometers. Gong et al. exploited the g-C_3N_4 emission intensity as a reference signal for a Mn^{2+}-based temperature probe in a $Ca_9Y(PO_4)_7$:Ce^{3+}, Mn^{2+}/g-C_3N_4 composite, achieving S_R = 1.673 %/K at 547 K [136]. Another illustration of the mixing of two phosphors is the glass ceramic with GdF_3:Tm^{3+} and Ga_2O_3:Mn^{2+} [137]. The maximum relative sensitivity obtained with this probe was 1.78 %/K at 543 K. Relatively good thermometric parameters were obtained for the mixture of Zn_2SiO_4 Mn^{2+}–Gd_2O_3 Eu^{3+} [138] Here, S_R = 3.05 %/K resulted from the small activation energy for the nonradiative depopulation of the $^4T_1$ state and, thus, the efficient thermal quenching of the Mn^{2+} emission intensity.

5.4.2. Mn^{3+}

The d^4 electronic configuration of Mn^{3+} results in the splitting of the ^5E ground state by the Jahn-Teller effect into two components: $^5E'$ and $^5E''$. The displacement in the wavevector domain between the ground levels and emitting $^5T_2$ state results in the broad emission band associated with the $^5T_2 \rightarrow {}^5E$ electronic transition. Because it is relatively difficult to stabilize Mn^{3+} than the much more thermodynamically favourable Mn^{2+} and Mn^{4+}, the number of reports devoted to Mn^{3+} luminescence and thermometry is very small. Trejgis et al. firstly reported using the Mn^{3+} emission intensity for temperature sensing, employing YAG:Mn^{3+}, Mn^{4+} and YAG: Mn^{3+}, Mn^{4+}, Nd^{3+}[139]. The strong thermal variation of the Mn^{3+} emission intensity and weak thermal dependence of the Nd^{3+} emission enabled the development of a ratiometric thermometer with S_R = 2 %/K at 250 K, whereas Mn^{3+}-to-Mn^{4+} LIR enables temperature readout with S_R = 1.6 %/K at 220 K. The luminescence decay time of the $^5T_2$ state was found to be drastically shortened above 220 K. Thus, a lifetime-based thermometer of high sensitivity was developed using $Y_3Al_5O_{12}$:0.01 %Mn with S_R = 2.69 %/K at 350 K. The extension of this study involved the evaluation of the role of the host material composition on the lifetime-based

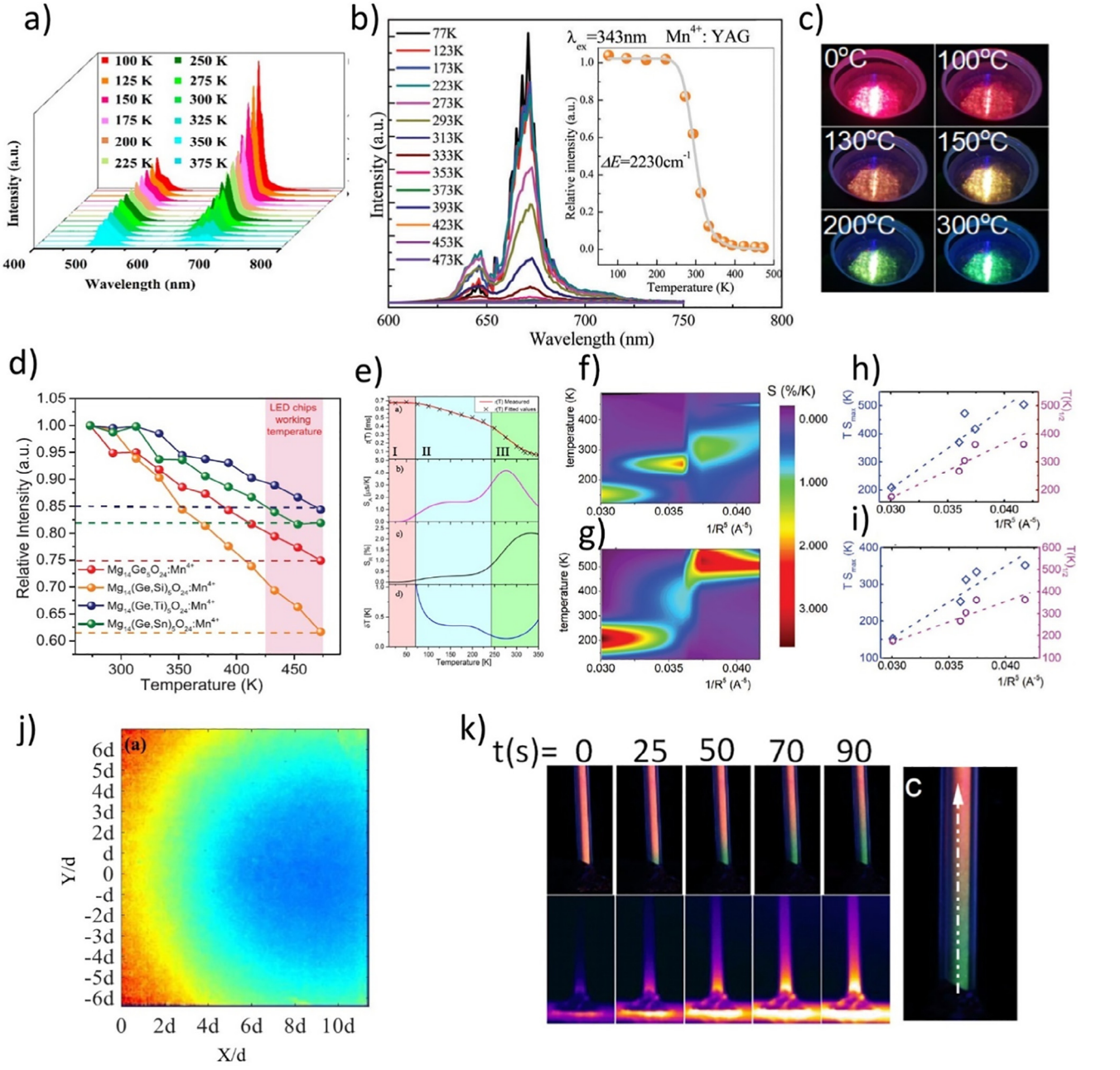

Fig. 10. Temperature-dependent emission spectra of $ZnGa_2O_4$:Mn^{2+},Mn^{4+} -a) [52]; thermal dependence of emission spectra and integrated emission intensity of YAG:Mn^{4+} - b) [80]; -images of the emitted light by the $Sr_4Al_{14}O_{25}$:Mn^{4+},Tb^{3+} luminescent thermometer at different temperatures - c) [53]; The relative integrated intensity of the four samples as a function of working temperature (273–473 K) in $Mg_{14}Ge_5A_{0.5}O_{24}$:Mn^{4+} (A = Si^{4+}, Ti^{4+}, Sn^{4+}) -d) [150]; The temperature dependence of the Mn emission lifetime (symbols); the red line represent fit, the absolute and relative sensitivity respectively, and the temperature resolution of thermometry in $Li_{1.8}Na_{0.2}TiO_3$:Mn^{4+} -e) [161]; the influence of the metal–oxygen distance on the relative sensitivity of the Mn^{4+} rise time based luminescent thermometers -f) [33]; and the decay time based thermometers-g) [33]; the influence of the temperature at which S_{Rmax} of the rise time based -h) [33]; and decay time based thermometers- in YAG:Mn^{3+},Mn^{4+}, GAG:Mn^{3+},Mn^{4+}, GGG:Mn^{3+}, Mn^{4+}, LuAG:Mn^{3+},Mn^{4+},i) [33]; Temperature measurement results of jet impingement cooling using the Mg_4FGeO_6:Mn^{4+}-based rise time method: temperature cloud chart-j) [163]; comparison of the images of the light emitted by $Sr_4Al_{14}O_{25}$:Mn^{4+},Tb^{3+} thermographic phosphor (upper images) and the thermal cameras (lower images) during heat diffusion –k) [53].

thermometer performance with $G_3Al_5O_{12}$:Mn^{3+}, Mn^{4+}; $Ga_3Ga_5O_{12}$: Mn^{3+}, Mn^{4+}; $Lu_3Al_5O_{12}$:Mn^{3+}, Mn^{4+}; $Y_3Al_5O_{12}$:Mn^{3+}, Mn^{4+}; and $YAlO_3$:Mn^{3+}, Mn^{4+} [33]. In this group of nanocrystals, upon excitation in the absorption band of Mn^{3+}, the kinetics of the Mn^{4+} emission revealed the rise time associated with the Mn^{3+} → Mn^{4+} energy transfer. It was found that the temperature at which the rise time was shortened by half ($T_{1/2}$) was sublinearly correlated with the CFS of the host material. The highest value of S_R based on the rise time was achieved for $Gd_3Al_5O_{12}$:Mn^{3+}, Mn^{4+} (S_R = 2.08 %/K at 249 K). Wang et al. employed a very similar approach to that reported by Trejgis et al. using $Ca_3Ga_2Ge_3O_{12}$: Mn^{3+}, Mn^{4+}, which yielded S_R = 6 %/K at 33 K [140]. Jahanbazi et al. developed a Mn^{3+}/Tb^{3+} ratiometric thermometer with $La_2Zr_2O_7$:Tb^{3+}, Mn^{3+} nanoparticles that presented S_R = 1.82 %/K at 298 K [141].

5.4.3. Mn^{4+}

The most extensively investigated manganese luminescence centre in thermometry is Mn^{4+} (d^3 electronic configuration) due to its well-known red/deep red emission associated with the

$^2E \rightarrow {}^4A_2$ electronic transition. The Mn^{4+} ions always experience a strong crystal field and their ^2E state energy only weakly depends on the host material composition. Thus, the emission band of Mn^{4+} is centred between 617 nm ($NaSiF_6$:Mn^{4+} [142]) and 723 nm ($SrTiO_3$:Mn^{4+} [143]). The close proximity of the ^2E and $^4T_2$ excited states facilitates their thermal coupling and, thus, the efficient quenching of the ^2E emission intensity and shortening of the ^2E lifetime at elevated temperatures. In the case of Mn^{4+}, three ratiometric temperature sensing approaches have been reported: (i) the LIR of the anti-Stokes to Stokes part of the $^2E \rightarrow {}^4A_2$ emission band, (ii) the LIR between ^2E and $^4T_2$ emissions, and (iii) the ratio of this band to the emission intensity of the reference signal. In the first case, relatively low sensitivities are usually reported. Cai et al. [144] proposed this approach in Y_2MgTiO_6:Mn^{4+}, achieving 0.14 %/K at 153 K. Yang et al. compared the thermometric performance of $Mg_{28}Ge_{7.55-x}Ga_xO_{32}F_{15.04}$:$Mn^{4+}$ upon direct and sideband excitations [145]. When side band excitation was used, the emission intensity increased with temperature, which resulted in the thermal enhancement of S_R from 0.42 %/K for λ_{exc} = 410 nm (direct excitation) to 0.68 %/K for λ_{exc} = 460 nm (sideband excitation) in the anti-Stokes to Stokes LIR approach. Similarly, Yang et al. found S_R = 0.42 %/K in $SrAl_{12}O_{19}$:Mn^{4+} [146]. The emission intensity ratio of the anti-Stokes to Stokes part of the $^2E \rightarrow {}^4T_2$ emission band in $Cs_2WO_2F_4$:Mn^{4+} provided S_R = 0.21 %/K at 167 K [147]. Cai et al. performed systematic studies of the influence of the excitation density on the thermometric properties of $Na_2WO_2F_4$:Mn^{4+} [148]. For this purpose, three intensities ratios were considered: those between the (i) anti-Stokes part of the spectrum and the zero-phonon line, (ii) anti-Stokes part and Stokes part of the spectrum, and (ii) anti-Stokes part of the spectrum and the integral intensity of the zero phonon line and Stokes part of the spectrum. Due to the light-induced heating effect on the thermal equilibrium between the ^2E and $^4T_2$ states, S_R was found to be slightly dependent on the excitation density (a change in excitation density by approximately 1 W/cm^2 decreased S_R by approximately 10 %). The highest S was found in the first case with S_R = 0.658 %/K at 193 K. The detailed analysis of the thermometric parameters of Mg_4FGeO_6:Mn^{4+} performed by Fuhrmann et al. revealed that the lifetime approach was superior in terms of accuracy, precision, and cross-sensitivity compared to the LIR method [149]. Liang et al. demonstrated how the precise optimization of the matrix stoichiometry and geometry of the polyhedron occupied by Mn^{4+} ions by cation substitution enables the modulation of the thermometric properties of the phosphor (Fig. 10d) [150]. This comprehensive research enabled the selection of the optimal phosphor that enabled the achievement of the highest sensitivity ever reported for a thermometer based on the anti-Stokes to Stokes part of the $^2E \rightarrow {}^4A_2$ emission band in $Mg_{14}Ge_5Ti_{0.5}O_{24}$:$Mn^{4+}$ (S_R = 2.71 %/K at 97 K). Much higher sensitivities were achieved when the Mn^{4+} to Ln^{3+} emission intensity ratio was considered as a thermometric parameter. Although only S_R = 0.7 %/K at 303 K for $Lu_3Al_5O_{12}$:Eu^{3+}, Mn^{4+} [151] and S_R = 0.89 %/K at ~ 520 K for La_2LiSbO_6:Mn^{4+}, Eu^{3+} were reported [152] S_R = 2.43 %/K and S_R = 2.75 %/K were found for $LaTiSbO_6$:Mn^{4+} using the ratiometric and lifetime approaches [153]. Chen et al. found a very high thermal variability of the Ce^{3+} to Mn^{4+} emission intensity ratio in $Lu_3Al_5O_{12}$:Ce^{3+}, Mn^{4+}, and rapid thermal quenching of the Mn^{4+} emission intensity above 25 K resulted in S_R = 4.37 %/K at 350 K [154]. This quenching was reflected in the shortening of the ^2E state lifetime with S_R = 3.22 %/K at 350 K. S_R = 2.18 %/K was found for $SrLaLiTeO_6$:Mn^{4+}, Dy^{3+} [51] and S_R = 4.3 %/K was obtained for $Lu_3Al_5O_{12}$:Mn^{4+}/Tb^3 [155]. As has been shown by Chen et al., even though Cr^{3+} and Mn^{4+} have the same electronic configuration, the difference in the energy separation between the ^2E and $^4T_2$ states results in a much higher S_R for YAG:Mn^{4+}, Eu^{3+} and YAG:Mn^{4+}, Dy^{3+} of S_R = 4.81 %/K and S_R = 3.16 %/K, respectively, compared to S_R = 2.43 %/K and S_R = 2.32 %/K for the Cr^{3+}-based counterparts (Fig. 10b) [80]. Using the luminescence intensity ratio as the ratio between the integrated intensities of the Eu^{3+} $^5D_0 \rightarrow {}^7F_1$ transition and the Mn^{4+} $^2E \rightarrow {}^4A_2$ manyfold, a maximum relative sensitivity of 5.06 %/K at 321 K was found in YAG:Mn^{4+}, Eu^{3+} nanoparticles [156]. In the case of $SrLaLiTeO_6$:Mn^{4+}, Dy^{3+}, the LIR between Mn^{4+} and Dy^{3+} emissions provides S_R = 1.6 %/K [51]. As was already stated in this manuscript, the lanthanide ions not only provide luminescence reference information, but also are responsible for the energy transfer channel that causes the increase in the quenching rate of the Mn^{4+} emission intensity. In $LaGaO_3$:Mn^{4+}, Sm^{3+}, the presence of Sm^{3+} co-dopant led to an increase in the thermal quenching rate of Mn^{4+}, and $Mn^{4+} \rightarrow Sm^{3+}$ energy transfer caused thermal enhancement of the Sm^{3+} emission intensity [157]. The outcome of these processes is the change in the emission color from red to yellow at elevated temperatures and S_R = 2.09 %/K at 423 K. Piotrowski et al. were the first to demonstrate that Mn^{4+} ion emission can be used for thermal imaging (Fig. 10c and k) [53]. Using the strong temperature quenching of the luminescence in $Sr_4Al_{14}O_{25}$:Mn^{4+}, Tb^{3+}, the authors observed a color change of the emitted light from red (R; for temperatures below 273 K) to green (G; for temperatures above 473 K). This color change occurred due to the different thermal quenching of the green (Tb^{3+}) and red (Mn^{4+}) emissions and provided the opportunity to detect these emissions separately in the G and R channels of a commercial digital camera. Therefore, using the proposed approach, a digital camera can be utilized to read temperature without the need for additional optical filters. The proposed solution enabled dynamic analysis of the heat diffusion in a heated quartz tube filled with a luminophore. The maximum sensitivity recorded was S_R = 2.8 %/K at 423 K. In addition, to quantify the thermochromic performance, the authors determined the sensitivities based on the variations of the chromatic coordinates (CIE 1931) of $S_R(x)$ = 0.6 %/K and $S_R(y)$ = 0.4 %/K. On the other hand, when the Bi^{3+}, Mn^{4+} co-doped system ($Ca_{14}Al_{10}Zn_6O_{35}$:Bi^{3+}, Mn^{4+}) was analysed, the Mn^{4+} emission intensity revealed a much lower thermal susceptibility than the Bi^{3+} emission intensity [158]. Thus, S_R = 1.21 %/K was reported. Zhang et al. [159] employed a similar approach for Gd_2ZnTiO_6:Bi^{3+}, Mn^{4+} (S_R = 2.4 %/K).

It is worth noting that the highest values of S_R for lifetime-based luminescence thermometers with Mn^{4+}-doped phosphors have been found in the physiologically relevant temperature range (273–350 K) [46,47,144,146,150,153,155,160–163]. Considering that their emission bands are located in the spectral range of the first biological transparency window, Mn^{4+}-doped thermometers are interesting from a biomedical application perspective. However, the excitation bands of Mn^{4+} in the UV range limit the application potential of this kind of temperature probe. Dramicanin et al. performed detailed studies on the evaluation of the thermometric performance of lifetime-based thermometry in Li_2TiO_3:Mn^4 [162]. According to their results, this phosphor can be applied in the 10–350 K temperature range with the best performance in the biologically relevant temperature range where S_R = 3.21 %/K was obtained. Importantly, the calibration curve of lifetime versus temperature perfectly fits the cross-over model. The partial substitution of the lithium ions with sodium ions ($Li_{1.8}Na_{0.2}TiO_3$:Mn^{4+}) negatively affected the thermometric performance of this phosphor (S_R = 2.27 %/K at 330 K) (Fig. 10e) [161]. Another representative of the titanate family (Mg_2TiO_4:Mn^{4+} [164]) yielded a much smaller thermal variation of the ^2E state lifetime with S_R = 0.8 %/K at 353 K. Cai et al. investigated the rise time of the Mn^{4+} kinetics in $MgFGeO_6$:Mn^{4+} phosphor as a thermometric parameter (Fig. 10j) [163]. The faster population of the ^2E excited state at elevated temperature resulted in the subexponential shortening of the rise time as a function of temperature, yielding S_R = 0.29 %/K at 475 K with a temperature uncertainty of approximately 3 K in the 300–675 K

temperature range. Although the rise time was found to be independent of the excitation duration, some shortening of its value with the excitation density was found. This characteristic could have affected the reliability of temperature determination when fluctuation in the excitation occurred during the experiment. Nevertheless, the authors proved the high application potential of this approach in a 2D experiment investigating the temperature distribution from steady jet impingement on a copper plate. Kissel et al. also used the decay of the Mn^{4+} emission in this compound for temperature readout [165]. Efficient quenching of the ^2E state in $Lu_3Al_5O_{12}:Mn^{4+}$ enables the achievement of one of the highest relative sensitivities among Mn^{4+} lifetime-based thermometers (S_R = 6.35 %/K at 345 K) [46]. However, very high values were reported also for $Y_3Ga_5O_{12}:Mn^{4+}$ (S_R = 6.09 %/K) and $Lu_3Ga_5O_{12}:Mn^{4+}$ (S_R = 5.14 %/K) [166]. As Mn^{4+} occupies the octahedral crystallographic site, its spectroscopic and, thus, thermometric parameters can be modified to some extent by the CFS. As shown in the series of garnet materials (GAG:Mn^{3+}, Mn^{4+}, GGG:Mn^{3+}, Mn^{4+}, LuAG:Mn^{3+}, Mn^{4+}, and YAG:Mn^{3+}, Mn^{4+}) and perovskite ($YAlO_3$:Mn^{3+}, Mn^{4+}) the linear correlation between the thermal quenching temperature and, thus, the temperature at which the maximum S_R can be obtained is a linear function of the CFS and reversibly proportional to R^{-5} (Fig. 10f-i) [33]. For $BaLaMgNbO_6:Dy^{3+}$, Mn^{4+}, S_R = 2.43 %/K [167] and S_R = 1.82 %/K were reported for the for lifetime and ratiometric approaches, whereas for $Sr_{0.5}Ba_{0.5}Al_{12}O_{19}:Mn^{4+}$, S_R = 4.48 %/K for Mn^{4+} [131]. The thermometric properties on the kinetics of the ^2E state in $Li_4Ti_5O_{12}:Mn^{4+}$ were found to be beneficial for the biologically relevant temperature range, with S_R = 2.6 %/K at 330 K [168].

By mixing $Y_2O_3:Ho^{3+}$ with $MgTiO_4:Mn^{4+}$, Sekulic et al. obtained S_R = 4.61 %/K with a temperature uncertainty around 0.1 K [169]. Even higher relative sensitivity was reported for a $Y_2O_3:Dy^{3+}$ and $Li_2TiO_3:Mn^{4+}$ mixture, for which S_R = 4.34 %/K with the ratiometric approach and S_R = 6.67 %/K with the ^2E lifetime-based approach [170].

Glais et al. reported a multiparametric luminescent thermometer based on $MgTiO_3:Mn^{4+}$ in which three different thermometric parameters were analysed: (1) the luminescence intensity ratio between the R_1 and R_2 lines of Mn^{4+}, (2) the emission intensity ratio between the ^2E and $^4T_2$ emission bands, and (3) the lifetime of the ^2E state [171]. The best thermometric performance was found for the lifetime-based approach, with S_R = 4.1 %/K at 277 K and 0.025 K temperature determination uncertainty, whereas only S_R = 0.9 %/K and S_R = 1.2 %/K were obtained with the first and second approaches. A multiparametric thermometer, reported by Trejgis et al., was developed based on $SrTiO_3:Mn^{4+}$ and $SrTiO_3:Mn^{4+}$, Ln^{3+} and showed that the Mn^{4+} emission intensity, ^2E to $^4T_2$ emission intensity ratio, and lifetime of the ^2E state could be applied for temperature sensing with S_R = 8.67 %/K, S_R = 4.5 %/K, and S_R = 3.5 %/K, respectively [47]. When the LIR of Mn^{4+} to Eu^{3+} was used, S_R = 5.64 %/K was achieved. However, an interesting effect was noticed when Ln^{3+} was used as a co-dopant to substitute the Sr^{2+} sites. The change compensation effect led to the stabilization of the Ti^{3+} state [160]. As Ti^{3+} is actively luminescent, its presence in the nanocrystals provided an additional channel for the nonradiative depopulation of the ^2E state. Therefore, in follow-up studies, Piotrowski et al. proved that the sensitivity of lifetime-based thermometers could be enhanced from S_R = 3.5 %/K for $SrTiO_3:Mn^{4+}$ to S_R = 3.87 %/K for $SrTiO_3:Mn^{4+}$, Lu^{3+} nanocrystals. The cooperation of $Mn^{4+} \rightarrow Ti^{3+}$ and $Mn^{4+} \rightarrow Er^{3+}$ energy transfer produced S_R = 5.1 %/K for $SrTiO_3:Mn^{4+}$, Er^{3+}.

5.4.4. Mn^{5+}

In recent years, an increased interest in luminescence thermometry using the luminescence properties of Mn^{5+} ions has been observed. Mn^{5+} is an interesting luminescent centre as it provides an intense and a narrow emission band in the spectral range from 1100 nm to 1300 nm, which corresponds to the second biological optical transparency window, and its luminescence can be excited by wavelengths from the first optical window. This feature is of great importance for potential biological applications. To facilitate Mn^{5+} emission, the material needs to provide both the tetrahedral environment for Mn^{5+} and a sufficiently large energy bandgap compared to the Mn^{5+} transitions' energies. More importantly, the host material must provide the stabilization of the Mn 5+ valence state, which imposes more constraints on the materials' structure and composition than the 2+ and 4+ valance states. For these reasons, most of the host materials for Mn^{5+} emission contain electropositive ions such as alkaline earth metals, and PO_4^{3-} and VO_4^{3-} groups (or SiO_4^{4-} group with a charge compensation). Gschwend et al. proposed a ratiometric thermometer based on the intensity ratio of the Mn^{5+} ^1E state emission and vibronic emission in the $Ba_3(PO_4)_2:Mn^{5+}$ and found S_R = 0.43 %/K [172]. The authors also provided experimental confirmation of the usability of this phosphor for deep tissue imaging. Ristic et al. proved that the thermal variability of the ^1E state in $(Sr/Ba)_3(PO_4)_2:Mn^{5+}$ can be used for lifetime-based thermometry. By replacing Sr^{2+} with Ba^{2+}, the spectral position of the $^1E \rightarrow {}^3A_2$ emission band can be shifted from 1173 nm to 1191 nm [173]. The modification of the CFS associated with this substitution modifies the thermal shortening decay rate of the ^1E emission. The highest S_R = 1 %/K was obtained for $Ba_3(PO_4)_2:Mn^{5+}$. As discussed in [172 and 173], temperature can be read from various features of Mn^{5+} photoluminescence. These can be steady-state features like emission intensity, peak position, and emission intensity ratio or the time-resolved like ^1E level lifetime. Regarding the complexity and the cost of equipment, time-integrated measurements are favorable to time-resolved ones since they are simpler and cheaper. The ratio of intensities of ^1E and vibronic emissions [172] and ^1E level lifetime provide self-referencing, while other read-outs require the external reference. In principle, lifetime-based thermometry has lower uncertainty in measurement compared to intensity-based measurements, and, thus, a better temperature resolution can be achieved. However, the uncertainty will be determent from the performance of equipment used in an actual experiment.

5.5. Iron

The luminescence properties of iron ions are rarely described in the literature and mostly limited to the emission of Fe^{3+}. Generally, Fe^{3+} is considered a luminescence quencher in optical spectroscopy. Recently, Fe^{3+}-activated phosphors have garnered attention for broadband NIR emitting phosphor applications [174–176] as well as for luminescence thermometry. Kniec et al. reported that in $LiAl_5O_8$, Fe^{3+} ions (with a d^5 electron configuration) occupy the octahedral Al^{3+} crystallographic positions and their intense emission associated with the $^4T_1$ (^4G) $\rightarrow {}^6A_1$ (^6S) electron transition strongly decreases with increasing temperature. However, the sensitivity of the $LiAl_5O_8:Fe^{3+}$, Nd^{3+} ratiometric thermometer reached a maximum of S_{Rmax} = 0.56 %/K at 193 K. As suggested by the authors a significant advantage of this thermometer is its very intense luminescence [177]. However, neither luminescence brightness nor luminescence quantum efficiency was not presented to support this claim. Much higher sensitivity values were obtained for garnet materials co-doped with Fe^{3+}, Cr^{3+}, and Nd^{3+}: 5.90 %/K (at 373 K) for $Lu_3Ga_5O_{12}$, 1.68 %/K (at 323 K) for $Y_3Ga_5O_{12}$, and 1.57 %/K (at 323 K) for $Ga_3Ga_5O_{12}$. In addition, the maximum sensitivity of the ratiometric luminescence thermometer based on the ratio of the emission intensity of Fe^{3+} to Nd^{3+} decreased almost linearly with increasing CFS, which was explained based on the Tanabe-Sugano diagram for the d^5 configuration [176]. On the other hand, in $MaI_4O_7:Fe^{3+}$ (M = Ca, Sr, Ba)

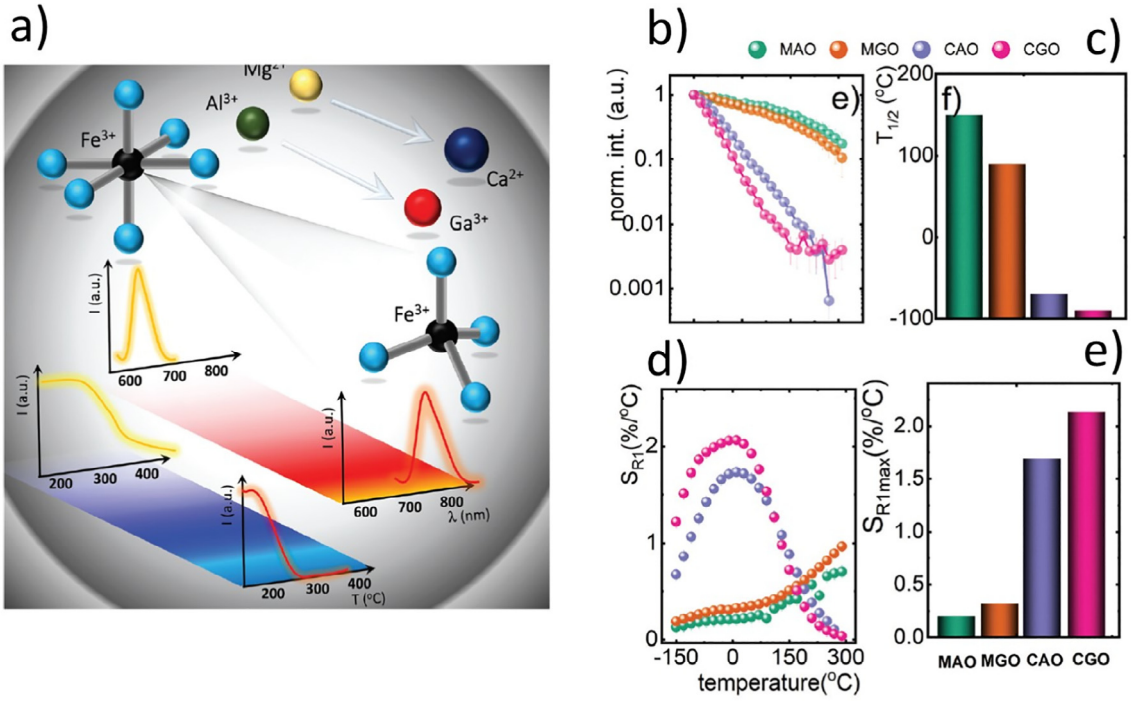

Fig. 11. Schematic visualization of the modification of the spectroscopic and thermometric properties of the Fe^{3+} based luminescence thermometers by the change of the host material stoichiometry in $AB_2O_4:Fe^{3+}$ (A = Mg, Ca, B = Al, Ga)-a) [175]; the Fe^{3+} emission intensity as a function of temperature in $MgAl_2O_4:Fe^{3+}$, $MgGa_2O_4:Fe^{3+}$, $CaAl_2O_4:Fe^{3+}$, and $CaGa_2O_4:Fe^{3+}$ -b) [175]; the temperature at which the emission intensity is at half the initial value in $MgAl_2O_4:Fe^{3+}$, $MgGa_2O_4:Fe^{3+}$, $CaAl_2O_4:Fe^{3+}$, and $CaGa_2O_4:Fe^{3+}$ - c [175]); the relative sensitivities value of Fe^{3+}-based spinel luminescence thermometers at 273 K in $MgAl_2O_4:Fe^{3+}$, $MgGa_2O_4:Fe^{3+}$, $CaAl_2O_4:Fe^{3+}$, and $CaGa_2O_4:Fe^{3+}$ -d) [175]; the comparison of the relative sensitivity values for different host material compositions value in $MgAl_2O_4:Fe^{3+}$, $MgGa_2O_4:Fe^{3+}$, $CaAl_2O_4:Fe^{3+}$, and $CaGa_2O_4:Fe^{3+}$ -e) [175].

[174] nanocrystals Fe^{3+} ions occupy the tetrahedral crystallographic positions, resulting in emission band shifts toward longer wavelengths. For $MaI_4O_7:Fe^{3+}$, four thermometric approaches were evaluated: an intensity-based method, a ratiometric technique utilizing the emission intensities of two different Fe^{3+} sites, a ratiometric approach using the Fe^{3+} to Tb^{3+} emission intensity ratio, and lifetime-based thermometry. The $BaAl_4O_7:Fe^{3+}$ nanocrystals achieved the best thermometric performance with almost all approaches (S_R = 3.52 %/K at 180 K and S_R = 1.57 %/K at 258 K for the Fe^{3+}/Fe^{3+} ratiometric and Fe^{3+} lifetime-based approaches, respectively) [174]. The ionic size of the ions constituting the host material predefines the crystallographic sites occupied by Fe^{3+} ions. It was shown that in $AB_2O_4:Fe^{3+}$ (A = Mg, Ca; B = Al, Ga), stoichiometry modification from $MgAl_2O_4:Fe^{3+}$ to $CaGa_2O_4:Fe^{3+}$ leads to a change in the crystallographic position substituted by Fe^{3+} from octahedral to tetrahedral (Fig. 11a and b). This modification significantly affects the thermal stability of the Fe^{3+} emission intensity and the spectral position of the Fe^{3+} emission band. As much lower energetical separation between the ground and excited states is expected for tetrahedral symmetry compared to octahedral symmetry, the emission band of Fe^{3+} in the former case is redshifted with respect to the octahedral counterpart. Moreover, the Fe^{3+} emission intensity is quenched more efficiently in $CaGa_2O_4:Fe^{3+}$ and $CaAl_2O_4:Fe^{3+}$ than in $MgAl_2O_4:Fe^{3+}$ and $MgGa_2O_4:Fe^{3+}$. Therefore the maximum S_R was found to be S_R = 2.08 %/K at 263 K for a $CaGa_2O_4:Fe^{3+}$, Tb^{3+} ratiometric thermometer (Fig. 11c-e) [175].

5.6. Cobalt

Literature regarding the use of cobalt ion luminescence for luminescence thermometry is limited, to the best of our knowledge, to one paper discussing $MgAl_2O_4:Co^{2+}$ and $MgAl_2O_4:Co^{2+}$, Nd^{3+} nanocrystals [178]. This gap is probably due to the relatively weak emission intensity of Co^{2+}. Kobylinska et al. [178] showed that only one emission band associated with the $^2E_g \rightarrow {}^4A_{2f}$ electronic transition could be observed in the emission spectrum of the investigated nanocrystal and that it was completely quenched at 573 K (Fig. 12a). An analysis of the thermal quenching rate of Co^{2+} luminescence performed as a function of the Co^{2+} dopant concentration and nanoparticle size revealed the fastest thermal quenching rate for the lowest particle size (~12 nm in diameter). However, the maximum relative sensitivity of the ratiometric luminescent thermometer based on the Co^{2+}/Nd^{3+} ($^4F_{3/2} \rightarrow {}^4I_{9/2}$) emission intensity ratio was too low to employ this material for reliable temperature measurement (S_R = 0.28 %/K in the 163–373 K temperature range for $MgAl_2O_4$:0.01 $\%Co^{2+}$, 5 $\%Nd^{3+}$ nanocrystals).

5.7. Nickel

The luminescence properties of nickel ions are related to the Ni^{2+} oxidation state of the d^8 electronic configuration. Only few Ni^{2+} based phosphors have been described to date. This is due to some difficulties in obtaining intense luminescence of these ions. There are several criteria of the host material that facilitate achieving the emission of Ni^{2+} ions. The first of them is the presence of a crystallographic position in the host material of 2 + valence, which could be occupied by Ni^{2+} ions. Although Ni^{2+} ions can occupy both octahedral and tetrahedral positions, due to the higher energy splitting between the ground and excited levels, those matrices in which Ni^{2+} ions could be octahedrally coordinated are preferred for phosphor development. In addition, increasing the strength of the crystal field positively affects the luminescence intensity of Ni^{2+} ions. However, it is associated with a blue-shift of the emission band maximum [179]. The advantages of using Ni^{2+} as a luminescent dopant are mainly related to the spectral localization of its emission band associated with the $^3T_{2g}(F) \rightarrow {}^3A_{2g}$ (F) electron transition in the range of the second biological optical window. This feature is important from the perspective of potential

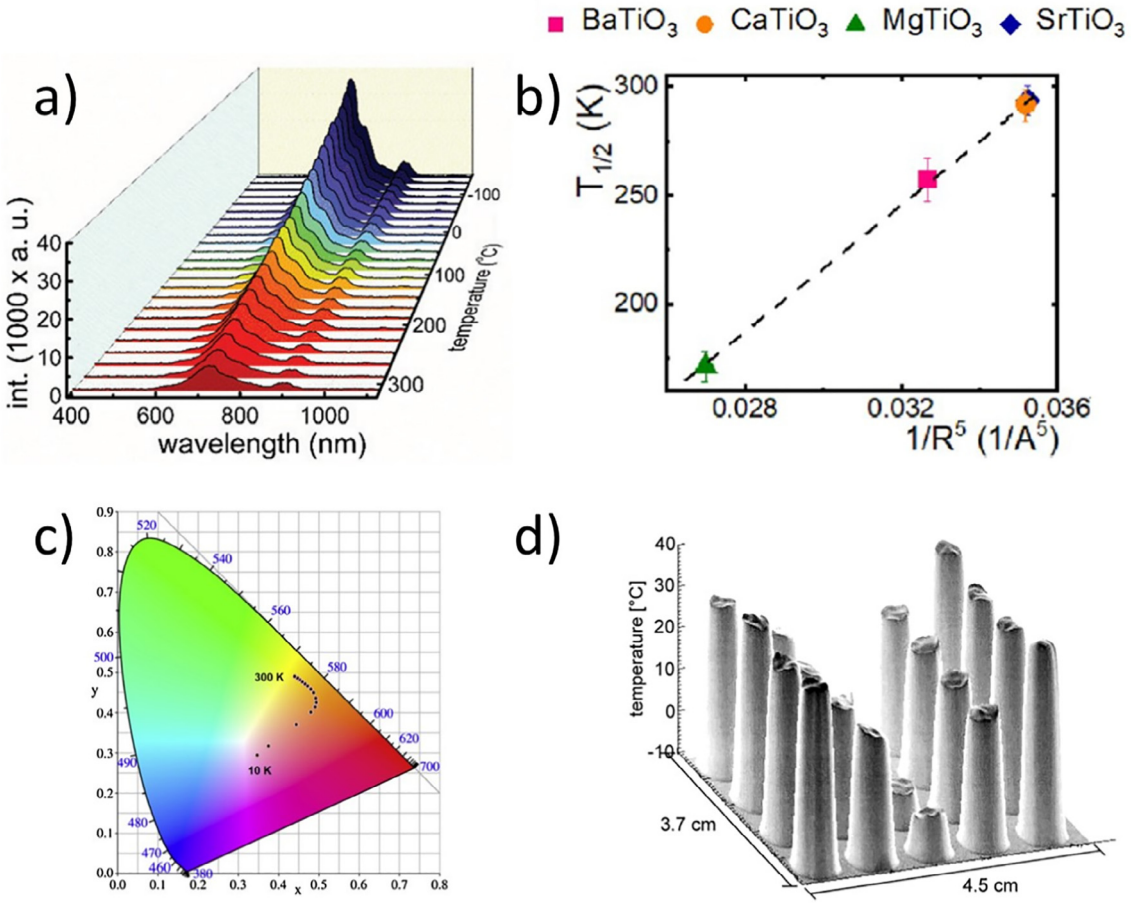

Fig. 12. Representative emission spectra of $MgAl_2O_4:Co^{2+},Nd^{3+}$ nanocrystals measured as a function of temperature upon λ_{exc} = 266 nm -a) [178]; the influence of temperature at which intensity decrease to the half of its initial value in the function of $1/R^5$ for $SrTiO_3$: 0.1 % Ni^{2+}, $CaTiO_3$: 0.1 % Ni^{2+}, $BaTiO_3$: 0.1 % Ni^{2+}, $MgTiO_3$: 0.1 % Ni^{2+} nanocrystals -b) [179]; thermally induced change of the chromatic CIE coordinates calculated for $[Cu_4I_4(Pz)_2]_n$ (Pz = [1,4-bis(4-pyridylmethyl)piperazine]) -c) [180]; decay time image of a section (5x4 wells) of a microtiterplate. The bottom of the wells is coated with the temperature-sensitive coating Ru(phen) and the wells are filled with water of defined temperature (273 K, 293 K, and 303 K) -d) [181].

biomedical applications as the absorption and scattering of light are reduced in this spectral range. Matuszewska et al. (Fig. 12b) [179] demonstrated that the variation in composition of $ATiO_3$: Ni^{2+} materials (A = Sr, Ca, Mg, Ba) strongly modifies the crystal field, leading to a change in the energy gap between the $^3T_{2g}$(F) and $^3A_{2g}$ (F) levels. Thus, the location of the emission band maximum can be shifted from 1210 nm for $SrTiO_3:Ni^{2+}$ to 1700 nm for $MgTiO_3:Ni^{2+}$. However, there is also a decrease in emission intensity, which is a logical outcome of the higher probability of non-radiative depopulation of the excited level with a smaller difference between the excited and ground energy levels. In addition, the luminescence thermal quenching rate varied as a function of the CFS. The temperature at which the luminescence intensity decreased to half its initial value increased linearly with increasing CFS. This behaviour enables modulation of the thermometer performance based on the Ni^{2+} emission intensity. Several features of these luminescent thermometers have been considered for temperature sensing, including the emission intensity, band shift, and LIR of Ni^{2+} to Er^{3+} ions. The highest sensitivity values were obtained using the LIR approach for SrTiO3:Ni^{2+}, Er^{3+} of S_R = 5.8 %/K at 423 K [182].

5.8. Cupper

The Cu clusters and Cu ions are primarily exploited as molecular luminescent thermometers [183–185]. In 2009., *N. Fujino et al.* have presented a molecular thermometer consisting of the CuTTP (tetraphenyl-21H,23H-porphityne copper (II)) and polystyrene composite in forms of films and fibers [183]. Since the intensity of the emission band at 780 nm decreased in respect to the one centered at 653 nm the ratiometric luminescent thermometers were developed, however without the evaluation of their thermometric performances (the relative sensitivity and temperature resolution). Authors confirmed the similar thermal evolution of LIRs in when thermometer was in an air and water and applied it to measure the temperature of the organic light emitting diode (OLED) during the operation. The comparison with the reference thermocouple measurement revealed up to 44 K difference in temperature when 450 mA/cm^2 electrical current was applied to OLED. The lower value of temperature measured by a thermocouple was explained by the small value of heat conductivity of the glass that covers OLED on which the thermocouple was mounted. The authors argued that the large deviation of temperature measured by thermocouple from the true value would be reduced if the diode operation time is extended, but they did not provide the experimental verification. In addition, the limitation of the experiment was the fact that the calibration curve was made in the range of 293–343 K, while the temperature reading during the diode's operation was at 383 K. The other example of Cu-based molecular thermometer is a complex structure, composing of five Cu atoms attached to three conjugated dianionic cationic ligands – EtNC(S)$PPh_2NPPh_2C(S)NEt^-$, which creates the Cu_5 cluster [184]. The

thermometric performance of these lifetime based luminescent thermometers has been evaluated in the 228–353 K temperature range showing the S_R = 0.5 %/K. The performance of the temperature readout from emission intensity was investigated with an 365 nm excitation. This excitation leads to the population of the singlet excited state S_1 after which S_1-S_6 excited states are populated according to the Boltzmann's law with having long emission decay. To this aim Cu_5 clusters were spotted on different types of surfaces, aluminum foil, cotton fabric and plastic plaster, and placed into a plastic container field with water. The temperature increase of water caused the decrease in the emission intensity (presented here as a red channel intensity) of each spot, having the same slope but different offset values, originating from different thickness of the samples. These results indicated the wide usable range of Cu_5 cluster thermometers, including various conditions, investigated heat and substrates. Another Cu cluster, the Cu_6-Cu_2-Cu_6 [$Cu_6L_3(Cu_2I_2)Cu_6L_3$] (H_2L = 3,5-bis((3,5-dimethyl-pyrazol-4-yl)methyl)-2,6- dimethylpyridine, Cu_2I_2=(2,6-lutidine)$_2$), is a dual emitting material, being a self-calibrated molecular luminescent thermometer, and it is based on the emission quenching via temperature changes[185]. Emission bands which are influenced by the temperature are attributed to the Cu_2I_2 and Cu_6L_3 clusters, emitting in the blue (λ_{em1}, λ_{exc} = 310–340 nm) and red (λ_{em2}, λ_{exc} = 290 nm) region of the spectrum, respectively. The temperature sensing performance of Cu_6-Cu_2-Cu_6 was investigated in the 100–450 K range and exploiting the emission intensity ratio between λ_{em1}, and λ_{em2}. Linear dependences of the thermometric parameter on temperature are observed from 120 to 260 K (S = 0.208 %/K-0.285 %/K) and in the 240 K-450 K range (S = 0.283 %/K-0.088 %/K), under 310 nm and 340 nm excitations, respectively. Cu nanoclasters have been also used for the temperature sensing in MDA-MB-231 cells with the S_R = 3.18 %/K. However, in this case, the intensity based approach was used, which is of low reliability [186]. Also in the *meta*-organic frameworks group you can find Cu-based luminescent thermometer. As described for $[Cu_4I_4(Pz)_2]_n$ (Pz = [1,4-bis(4-pyridylmethyl)piperazine]) (Fig. 12c), an increase in temperature causes a linear change in the ratio of band intensities, which results in a change in the emission color from pinkish at 10 K to yellow-green at 300 K [180].

5.9. Ruthenium

The luminescence of ruthenium complexes is characterized by large Stokes shifts, strong emissions, and microsecond lifetimes. Consequently, they have many applications in physical and chemical sensing. The first ruthenium-based luminescent thermometer was proposed in 1999 by Liebsch et al.[181]. The authors have found that in Ru(phen) (ruthenium-tris-1,10-phenanthroline), the Ru^{2+} luminescence decay time linearly decreases over the 270–310 K temperature range. To develop thermally sensitive paints, Ru(phen) was incorporated into sol-gels and poly(acrylonitrile) (PAN) materials. The highest relative sensitivity of the lifetime-based thermometer was found to be 1.96 %/K. The authors also demonstrated thermal imaging based on the kinetics of the Ru^{2+} luminescence of the 2D microtiterplates, which are frequently used for bioassays (Fig. 12 d). In fact, this report was the first demonstration of 2D thermal imaging based on the luminescence decay time of a ruthenium-based phosphor. In 2005, Köse et al. reported a temperature and pressure sensor based on the luminescence of the Ru(II) complex in the PAN matrix[187]. In this case, the emission intensity ratio of Ru(Phen) at 525 nm and luminescent dye 5,10,15,20-tetrakis(pentafluorophenyl)porphyrin platinum(II) (PtTFPP) 650 nm were analysed. It was found that in the 280–315 K temperature range, the LIR increased monotonically with temperature and remained almost independent of the applied pressure.

In the following year, a temperature sensor film prepared from a different polymer than PAN was presented. Mills et al. described a sensor based on the complex $Ru(bpy)_3^{2+}$ (ruthenium(II) diamine) encapsulated in a poly(vinyl alcohol) (PVA) matrix [188]. This sensor proved to be completely insensitive to the presence of oxygen, because the PVA polymer had a low oxygen permeability. The authors emphasized that the compounds used for synthesis were water-soluble, making them easier to manufacture as temperature-sensitive films. Excitation was obtained by employing 455 nm visible light, and to determine the temperature, the lifetime was measured using the emission peak observed at approximately 490 nm. A decrease in intensity and shortening of the decay time to reduce the temperature in the range of 298–338 K were presented (intensity change from 500 to 300 [a.u.]).

Borisov et al. considered a very similar sensor: a composite material based on the luminescence of the Ru(II) complex (ruthenium tris-1,10-pehenanthroline) in the PAN matrix to measure the temperature combined with Pd(II) for oxygen detection[189]. The simultaneous measurement of temperature and oxygen was facilitated by the spectral separation of the emission bands. Two bands were observed in the emission spectra: one at approximately 580 nm (excitation: 470 nm) associated with Ru(II), and a second at approximately 670 nm (excitation 525 nm) associated with Pd(II). An additional advantage was that the luminescence decay time of the Ru(II) complex was shorter than the decay time of Pd(II), which also simplified the measurements. The ruthenium emission in this sensor was strongly quenched by temperature and was completely insensitive to the presence of oxygen. The luminescence decay time for the range 275–330 K decreased linearly from 4.2 μs to 2.9 μs (change of 0.0236 μs/K). In 2007, Kocincova et al. presented two fiber-optic sensors for simultaneous measurement of two parameters: pO_2/pH and pO_2/temperature [190]. The use of polymer microbeds enabled the elimination of the effects of undesirable factors and prevented the transfer of energy between dyes. The luminescence decay times of the ruthenium complex revealed a shortening from 2 μs to 1 μs in the temperature range of 273–323 K. In 2008, Baleiz~a et al. reported a dual temperature and oxygen-sensing layer containing Ru(II) complexes (ruthenium tris-1,10-pehenanthrolline = $Ru(phen)_3$) encapsulated in a PAN matrix for temperature measurement and fullerenes for oxygen sensing [191]. The presented results indicated that the Ru(II) luminescence decay times were insensitive to changes in oxygen content (maximum deviation: 0.31 %) but changed monotonically with temperature. Bustamante et al. [192] conducted a large-scale comparison of the rates of change of the thermal luminescence kinetics of Ru^{2+} ion complexes ($[Ru(dpp)_3]^{2+}$, $[Ru(bpy)_3]^{2+}$, $[Ru(phen)_2(4\text{-}Clp)]^{2+}$, $[Ru(phen)_2(4\text{-}OHp)]^{2+}$, $[Ru(bpz)_3]^{2+}$, and $[Ru(phen)_3]^{2+}$), revealing the largest reduction in lifetime for $[Ru(phen)_2(4\text{-}Clp)]^{2+}$. Then, this complex was used for temperature sensing of cell culture-on-a-chop measurements with a temperature resolution of 0.05 K.

6. Conclusions, perspectives and outlook

The above descriptions elucidate the benefits of using phosphor-based TM ions in luminescence thermometry. In contrast to trivalent lanthanide ions, for which TMs have been proposed as alternative luminescence thermometry probes, the spectroscopic properties of TM-doped materials can be significantly modified by changing the material parameters of the host. The high plasticity of TM-doped phosphors is an important advantage as it enables the spectral range of the emission to be tailored according to the application requirements. As can be seen in Fig. 13, the emission spectral ranges of TM-doped luminescent thermometers extend from UV to infrared. An additional advantage

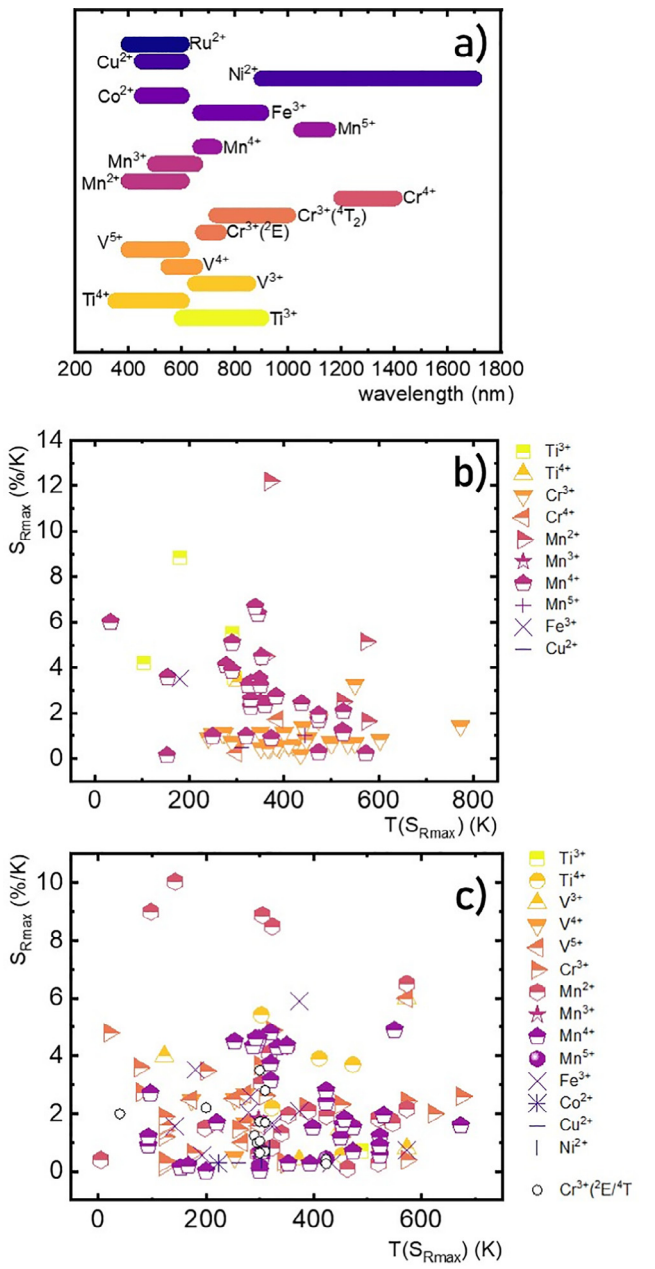

Fig. 13. The comparison of the emission spectral range of particular TM-based luminescent thermometers-a); the S_{Rmax} as a function of the temperature at which it is recorded for lifetime based (Table 3)-b) and ratiometric (Table 4)-c) luminescent thermometers.

of these materials is the prevalence of broad spectral absorption bands, which facilitate luminescence excitation. Moreover, the high absorption cross-sections of TM ions enable intense luminescence to be achieved. Finally, TMs are abundant and much cheaper than lanthanides. However, the low luminescence efficiency observed for most TMs limits the choices of potential dopant ions to chromium and manganese ions.

Fig. 13 summarizes the thermometer performances based on the luminescence intensity ratio, enabling some general conclusions to be drawn. It should be noted that not all papers mentioned herein present the thermometric parameters of the investigated thermometers in the same temperature range and, in some cases, the highest sensitivities were recorded at the boundary temperatures. Nevertheless, the highest sensitivities were recorded for materials doped with Mn^{2+} ions (in some cases exceeding 10 %/K). The highest sensitivities for thermometers based on Mn^{4+} were observed at approximately room temperature, which is particularly important for biological applications. However, in this case, the requirement of UV/blue excitation limits the applicability of these thermometers in biological in vivo studies. At cryogenic temperatures, the highest sensitivities are usually observed for thermometers based on Cr^{3+} ions, with the highest sensitivities observed at temperatures above 200 K. The sensitivities achieved by Cr^{3+}-based thermometers usually do not exceed 5 %/K. At temperatures above 500 K, Cr^{3+}- and Mn^{4+}-based thermometers exhibit the highest sensitivities.

From the perspective of potential applications, not only the temperature range, but also the spectral range of emission plays an important role. When considering thermometers emitting in the UV/blue spectral range, Mn^{2+}-based thermometers exhibit superior thermometric performance. In the green–yellow spectral range, thermometers based on Mn^{2+} and V^{4+} are worth considering, whereas in the red range, materials doped with Cr^{3+} and Mn^{4+} ions are the most important as their emission intensities and sensitivities are the highest. On the other hand, in the NIR range, although materials doped with Ni^{2+} ions offer wide emission ranges, the low emission intensity and low sensitivity of the thermometers described so far in the literature significantly hinder their practical application. Therefore, in this spectral range, thermometers based on Cr^{3+} ion emissions dominate; however, relatively scarcely studied thermometers based on Mn^{5+} ion emissions may constitute suitable alternatives. The Mn^{5+} luminescence is characterized by relatively high quantum efficiency and high luminosity, and its narrow emission bands fall in the second optical transparency window with excitation in the first transparency window. Thus, it is expected that their role and importance in research focusing on biological applications will increase in the near future. A new and interesting research direction taken recently is the doping of thermometers with Fe^{3+} ions, for which very high emission brightness may be observed (e.g. $LiAl_5O_8:Fe^{3+}$).

On the other hand, in the cases of luminescence thermometers based on emission kinetics, thermometers exploiting the shortening of the ^2E level lifetime of Mn^{4+} have the highest sensitivities and, in general, their thermometric parameters provide superior performance. However, their maximum sensitivities decrease with increasing temperature. Several works published in recent years have proven that the luminescence decay of Ti^{3+} ions can provide a super-sensitive thermometric parameter at temperatures below 250 K.

Despite the high sensitivity of Mn^{2+}-based lifetime luminescent thermometers, surprisingly few works devoted to this ion have been reported to date. The great potential of Mn^{2+}-doped materials in lifetime-based luminescence thermometry associated with both high sensitivities and very long lifetimes (often > 10 ms) may suggest that this direction is worthy of extensive research in the future. Considering their very long lifetimes, it can be anticipated that further enhancement of the sensitivities of these thermometers will be possible by activating additional channels of non-radiative depopulation of the Mn^{2+} emitting level, e.g. by co-doped ion guidance.

In summary, luminescence thermometry with TM ions offers a wide range of advantages over other types of thermometer materials, which is a motivation for large-scale research. The potential of these materials is reflected in the rapidly increasing number of papers in recent years on not only new thermometer materials, but also their practical applications in sensing and thermal imaging. Despite the extensive literature on this topic, it can be assumed that the coming years will bring many interesting and scientifically inspiring discoveries in this area.

Declaration of Competing Interest

The authors declare the following financial interests/personal relationships which may be considered as potential competing interests: Lukasz Marciniak reports financial support was provided by Foundation for Polish Science.

Acknowledgements

The „High sensitive thermal imaging for biomedical and micro-electronic application“ project is carried out within the First Team program of the Foundation for Polish Science co-financed by the European Union under the European Regional Development Fund. M. D. Dramićanin acknowledge the support from the Ministry of Education, Science and Technological Development of the Republic of Serbia and the support from the Chinese National Foreign Experts Program for "Belt and Road Initiative“ Innovative Talent Exchange (Grant No. DL2021035001L). The authors thank Dr. Zoran Ristic for his comments and suggestions related to the theoretical part of the paper. K. T. and K. E.P. would like to thank the Foundation for Polish Science (FNP) for its support in the framework of the START 2021 scholarship.

References

[1] M.I. Tiwana, S.J. Redmond, N.H. Lovell, A review of tactile sensing technologies with applications in biomedical engineering, Sensors Actuators, A Phys. 179 (2012) 17–31, https://doi.org/10.1016/j.sna.2012.02.051.
[2] I. Mordor, "Temperature Sensors Market - Growth, Trends, and Forecast (2020 - 2025)," 2019. [Online]. Available: https://www.mordorintelligence.com/industry-reports/temperature-sensors-market-industry.
[3] G. Wasner, J. Schattschneider, K. Heckmann, C. Maier, R. Baron, Vascular abnormalities in reflex sympathetic dystrophy (CRPS I): Mechanisms and diagnostic value, Brain 124 (3) (2001) 587–599, https://doi.org/10.1093/brain/124.3.587.
[4] S. Roujol, M. Ries, B. Quesson, C. Moonen, B. Denis de Senneville, Real-time MR-thermometry and dosimetry for interventional guidance on abdominal organs, Magn. Reson. Med. 63 (4) (2010) 1080–1087, https://doi.org/10.1002/mrm.v63:410.1002/mrm.22309.
[5] W.P. Cheshire, Thermoregulatory disorders and illness related to heat and cold stress, Auton. Neurosci. Basic Clin. 196 (2016) 91–104, https://doi.org/10.1016/j.autneu.2016.01.001.
[6] G. Kastberger, R. Stachl, Infrared imaging technology and biological applications, Behav. Res. Methods Instrum. Comput. 35 (3) (2003) 429–439, https://doi.org/10.3758/BF03195520.
[7] D.D. Soerensen, L.J. Pedersen, Infrared skin temperature measurements for monitoring health in pigs: A review, Acta Vet. Scand. 57 (1) (2015) 5, https://doi.org/10.1186/s13028-015-0094-2.
[8] M. Aldén, A. Omrane, M. Richter, G. Särner, Thermographic phosphors for thermometry: A survey of combustion applications, Prog. Energy Combust. Sci. 37 (4) (2011) 422–461, https://doi.org/10.1016/j.pecs.2010.07.001.
[9] M.M. Kim, A. Giry, M. Mastiani, G.O. Rodrigues, A. Reis, P. Mandin, Microscale thermometry: A review, Microelectron. Eng. 148 (2015) 129–142, https://doi.org/10.1016/j.mee.2015.11.002.
[10] S.W. Allison, G.T. Gillies, Remote thermometry with thermographic phosphors: Instrumentation and applications, Rev. Sci. Instrum. 68 (7) (1997) 2615–2650, https://doi.org/10.1063/1.1148174.
[11] A.H. Khalid, K. Kontis, Thermographic phosphors for high temperature measurements: Principles, current state of the art and recent applications, Sensors 8 (9) (2008) 5673–5744, https://doi.org/10.3390/s8095673.
[12] W.E. Knowles Middleton (Ed.), A History of the Thermometer and Its Uses in Meteorology, vol. 59, no. 2, Johns Hopkins University Press, 1968.
[13] T. Togawa, H. Saito, Non-contact imaging of thermal properties of the skin, Physiol. Meas. 15 (3) (1994) 291–298, https://doi.org/10.1088/0967-3334/15/3/007.
[14] C.D.S. Brites, P.P. Lima, N.J.O. Silva, A. Millán, V.S. Amaral, F. Palacio, L.D. Carlos, Thermometry at the nanoscale, Nanoscale 4 (16) (2012) 4799, https://doi.org/10.1039/c2nr30663h.
[15] E. Carrasco, B. del Rosal, F. Sanz-Rodríguez, Á.J. de la Fuente, P.H. Gonzalez, U. Rocha, K.U. Kumar, C. Jacinto, J.G. Solé, D. Jaque, Intratumoral thermal reading during photo-thermal therapy by multifunctional fluorescent nanoparticles, Adv. Funct. Mater. 25 (4) (2015) 615–626, https://doi.org/10.1002/adfm.v25.410.1002/adfm.201403653.
[16] C. D. S. Brites, A. Millán, and L. D. Carlos, "Chapter 281 - Lanthanides in Luminescent Thermometry," in *Including Actinides*, vol. 49, B. Jean-Claude and P. B. T.-H. on the P. and C. of R. E. Vitalij K., Eds. Elsevier, 2016, pp. 339–427.
[17] M.D. Dramićanin, Trends in luminescence thermometry, J. Appl. Phys. 128 (4) (2020) 40902, https://doi.org/10.1063/5.0014825.
[18] M.D. Dramićanin, Sensing temperature via downshifting emissions of lanthanide-doped metal oxides and salts. A review, Methods Appl. Fluoresc. 4 (4) (2016) 42001, https://doi.org/10.1088/2050-6120/4/4/042001.
[19] A. Bednarkiewicz, J. Drabik, K. Trejgis, D. Jaque, E. Ximendes, L. Marciniak, Luminescence based temperature bio-imaging: Status, challenges, and perspectives, Appl. Phys. Rev. 8 (1) (2021) 11317, https://doi.org/10.1063/5.0030295.
[20] A. Bednarkiewicz, L. Marciniak, L.D. Carlos, D. Jaque, Standardizing luminescence nanothermometry for biomedical applications, Nanoscale 12 (27) (2020) 14405–14421, https://doi.org/10.1039/D0NR03568H.
[21] M. Suta, A. Meijerink, A theoretical framework for ratiometric single ion luminescent thermometers—thermodynamic and kinetic guidelines for optimized performance, Adv. Theory Simul. 3 (12) (2020) 2000176, https://doi.org/10.1002/adts.v3.1210.1002/adts.202000176.
[22] J. Zhou, B. del Rosal, D. Jaque, S. Uchiyama, D. Jin, Advances and challenges for fluorescence nanothermometry, Nat. Methods 17 (10) (2020) 967–980, https://doi.org/10.1038/s41592-020-0957-y.
[23] D. Jaque, F. Vetrone, Luminescence nanothermometry, Nanoscale 4 (15) (2012) 4301–4326, https://doi.org/10.1039/C2NR30764B.
[24] J. Stefanska, L. Marciniak, Single-band ratiometric luminescent thermometry using Pr 3+ ions emitting in yellow and red spectral ranges, Adv. Photonics Res. 2 (7) (2021) 2170021, https://doi.org/10.1002/adpr.202170021.
[25] D. Jaque, C. Jacinto, Luminescent nanoprobes for thermal bio-sensing: Towards controlled photo-thermal therapies, J. Lumin. 169 (2016) 394–399, https://doi.org/10.1016/j.jlumin.2015.03.037.
[26] Q. Wang, M. Liao, Q. Lin, M. Xiong, Z. Mu, F. Wu, A review on fluorescence intensity ratio thermometer based on rare-earth and transition metal ions doped inorganic luminescent materials, J. Alloy. Compd. 850 (2021) 156744, https://doi.org/10.1016/j.jallcom.2020.156744.
[27] M. Back, J. Ueda, M.G. Brik, T. Lesniewski, M. Grinberg, S. Tanabe, Revisiting Cr3+-doped Bi2Ga4O9 spectroscopy: crystal field effect and optical thermometric behavior of near-infrared-emitting singly-activated phosphors, ACS Appl. Mater. Interfaces 10 (48) (2018) 41512–41524, https://doi.org/10.1021/acsami.8b15607.
[28] M. Back, J. Ueda, H. Nambu, M. Fujita, A. Yamamoto, H. Yoshida, H. Tanaka, M. G. Brik, S. Tanabe, Boltzmann thermometry in Cr3+-doped Ga2O3 polymorphs: the structure matters!, Adv Opt. Mater. 9 (9) (2021) 2100033, https://doi.org/10.1002/adom.202100033.
[29] A. Ćirić, Z. Ristić, J. Periša, Ž. Antić, M.D. Dramićanin, MgAl2O4:Cr3+ luminescence thermometry probe in the physiological temperatures range, Ceram. Int. 47 (19) (2021) 27151–27156, https://doi.org/10.1016/j.ceramint.2021.06.131.
[30] A. Ćirić, J. Periša, M. Medić, S. Kuzman, Z. Ristić, Ž. Antić, M.D. Dramićanin, Sensitive temperature reading from intensity ratio of Cr3+ and defects' emissions in MgTiO3:Cr3+, Ceram. Int. 47 (22) (2021) 31915–31919, https://doi.org/10.1016/j.ceramint.2021.08.077.
[31] Z. Ristić, V. Đorđević, M. Medić, S. Kuzman, M. Sekulić, Ž. Antić, M.D. Dramićanin, Triple-temperature readout in luminescence thermometry with Cr3+-doped Mg2SiO4operating from cryogenic to physiologically relevant temperatures, Meas. Sci. Technol. 32 (5) (2021) 054004, https://doi.org/10.1088/1361-6501/abdc9a.
[32] K. Kniec, L. Marciniak, The influence of grain size and vanadium concentration on the spectroscopic properties of YAG:V3+, V5+ and YAG: V, Ln3+ (Ln3+ = Eu3+, Dy3+, Nd3+) nanocrystalline luminescent thermometers, Sensors Actuators B Chem. 264 (2018) 382–390, https://doi.org/10.1016/j.snb.2018.02.189.
[33] L. Marciniak, K. Trejgis, Luminescence lifetime thermometry with Mn3+–Mn4+ co-doped nanocrystals, J. Mater. Chem. C 6 (26) (2018) 7092–7100, https://doi.org/10.1039/C8TC01981A.
[34] H.H. Kung, Review of Spectroscopy of Transition Metal Ions on Surfaces vol. 213, no. 1, Leuven University Press, 2001.
[35] D.S. McClure, Electronic structure of transition-metal complex ions, Radiat. Res. Suppl. 2 (1960) 218, https://doi.org/10.2307/3583598.
[36] M.G. Brik, Ab-initio studies of the electronic and optical properties of Al2O3: Ti3+ laser crystals, Phys. B Condens. Matter 532 (2018) 178–183, https://doi.org/10.1016/j.physb.2017.02.032.
[37] A. B. P. Lever and S. A. Rice, *Inorganic Electronic Spectroscopy* , vol. 22, no. 10. 1969.
[38] D. Plessers et al., Single site spectroscopy of transition metal ions and reactive oxygen complexes in zeolites, Reference Module in Chemistry, Molecular Sciences and Chemical Engineering, Elsevier, 2021.
[39] M. Shi, L. Yao, S. Yu, Y. Dong, Q. Shao, Enhancing the temperature sensitivity of Cr3+emissions by modification of the host's composition for fluorescence thermometry applications, Dalt. Trans. 51 (2) (2022) 587–593, https://doi.org/10.1039/d1dt03480d.
[40] K. Elzbieciak, A. Bednarkiewicz, L. Marciniak, Temperature sensitivity modulation through crystal field engineering in Ga3+ co-doped Gd3Al5-xGaxO12:Cr3+, Nd3+ nanothermometers, Sensors Actuators B Chem. 269 (2018) 96–102, https://doi.org/10.1016/j.snb.2018.04.157.
[41] K. Elzbieciak-Piecka, C. Matuszewska, L. Marciniak, Step by step designing of sensitive luminescent nanothermometers based on Cr3+, Nd3+ co-doped La3−xLuxAl5−yGayO12 nanocrystals, New J. Chem. 43 (32) (2019) 12614–12622, https://doi.org/10.1039/C9NJ03167G.
[42] K. Elzbieciak, L. Marciniak, The Impact of Cr3+ Doping on Temperature Sensitivity Modulation in Cr3+ Doped and Cr3+, Nd3+ Co-doped Y3Al5O12, Y3Al2Ga3O12, and Y3Ga5O12 Nanothermometers, Front. Chem. 6 (2018) 424, https://doi.org/10.3389/fchem.2018.00424.

[43] S. M. Borisov, K. Gatterer, and I. K. Brigitte Bitschnau, "Preparation and characterization of chromium(III)-activated yttrium aluminum borate: A new thermographic phosphor for optical sensing and imaging at ambient temperatures," *J. Phys. Chem. C*, vol. 114, no. 19, pp. 9118–9124, May 2010, doi: 10.1021/jp1016467.
[44] D. Chen, X. Chen, X. Li, H. Guo, S. Liu, X. Li, Cr^3+-doped Bi_2Ga_4O_9-Bi_2Al_4O_9 solid-solution phosphors: crystal-field modulation and lifetime-based temperature sensing, Opt. Lett. 42 (23) (2017) 4950, https://doi.org/10.1364/ol.42.004950.
[45] W. Piotrowski, M. Kuchowicz, M. Dramićanin, L. Marciniak, Lanthanide dopant stabilized Ti3+ state and supersensitive Ti3+ -based multiparametric luminescent thermometer in SrTiO3:Ln3+ (Ln3+ = Lu3+, La3+, Tb3+) nanocrystals, Chem. Eng. J. 428 (2022) 131165, https://doi.org/10.1016/j.cej.2021.131165.
[46] F. Li, J. Cai, F.F. Chi, Y. Chen, C. Duan, M. Yin, Investigation of luminescence from LuAG: Mn4+ for physiological temperature sensing, Opt. Mater. (Amst) 66 (2017) 447–452, https://doi.org/10.1016/j.optmat.2017.02.054.
[47] K. Trejgis, M.D. Dramićanin, L. Marciniak, Highly sensitive multiparametric luminescent thermometer for biologically-relevant temperatures based on Mn4+, Ln3+ co-doped SrTiO3 nanocrystals, J. Alloy. Compd. 875 (2021) 159973, https://doi.org/10.1016/j.jallcom.2021.159973.
[48] M. Back, J. Ueda, J. Xu, D. Murata, M.G. Brik, S. Tanabe, Ratiometric Luminescent Thermometers with a Customized Phase-Transition-Driven Fingerprint in Perovskite Oxides, ACS Appl. Mater. Interfaces 11 (42) (2019) 38937–38945, https://doi.org/10.1021/acsami.9b1301010.1021/acsami.9b13010.s001.
[49] D. Chen, Z. Wan, Y. Zhou, Dual-phase nano-glass-ceramics for optical thermometry, Sensors Actuators, B Chem. 226 (2016) 14–23, https://doi.org/10.1016/j.snb.2015.10.115.
[50] J.I. Eldridge, M.D. Chambers, Fiber optic thermometer using Cr-doped GdAlO3 broadband emission decay, Meas. Sci. Technol. 26 (9) (2015) 95202, https://doi.org/10.1088/0957-0233/26/9/095202.
[51] Z. Wu, L.i. Li, G. Tian, Y. Wang, F. Ling, Z. Cao, S. Jiang, G. Xiang, Y. Li, X. Zhou, High-sensitivity and wide-temperature-range dual-mode optical thermometry under dual-wavelength excitation in a novel double perovskite tellurate oxide, Dalt. Trans. 50 (33) (2021) 11412–11421, https://doi.org/10.1039/D1DT01147B.
[52] L. Dong, L. Zhang, Y. Jia, Y. Xu, S. Yin, H. You, ZnGa2–yAlyO4:Mn2+, Mn4+ Thermochromic Phosphors: Valence State Control and Optical Temperature Sensing, Inorg. Chem. 59 (21) (2020) 15969–15976, https://doi.org/10.1021/acs.inorgchem.0c0247410.1021/acs.inorgchem.0c02474.s001.
[53] W. Piotrowski, K. Trejgis, K. Maciejewska, K. Ledwa, B. Fond, L. Marciniak, Thermochromic Luminescent Nanomaterials Based on Mn4+/Tb3+Codoping for Temperature Imaging with Digital Cameras, ACS Appl. Mater. Interfaces 12 (39) (2020) 44039–44048, https://doi.org/10.1021/acsami.0c1173010.1021/acsami.0c11730.s001.
[54] H. A. Jahn, E. Teller, and F. G. Donnan, "Stability of polyatomic molecules in degenerate electronic states - I—Orbital degeneracy," *Proc. R. Soc. London. Ser. A - Math. Phys. Sci.*, vol. 161, no. 905, pp. 220–235, Jul. 1937, doi: 10.1098/rspa.1937.0142.
[55] J.H. Van Vleck, The John-Teller effect and crystalline stark splitting for clusters of the form XY6, J. Chem. Phys. 7 (1) (1939) 72–84, https://doi.org/10.1063/1.1750327.
[56] Y. Tanabe, S. Sugano, On the Absorption Spectra of Complex Ions. I, J. Phys. Soc. Japan 9 (5) (1954) 753–766, https://doi.org/10.1143/JPSJ.9.753.
[57] R. Hoshino, T. Nakamura, S. Adachi, Synthesis and Photoluminescence Properties of BaSnF 6: Mn 4+ Red Phosphor, ECS J. Solid State Sci. Technol. 5 (3) (2016) R37–R43, https://doi.org/10.1149/2.0151603jss.
[58] G. Blasse, The influence of charge-transfer and rydberg states on the luminescence properties of lanthanides and actinides, in: Spectra and Chemical Interactions, 2007, pp. 43–79, doi: 10.1007/bfb0116577.
[59] C. C. Klick and J. H. Schulman, "Luminescence in Solids," in *Solid State Physics - Advances in Research and Applications*, vol. 5, no. C, F. SEITZ and D. B. T.-S. S. P. TURNBULL, Eds. Academic Press, 1957, pp. 97–172.
[60] L.A. Riseberg, H.W. Moos, Multiphonon orbit-lattice relaxation of excited states of rare-earth ions in crystals, Phys. Rev. 174 (2) (1968) 429–438, https://doi.org/10.1103/PhysRev.174.429.
[61] G. Blasse, On the Eu3+ fluorescence of mixed metal oxides. IV. The photoluminescent efficiency of Eu3+-activated oxides, J. Chem. Phys. 45 (7) (1966) 2356–2360, https://doi.org/10.1063/1.1727946.
[62] T. Katsumata, A. Nakayama, Y. Kano, H. Aizawa, S. Komuro, Characteristics of Ti-doped sapphire for fluorescence thermo-sensor, in: ICCAS 2007 - International Conference on Control, Automation and Systems, 2007, pp. 2331–2334, https://doi.org/10.1109/ICCAS.2007.4406718.
[63] T. Katsumata et al., Development of sensor materials in fluorescence thermometer, in: ICSMA 2008 - International Conference on Smart Manufacturing Application, 2008, pp. 320–323, https://doi.org/10.1109/ICSMA.2008.4505666.
[64] J. Drabik, B. Cichy, L. Marciniak, New type of nanocrystalline luminescent thermometers based on Ti3+/Ti4+ and Ti4+/Ln3+ (Ln3+ = Nd3+, Eu3+, Dy3+) luminescence intensity ratio, J. Phys. Chem. C 122 (26) (2018) 14928–14936, https://doi.org/10.1021/acs.jpcc.8b0232810.1021/acs.jpcc.8b02328.s001.
[65] J. Drabik, L. Marciniak, The influence of Eu3+ concentration on the spectroscopic properties of YAG:Ti, Eu3+ nanocrystalline luminescent thermometer, J. Lumin. 208 (2019) 213–217, https://doi.org/10.1016/j.jlumin.2018.12.054.
[66] C. Wang, Y. Jin, L. Yuan, H. Wu, G. Ju, Z. Li, D. Liu, Y. Lv, L.i. Chen, Y. Hu, A spatial/temporal dual-mode optical thermometry platform based on synergetic luminescence of Ti4+-Eu3+ embedded flexible 3D micro-rod arrays: High-sensitive temperature sensing and multi-dimensional high-level secure anti-counterfeiting, Chem. Eng. J. 374 (2019) 992–1004, https://doi.org/10.1016/j.cej.2019.06.015.
[67] G.-H. Pan, L. Zhang, H. Wu, X. Qu, H. Wu, Z. Hao, L. Zhang, X. Zhang, J. Zhang, On the luminescence of Ti4+ and Eu3+ in monoclinic ZrO2: High performance optical thermometry derived from energy transfer, J. Mater. Chem. C 8 (13) (2020) 4518–4533, https://doi.org/10.1039/C9TC06992E.
[68] W.M. Piotrowski, Z. Ristic, M.D. Dramićanin, Ł. Marciniak, and Marciniak, "Modification of the thermometric performance of the lifetime-based luminescent thermometer exploiting Ti3+ emission in SrTiO3 and CaTiO3 by doping with lanthanide ions", J. Alloy. Compd. 906 (2022) 164398, https://doi.org/10.1016/j.jallcom.2022.164398.
[69] K. Kniec, K. Ledwa, and L. Marciniak, "Enhancing the relative sensitivity of V5+, V4+ and V3+ based luminescent thermometer by the optimization of the stoichiometry of Y3Al5-xGaxO12 nanocrystals," *Nanomaterials*, vol. 9, no. 10. 2019, doi: 10.3390/nano9101375.
[70] K. Kniec, L. Marciniak, Spectroscopic properties of LaGaO3:V, Nd3+ nanocrystals as a potential luminescent thermometer, PCCP 20 (33) (2018) 21598–21606, https://doi.org/10.1039/c8cp04080j.
[71] I.E. Kolesnikov, D.V. Mamonova, M.A. Kurochkin, E.Y. Kolesnikov, E. Lähderanta, Multimode luminescence thermometry based on emission and excitation spectra, J. Lumin. 231 (2021) 117828, https://doi.org/10.1016/j.jlumin.2020.117828.
[72] S.W. Allison, D.L. Beshears, M.R. Cates, M. Paranthaman, G.T. Gilles, LED-induced fluorescence diagnostics for turbine and combustion engine thermometry, in: Optical Diagnostics for Fluids Solids, and Combustion, 2001, p. 28, https://doi.org/10.1117/12.449386.
[73] J. Ueda, M. Back, M.G. Brik, Y. Zhuang, M. Grinberg, S. Tanabe, Ratiometric optical thermometry using deep red luminescence from 4T2 and 2E states of Cr3+ in ZnGa2O4 host, Opt. Mater. (Amst) 85 (2018) 510–516, https://doi.org/10.1016/j.optmat.2018.09.013.
[74] B. Zhu, N. Li, S. Ren, Y. Liu, D. Zhang, Q. Wang, Q. Shi, Q. Wang, S. Li, B. Zhang, W. Wang, C. Liu, Mn2+ ions substitution inducing improvement of optical performances in ZnAl2O4: Cr3+ phosphors: Energy transfer and ratiometric optical thermometry, Spectrochim. Acta - Part A Mol. Biomol. Spectrosc. 264 (2022) 120321, https://doi.org/10.1016/j.saa.2021.120321.
[75] M. Back, J. Ueda, M.G. Brik, S. Tanabe, Pushing the limit of boltzmann distribution in Cr3+-doped CaHfO3for cryogenic thermometry, ACS Appl. Mater. Interfaces 12 (34) (2020) 38325–38332, https://doi.org/10.1021/acsami.0c08965.
[76] Z. Ristić, V. Đorđević, M. Medić, S. Kuzman, M.G. Brik, Ž. Antić, M.D. Dramićanin, Temperature dependence of the Cr3+-DOPED Mg2TiO4 near-infrared emission, Opt. Mater. 120 (2021) 111468, https://doi.org/10.1016/j.optmat.2021.111468.
[77] L. Marciniak, A. Bednarkiewicz, D. Kowalska, W. Strek, A new generation of highly sensitive luminescent thermometers operating in the optical window of biological tissues, J. Mater. Chem. C 4 (24) (2016) 5559–5563, https://doi.org/10.1039/C6TC01484D.
[78] L. Marciniak, A. Bednarkiewicz, Nanocrystalline NIR-to-NIR luminescent thermometer based on Cr3+, Yb3+ emission, Sensors Actuators, B Chem. 243 (2017) 388–393, https://doi.org/10.1016/j.snb.2016.12.006.
[79] L. Marciniak, A. Bednarkiewicz, J. Drabik, K. Trejgis, W. Strek, Optimization of highly sensitive YAG:Cr3+, Nd3+ nanocrystal-based luminescent thermometer operating in an optical window of biological tissues, PCCP 19 (10) (2017) 7343–7351, https://doi.org/10.1039/C6CP07213E.
[80] D. Chen, S. Liu, Y. Zhou, Z. Wan, P. Huang, Z. Ji, Dual-activator luminescence of RE/TM:Y3Al5O12 (RE = Eu3+, Tb3+, Dy3+; TM = Mn4+, Cr3+) phosphors for self-referencing optical thermometry, J. Mater. Chem. C 4 (38) (2016) 9044–9051, https://doi.org/10.1039/c6tc02934e.
[81] Y. Zhu, C. Li, D. Deng, H. Yu, H. Li, L.e. Wang, C. Shen, X. Jing, S. Xu, High-sensitivity based on Eu2+/Cr3+ co-doped BaAl12O19 phosphors for dual-mode optical thermometry, J. Lumin. 237 (2021) 118142, https://doi.org/10.1016/j.jlumin.2021.118142.
[82] J. Periša, Z. Ristić, V. Đorđević, M. Sekulić, T. Dramićanin, Ž. Antić, M.D. Dramićanin, Multiparametric luminescence thermometry from Dy3+, Cr3+ double activated YAG, J. Lumin. 238 (2021) 118306, https://doi.org/10.1016/j.jlumin.2021.118306.
[83] Y. Zhou, L. Li, F. Qin, Z. Zhang, Stably and highly sensitive FIR thermometry over a wide temperature range of 303–753 K based on the GdVO 4: Eu 3+ and Al 2 O 3: Cr 3+ hybrid particles, Opt. Express 28 (10) (2020) 14366, https://doi.org/10.1364/oe.393115.
[84] Y. Zhou, L. Li, F. Qin, Z. Zhang, Highly sensitive fluorescence intensity ratio thermometry by breaking the thermal correlation of two emission centers, Opt. Lett. 44 (18) (2019) 4598, https://doi.org/10.1364/ol.44.004598.
[85] L. Qiu, P. Wang, X. Wei, F. Chi, Y. Chen, M. Yin, Investigation of a phosphor mixture of LiAl5O8: Cr3+ and LuPO4: Tb3+ as a dual-mode temperature sensor with high sensitivity, J. Alloy. Compd. 879 (2021) 160461, https://doi.org/10.1016/j.jallcom.2021.160461.
[86] D. Chen, S. Liu, W. Xu, X. Li, Yb3+/Ln3+/Cr3+ (Ln = Er, Ho) doped transparent glass ceramics: Crystallization, Ln3+ sensitized Cr3+ upconversion emission and multi-modal temperature sensing, J. Mater. Chem. C 5 (45) (2017) 11769–11780, https://doi.org/10.1039/c7tc04410k.

[87] A. Bednarkiewicz, K. Trejgis, J. Drabik, A. Kowalczyk, L. Marciniak, Phosphor-Assisted Temperature Sensing and Imaging Using Resonant and Nonresonant Photoexcitation Scheme, ACS Appl. Mater. Interfaces 9 (49) (2017) 43081–43089, https://doi.org/10.1021/acsami.7b13649.
[88] A. Ćirić, S. Stojadinović, Z. Ristić, Ž. Antić, M.D. Dramićanin, Temperature sensing using ruby coatings created by plasma electrolytic oxidation, Sensors Actuators A Phys. 331 (2021) 112987, https://doi.org/10.1016/j.sna.2021.112987.
[89] V.B. Mykhaylyk, H. Kraus, L.-I. Bulyk, I. Lutsyuk, V. Hreb, L. Vasylechko, Y. Zhydachevskyy, A. Wagner, A. Suchocki, Al2O3co-doped with Cr3+and Mn4+, a dual-emitter probe for multimodal non-contact luminescence thermometry, Dalt. Trans. 50 (41) (2021) 14820–14831, https://doi.org/10.1039/D1DT02836G.
[90] V. Mykhaylyk, H. Kraus, Y. Zhydachevskyy, V. Tsiumra, A. Luchechko, A. Wagner, A. Suchocki, Multimodal non-contact luminescence thermometry with cr-doped oxides, Sensors (Switzerland) 20 (18) (2020) 5259, https://doi.org/10.3390/s20185259.
[91] A. Luchechko, V. Vasyltsiv, Y.a. Zhydachevskyy, M. Kushlyk, S. Ubizskii, A. Suchocki, Luminescence spectroscopy of Cr3+ions in bulk single crystalline β-Ga2O3, J. Phys. D Appl. Phys. 53 (35) (2020) 354001, https://doi.org/10.1088/1361-6463/ab8c7d.
[92] E. Glais et al., Luminescence properties of ZnGa 2 O 4: Cr 3+, Bi 3+ nanophosphors for thermometry applications, RSC Adv. 8 (73) (2018) 41767–41774, https://doi.org/10.1039/c8ra08182d.
[93] K.T.V. Grattan, A.W. Palmer, Z. Zhang, Development of a high-temperature fiber-optic thermometer probe using fluorescent decay, Rev. Sci. Instrum. 62 (5) (1991) 1210–1213, https://doi.org/10.1063/1.1142001.
[94] Z. Zhang, K.T.V. Grattan, A.W. Palmer, Thermal characteristics of alexandrite fluorescence decay at high temperatures, induced by a visible laser diode emission, J. Appl. Phys. 73 (7) (1993) 3493–3498, https://doi.org/10.1063/1.354054.
[95] A. Wadhwa et al., Multi-phase glass-ceramics containing CaF 2: Er 3+ and ZnAl 2 O 4: Cr 3+ nanocrystals for optical temperature sensing, J. Am. Ceram. Soc. 102 (5) (2019) 2472–2481, https://doi.org/10.1111/jace.16098.
[96] D. Chen, Z. Wan, Y. Zhou, X. Zhou, Y. Yu, J. Zhong, M. Ding, Z. Ji, Dual-phase glass ceramic: structure, dual-modal luminescence, and temperature sensing behaviors, ACS Appl. Mater. Interfaces 7 (34) (2015) 19484–19493, https://doi.org/10.1021/acsami.5b06036.
[97] Z. Fang, L. Zhao, Q. Yang, Z.e. Yang, Y. Cai, D. Zhou, X. Yu, J. Qiu, X. Xu, Optical thermometry properties of silicate glass ceramics with dual-phase for spatial isolation of Er3+ and Cr3+, J. Lumin. 219 (2020) 116861, https://doi.org/10.1016/j.jlumin.2019.116861.
[98] K. Elzbieciak-Piecka, J. Drabik, D. Jaque, L. Marciniak, Cr3+based nanocrystalline luminescent thermometers operating in a temporal domain, PCCP 22 (44) (2020) 25949–25962, https://doi.org/10.1039/d0cp03453c.
[99] X. Li, G. Jiang, S. Zhou, X. Wei, Y. Chen, C.K. Duan, M. Yin, Luminescent properties of chromium(III)-doped lithium aluminate for temperature sensing, Sensors Actuators, B Chem. 202 (2014) 1065–1069, https://doi.org/10.1016/j.snb.2014.06.053.
[100] D. Chen, Z. Wan, Y. Zhou, Z. Ji, Cr3+-doped gallium-based transparent bulk glass ceramics for optical temperature sensing, J. Eur. Ceram. Soc. 35 (15) (2015) 4211–4216, https://doi.org/10.1016/j.jeurceramsoc.2015.08.005.
[101] X. Li, Y. Chen, T. Yang, Y. Zhu, Q. Mao, J. Zhong, S. Li, Dual-phase glass ceramics for dual-modal optical thermometry through a spatial isolation strategy, Dalt. Trans. 50 (44) (2021) 16223–16232, https://doi.org/10.1039/D1DT03154F.
[102] D. Chen, Z. Wan, Y. Zhou, Optical spectroscopy of Cr^3+-doped transparent nano-glass ceramics for lifetime-based temperature sensing, Opt. Lett. 40 (15) (2015) 3607, https://doi.org/10.1364/ol.40.003607.
[103] C. Wang, A. Wadhwa, S. Cui, R. Ma, X. Qiao, X. Fan, X. Zhang, Dual mode temperature sensing through luminescence lifetimes of F- and O-coordinated Cr3+ sites in fluorosilicate glass-ceramics, RSC Adv. 7 (83) (2017) 52435–52441, https://doi.org/10.1039/C7RA10864H.
[104] A. Mondal, S. Das, J. Manam, Investigation on spectroscopic properties and temperature dependent photoluminescence of NIR emitting Cr3+ doped zinc gallate long persistent nanophosphor, Phys. B Condens. Matter 569 (2019) 20–30, https://doi.org/10.1016/j.physb.2019.05.030.
[105] F. Venturini, R. Bürgi, S.M. Borisov, I. Klimant, Optical temperature sensing using a new thermographic phosphor, Sensors Actuators, A Phys. 233 (2015) 324–329, https://doi.org/10.1016/j.sna.2015.07.009.
[106] N. Fuhrmann, T. Kissel, A. Dreizler, J. Brübach, Gd3Ga5O12: Cr - A phosphor for two-dimensional thermometry in internal combustion engines, Meas. Sci. Technol. 22 (4) (2011) 45301, https://doi.org/10.1088/0957-0233/22/4/045301.
[107] F. Anghel, C. Iliescu, K.T.V. Grattan, A.W. Palmer, Z.Y. Zhang, Fluorescent-based lifetime measurement thermometer for use at subroom temperatures (200–300 K), Rev. Sci. Instrum. 66 (3) (1995) 2611–2614, https://doi.org/10.1063/1.1145596.
[108] B. Atakan, C. Eckert, C. Pflitsch, Light emitting diode excitation of Cr3+:Al2O 3 as thermographic phosphor: Experiments and measurement strategy, Meas. Sci. Technol. 20 (7) (2009) 75304, https://doi.org/10.1088/0957-0233/20/7/075304.
[109] V.C. Fernicola, L. Rosso, R. Galleano, T. Sun, Z.Y. Zhang, K.T.V. Grattan, Investigations on exponential lifetime measurements for fluorescence thermometry, Rev. Sci. Instrum. 71 (7) (2000) 2938–2943, https://doi.org/10.1063/1.1150714.
[110] V.C. Fernicola, Z.Y. Zhang, K.T.V. Grattan, Fiber optic thermometry based on Cr-fluorescence in olivine crystals, Rev. Sci. Instrum. 68 (6) (1997) 2418–2421, https://doi.org/10.1063/1.1148126.
[111] M. Salem, S. Staude, U. Bergmann, B. Atakan, Heat flux measurements in stagnation point methane/air flames with thermographic phosphors, Exp. Fluids 49 (4) (2010) 797–807, https://doi.org/10.1007/s00348-010-0910-4.
[112] H. Aizawa, M. Sekiguchi, T. Katsumata, S. Komuro, T. Morikawa, Fabrication of ruby phosphor sheet for the fluorescence thermometer application, Rev. Sci. Instrum. 77 (4) (2006) 44902, https://doi.org/10.1063/1.2190069.
[113] C. Pflitsch, D. Viefhaus, B. Atakan, CVD of thin ruby films on Si(100) and stainless steel for surface temperature sensor applications, Chem. Vap. Depos. 13 (8) (2007) 420–426, https://doi.org/10.1002/(ISSN)1521-386210.1002/cvde.v13:810.1002/cvde.200606564.
[114] E. Glais, A. Maître, B. Viana, C. Chanéac, Experimental measurement of local high temperature at the surface of gold nanorods using doped ZnGa2O4as a nanothermometer, Nanoscale Adv. 3 (10) (2021) 2862–2869, https://doi.org/10.1039/d1na00010a.
[115] X. Chen, S. Liu, K. Huang, J. Nie, R.u. Kang, X. Tian, S. Zhang, Y. Li, J. Qiu, Cr4+ activated NIR-NIR multi-mode luminescent nanothermometer for double biological windows, Chem. Eng. J. 396 (2020) 125201, https://doi.org/10.1016/j.cej.2020.125201.
[116] W. Piotrowski, L. Dalipi, R. Szukiewicz, B. Fond, M. Dramicanin, L. Marciniak, The role of Cr3+and Cr4+in emission brightness enhancement and sensitivity improvement of NIR-emitting Nd3+/Er3+ratiometric luminescent thermometers, J. Mater. Chem. C 9 (37) (2021) 12671–12680, https://doi.org/10.1039/d1tc03046a.
[117] M. Back, J. Ueda, J. Xu, K. Asami, M.G. Brik, S. Tanabe, Effective ratiometric luminescent thermal sensor by Cr3+-doped mullite Bi2Al4O9 with robust and reliable performances, Adv. Opt. Mater. 8 (11) (2020) 2000124, https://doi.org/10.1002/adom.202000124.
[118] Z. Zhang, X. Li, C. Wang, X. Qiao, High performance optical temperature sensing via selectively partitioning Cr4+ in the residual SiO2-rich phase of glass-ceramics, PCCP 21 (31) (2019) 17047–17053, https://doi.org/10.1039/c9cp03929e.
[119] Q. Zhou, L. Dolgov, A.M. Srivastava, L. Zhou, Z. Wang, J. Shi, M.D. Dramićanin, M.G. Brik, M. Wu, Mn2+ and Mn4+ red phosphors: Synthesis, luminescence and applications in WLEDs. A review, J. Mater. Chem. C 6 (11) (2018) 2652–2671, https://doi.org/10.1039/C8TC00251G.
[120] S. Wang, S. Westcott, W. Chen, Nanoparticle luminescence thermometry, J. Phys. Chem. B 106 (43) (2002) 11203–11209, https://doi.org/10.1021/jp026445m.
[121] J. Xue et al., Designing ultra-highly efficient Mn2+-activated Zn2GeO4 green-emitting persistent phosphors toward versatile applications, Mater. Today Chem. 23 (2022), https://doi.org/10.1016/j.mtchem.2021.100693 100693.
[122] X. Fan, W. Zhang, F. Lü, Y. Sui, J. Wang, Z. Xu, Research of fluorescent properties of a new type of phosphor with mn2+-doped ca2sio4, Sensors 21 (8) (2021), https://doi.org/10.3390/s21082788.
[123] H. Yao, Y. Zhang, Y. Xu, Dopant concentration-dependent morphological evolution of Zn2GeO4:Mn2+/Eu3+ phosphor and optical temperature sensing performance, J. Alloy. Compd. 770 (2019) 149–157, https://doi.org/10.1016/j.jallcom.2018.08.105.
[124] H. Xia, L. Lei, W. Hong, S. Xu, A novel Ce3+/Mn2+/Eu3+ tri-doped GdF3 nanocrystals for optical temperature sensor and anti-counterfeiting, J. Alloy. Compd. 757 (2018) 239–245, https://doi.org/10.1016/j.jallcom.2018.05.094.
[125] Y. Fu, C. Li, F. Zhang, S. Huang, Z. Wu, Y. Wang, Z. Zhang, Site preference and the optical thermometry strategy by different temperature response from two sites environment of Mn2+ in K7ZnSc2B15O30, Chem. Eng. J. 409 (2021) 128190, https://doi.org/10.1016/j.cej.2020.128190.
[126] J. Song, W. Zhao, H. Zhang, Y. Liu, H. Huang, H. Yang, H. Zhang, J. Zhong, Energy transfer and ratiometric Temperature sensing based on the dual-emitting NaMgBO3:Ce3+, Mn2+ phosphor, J. Lumin. 232 (2021) 117858, https://doi.org/10.1016/j.jlumin.2020.117858.
[127] Y. Gao, Y. Cheng, F. Huang, H. Lin, J. Xu, Y. Wang, Sn2+/Mn2+ codoped strontium phosphate (Sr2P2O7) phosphor for high temperature optical thermometry, J. Alloy. Compd. 735 (2018) 1546–1552, https://doi.org/10.1016/j.jallcom.2017.11.243.
[128] X. Zhang, J. Xu, Z. Guo, M. Gong, Luminescence and energy transfer of dual-emitting solid solution phosphors (Ca, Sr)10Li(PO4)7:Ce3+, Mn2+ for ratiometric temperature sensing, Ind. Eng. Chem. Res. 56 (4) (2017) 890–898, https://doi.org/10.1021/acs.iecr.6b03748.
[129] V. Lojpur, M.G. Nikolić, D. Jovanović, M. Medić, Ž. Antić, M.D. Dramićanin, Luminescence thermometry with Zn2SiO4:Mn2 powder, Appl. Phys. Lett. 103 (14) (2013) 141912, https://doi.org/10.1063/1.4824208.
[130] X. Jiang, S. Xia, J. Zhang, D. Ju, Y. Liu, X. Hu, L. Wang, Z. Chen, X. Tao, Exploring organic metal halides with reversible temperature-responsive dual-emissive photoluminescence, ChemSusChem 12 (24) (2019) 5228–5232, https://doi.org/10.1002/cssc.v12.2410.1002/cssc.201902481.
[131] Y. Zhu, C. Li, D. Deng, B. Chen, H. Yu, H. Li, L.e. Wang, C. Shen, X. Jing, S. Xu, A high-sensitivity dual-mode optical thermometry based on one-step synthesis of Mn2+:BaAl12O19–Mn4+:SrAl12O19 solid solution phosphors, J. Alloy. Compd. 853 (2021) 157262, https://doi.org/10.1016/j.jallcom.2020.157262.
[132] Z.-H. Zuo, S.-L. Jiang, Z.-H. Zhang, J. Liang, J. Li, Z.-Q. Liu, Y. Chen, Compensation effect of electron traps for enhanced fluorescence intensity ratio thermometry performance, Inorg. Chem. Front. 9 (8) (2022) 1802–1811, https://doi.org/10.1039/D2QI00284A.

[133] D. Huang, Q. Ouyang, B. Liu, B. Chen, Y. Wang, C. Yuan, H. Xiao, H. Lian, J. Lin, Mn2+/Mn4+co-doped LaM1−xAl11−yO19(M = Mg, Zn) luminescent materials: electronic structure, energy transfer and optical thermometric properties, Dalt. Trans. 50 (13) (2021) 4651–4662, https://doi.org/10.1039/D1DT00153A.
[134] X. Zhang, Z. Zhu, Z. Guo, Z. Sun, Y. Chen, A ratiometric optical thermometer with high sensitivity and superior signal discriminability based on Na3Sc2P3O12: Eu2+, Mn2+ thermochromic phosphor, Chem. Eng. J. 356 (2019) 413–422, https://doi.org/10.1016/j.cej.2018.09.075.
[135] V. Sharma, M.S. Mehata, A parallel investigation of un-doped and manganese ion-doped zinc selenide quantum dots at cryogenic temperature and application as an optical temperature sensor, Mater. Chem. Phys. 276 (2022) 125349, https://doi.org/10.1016/j.matchemphys.2021.125349.
[136] Y. Gong, Y. Liang, S. Liu, H. Li, Y. Bi, Q. Wang, Y.i. Dou, Improving the temperature-dependent sensitivity of Ca9Y(PO4)7:Ce3+, Mn2+and g-C3N4composite phosphors by mechanical mixing, Inorg. Chem. Front. 8 (15) (2021) 3760–3766, https://doi.org/10.1039/D1QI00588J.
[137] X. Li, Y. Yu, X. Guan, P. Luo, F. Chen, M. Yu, L. Jiang, Dual-emitting Tm3+/Mn2+ co-doped glass ceramic for wide-range optical thermometer, J. Alloy. Compd. 836 (2020) 155507, https://doi.org/10.1016/j.jallcom.2020.155507.
[138] F. Huang, D. Chen, Synthesis of Mn2+:Zn2SiO4–Eu3+:Gd2O3 nanocomposites for highly sensitive optical thermometry through the synergistic luminescence from lanthanide-transition metal ions, J. Mater. Chem. C 5 (21) (2017) 5176–5182, https://doi.org/10.1039/C7TC01500C.
[139] K. Trejgis, L. Marciniak, The influence of manganese concentration on the sensitivity of bandshape and lifetime luminescent thermometers based on Y3Al5O12:Mn3+, Mn4+, Nd3+ nanocrystals, PCCP 20 (14) (2018) 9574–9581, https://doi.org/10.1039/c8cp00558c.
[140] Y. Wang, D. Włodarczyk, M.G. Brik, J. Barzowska, A.N. Shekhovtsov, K.N. Belikov, W. Paszkowicz, L.i. Li, X. Zhou, A. Suchocki, Effect of temperature and high pressure on luminescence properties of mn3+ ions in ca3ga2ge3o12 single crystals, J. Phys. Chem. C 125 (9) (2021) 5146–5157, https://doi.org/10.1021/acs.jpcc.0c0984510.1021/acs.jpcc.0c09845.s001.
[141] F. Jahanbazi, X. Wang, Y. Mao, Tb3+, Mn3+ co-doped La2Zr2O7 nanoparticles for self-referencing optical thermometry, J. Lumin. 240 (2021) 118412, https://doi.org/10.1016/j.jlumin.2021.118412.
[142] Y.K. Xu, S. Adachi, Properties of Na2 SiF6: Mn4+ and Na GeF6: Mn4+ red phosphors synthesized by wet chemical etching, J. Appl. Phys. 105 (1) (2009) 13525, https://doi.org/10.1063/1.3056375.
[143] M.G. Brik, N.M. Avram, Microscopic analysis of the crystal field strength and electron-vibrational interaction in cubic SrTiO3 doped with Cr3+, Mn 4+ and Fe5+ ions, J. Phys.: Condens. Matter 21 (15) (2009) 155502, https://doi.org/10.1088/0953-8984/21/15/155502.
[144] P. Cai, L. Qin, C. Chen, J. Wang, S. Bi, S.I. Kim, Y. Huang, H.J. Seo, Optical thermometry based on vibration sidebands in Y2MgTiO6:Mn4+ double perovskite, Inorg. Chem. 57 (6) (2018) 3073–3081, https://doi.org/10.1021/acs.inorgchem.7b02938.
[145] Z. Yang, Z. Wang, M. Zheng, X. Wang, J. Cui, Y. Yao, L. Cao, M. Zhang, H. Suo, P. Li, Excitation selective thermal characteristics of Mg28Ge7.55−xGaxO32F15.04: Mn4+ and application in single/dual-mode optical thermometry, Mater. Today Commun. 28 (2021) 102660, https://doi.org/10.1016/j.mtcomm.2021.102660.
[146] S.H. Yang, Y.C. Lee, Y.C. Hung, Thermometry of red nanoflaked SrAl12O19: Mn4+ synthesized with boric acid flux, Ceram. Int. 44 (10) (2018) 11665–11673, https://doi.org/10.1016/j.ceramint.2018.03.242.
[147] P. Cai, L. Qin, C. Chen, J. Wang, H.J. Seo, Luminescence, energy transfer and optical thermometry of a novel narrow red emitting phosphor: Cs2WO2F4: Mn4+, Dalt. Trans. 46 (41) (2017) 14331–14340, https://doi.org/10.1039/c7dt02751f.
[148] P. Cai, X. Wang, H.J. Seo, Excitation power dependent optical temperature behaviors in Mn4+ doped oxyfluoride Na2WO2F4, PCCP 20 (3) (2018) 2028–2035, https://doi.org/10.1039/c7cp07123j.
[149] N. Fuhrmann, J. Brübach, A. Dreizler, Phosphor thermometry: A comparison of the luminescence lifetime and the intensity ratio approach, Proc. Combust. Inst. 34 (2) (2013) 3611–3618, https://doi.org/10.1016/j.proci.2012.06.084.
[150] S. Liang, G. Li, P. Dang, Y.i. Wei, H. Lian, J. Lin, Cation substitution induced adjustment on lattice structure and photoluminescence properties of Mg14Ge5O24:Mn4+: optimized emission for w-LED and thermometry applications, Adv. Opt. Mater. 7 (12) (2019) 1900093, https://doi.org/10.1002/adom.201900093.
[151] B. Yan, Y. Wei, W. Wang, M. Fu, G. Li, Red-tunable LuAG garnet phosphors: Via Eu3+ → Mn4+energy transfer for optical thermometry sensor application, Inorg. Chem. Front. 8 (3) (2021) 746–757, https://doi.org/10.1039/d0qi01285h.
[152] Y. Song, N. Guo, J. Li, R. Ouyang, Y. Miao, B. Shao, Photoluminescence and temperature sensing of lanthanide Eu3+ and transition metal Mn4+ dual-doped antimoniate phosphor through site-beneficial occupation, Ceram. Int. 46 (14) (2020) 22164–22170, https://doi.org/10.1016/j.ceramint.2020.05.293.
[153] H. Luo, X. Li, X. Wang, M. Peng, Highly thermal-sensitive robust LaTiSbO6: Mn4+ with a single-band emission and its topological architecture for single/dual-mode optical thermometry, Chem. Eng. J. 384 (2020) 123272, https://doi.org/10.1016/j.cej.2019.123272.
[154] Y. Chen, J. He, X. Zhang, M. Rong, Z. Xia, J. Wang, Z.-Q. Liu, Dual-Mode Optical Thermometry Design in Lu3Al5O12:Ce3+/Mn4+ Phosphor, Inorg. Chem. 59 (2) (2020) 1383–1392, https://doi.org/10.1021/acs.inorgchem.9b03107.
[155] C. Xie, L.u. Zhao, B. Jiang, J. Mao, Y. Lin, P. Wang, X. Wei, M. Yin, Y. Chen, Dual-activator luminescence of LuAG:Mn4+/Tb3+ phosphor for optical thermometry, J. Am. Ceram. Soc. 102 (12) (2019) 7500–7508, https://doi.org/10.1111/jace:v102.1210.1111/jace:16683.
[156] J. Periša, V. Đorđević, Z. Ristić, M. Medić, S. Kuzman, Ž. Antić, M.D. Dramićanin, Highly sensitive temperature reading from intensity ratio of Eu3+ And Mn4+emissions in Y3Al5O12 nanocrystals, Mater. Res. Bull. 149 (2022) 111708, https://doi.org/10.1016/j.materresbull.2021.111708.
[157] Z. Li, X. Yu, T. Wang, S. Wang, L. Guo, Z. Cui, G. Yan, W. Feng, F. Zhao, J. Chen, X. Xu, J. Qiu, Highly sensitive optical thermometer of Sm3+, Mn4+ activated LaGaO3 phosphor for the regulated thermal behavior, J. Am. Ceram. Soc. 105 (4) (2022) 2804–2812, https://doi.org/10.1111/jace:v105.410.1111/jace:18286.
[158] Y.u. Ding, N. Guo, X. Lü, H. Zhou, L.u. Wang, R. Ouyang, Y. Miao, B. Shao, None-rare-earth activated Ca14Al10Zn6O35:Bi3+, Mn4+ phosphor involving dual luminescent centers for temperature sensing, J. Am. Ceram. Soc. 102 (12) (2019) 7436–7447, https://doi.org/10.1111/jace:16660.
[159] M. Zhang, M. Jia, T. Sheng, Z. Fu, Multifunctional optical thermometry based on the transition metal ions doped down-conversion Gd2ZnTiO6: Bi3+, Mn4+ phosphors, J. Lumin. 229 (2021) 117653, https://doi.org/10.1016/j.jlumin.2020.117653.
[160] W.M. Piotrowski, K. Trejgis, M. Dramicanin, L. Marciniak, Strong sensitivity enhancement in lifetime-based luminescence thermometry by co-doping of SrTiO3:Mn4+nanocrystals with trivalent lanthanide ions, J. Mater. Chem. C 9 (32) (2021) 10309–10316, https://doi.org/10.1039/d1tc02814f.
[161] M. Sekulić, Z. Ristić, B. Milićević, Ž. Antić, V. Đorđević, M.D. Dramićanin, Li1.8Na0.2TiO3:Mn4+: The highly sensitive probe for the low-temperature lifetime-based luminescence thermometry, Opt. Commun. 452 (2019) 342–346, https://doi.org/10.1016/j.optcom.2019.07.056.
[162] M.D. Dramićanin, B. Milićević, V. Đorđević, Z. Ristić, J. Zhou, D. Milivojević, J. Papan, M.G. Brik, C.-G. Ma, A.M. Srivastava, M. Wu, Li2TiO3:Mn4+ deep-red phosphor for the lifetime-based luminescence thermometry, ChemistrySelect 4 (24) (2019) 7067–7075, https://doi.org/10.1002/slct.201901590.
[163] T. Cai, Y. Park, S. Mohammadshahi, K.C. Kim, Rise time-based phosphor thermometry using Mg4FGeO6:Mn4+, Meas. Sci. Technol. 32 (1) (2021) 15201, https://doi.org/10.1088/1361-6501/abac8a.
[164] F. Venturini, M. Baumgartner, S.M. Borisov, Mn4+-Doped magnesium titanate-a promising phosphor for self-referenced optical temperature sensing, Sensors (Switzerland) 18 (2) (2018) 668, https://doi.org/10.3390/s18020668.
[165] T. Kissel, E. Baum, A. Dreizler, J. Brübach, Two-dimensional thermographic phosphor thermometry using a CMOS high speed camera system, Appl. Phys. B: Lasers Opt. 96 (4) (2009) 731–734, https://doi.org/10.1007/s00340-009-3626-5.
[166] J. Zhang, X. Hou, S. Wang, Z. Ye, Unraveling the valence states of manganese ions and the effects of composition variation and post-processing in YGG1-x-LuGGx: Mn garnet optical sensor, Chem. Eng. J. 411 (2021), https://doi.org/10.1016/j.cej.2021.128448 128448.
[167] Y. Lin, L.u. Zhao, B. Jiang, J. Mao, F. Chi, P. Wang, C. Xie, X. Wei, Y. Chen, M. Yin, Temperature-dependent luminescence of BaLaMgNbO6:Mn4+, Dy3+ phosphor for dual-mode optical thermometry, Opt. Mater. 95 (2019) 109199, https://doi.org/10.1016/j.optmat.2019.109199.
[168] M. Medić, Z. Ristić, S. Kuzman, V. Đorđević, I. Vukoje, M.G. Brik, M.D. Dramićanin, Luminescence of Mn4+ activated Li4Ti5O12, J. Lumin. 228 (2020) 117646, https://doi.org/10.1016/j.jlumin.2020.117646.
[169] M. Sekulić, V. Đorđević, Z. Ristić, M. Medić, M.D. Dramićanin, Highly sensitive dual self-referencing temperature readout from the Mn4+/Ho3+ binary luminescence thermometry probe, Adv. Opt. Mater. 6 (17) (2018) 1800552, https://doi.org/10.1002/adom.201800552.
[170] C. Xie, P. Wang, Y. Lin, X. Wei, M. Yin, Y. Chen, Temperature-dependent luminescence of a phosphor mixture of Li2TiO3: Mn4+ and Y2O3: Dy3+ for dual-mode optical thermometry, J. Alloy. Compd. 821 (2020) 153467, https://doi.org/10.1016/j.jallcom.2019.153467.
[171] E. Glais, V. Dordević, J. Papan, B. Viana, M.D. Dramićanin, MgTiO3:Mn4+ a multi-reading temperature nanoprobe, RSC Adv. 8 (33) (2018) 18341–18346, https://doi.org/10.1039/c8ra02482k.
[172] P.M. Gschwend, D. Niedbalka, L.R.H. Gerken, I.K. Herrmann, S.E. Pratsinis, Simultaneous Nanothermometry and Deep-Tissue Imaging, Adv. Sci. 7 (12) (2020) 2000370, https://doi.org/10.1002/advs.v7.1210.1002/advs.202000370.
[173] Z. Ristić, W. Piotrowski, M. Medić, J. Periša, Ž.M. Antić, L. Marciniak, M.D. Dramićanin, Near-Infrared luminescent lifetime-based thermometry with Mn5+-activated Sr3(PO4)2and Ba3(PO4)2phosphors, ACS Appl. Electron. Mater. 4 (3) (2022) 1057–1062, https://doi.org/10.1021/acsaelm.1c01207.
[174] K. Kniec, W. Piotrowski, K. Ledwa, M. Suta, L.D. Carlos, L. Marciniak, From quencher to potent activator – Multimodal luminescence thermometry with Fe3+ in the oxides MAl4O7 (M = Ca, Sr, Ba), J. Mater. Chem. C 9 (19) (2021) 6268–6276, https://doi.org/10.1039/D1TC01272J.
[175] K. Kniec, W. Piotrowski, K. Ledwa, L.D. Carlos, L. Marciniak, Spectral and thermometric properties altering through crystal field strength modification and host material composition in luminescence thermometers based on Fe3+doped AB2O4type nanocrystals (A = Mg, Ca; B = Al, Ga), J. Mater. Chem. C 9 (2) (2021) 517–527, https://doi.org/10.1039/d0tc04917d.
[176] K. Kniec, K. Ledwa, K. Maclejewska, L. Marciniak, Intentional modification of the optical spectral response and relative sensitivity of luminescent thermometers based on Fe3+, Cr3+, Nd3+co-doped garnet nanocrystals by

crystal field strength optimization, Mater. Chem. Front. 4 (6) (2020) 1697–1705, https://doi.org/10.1039/d0qm00097c.
[177] K. Kniec, M. Tikhomirov, B. Pozniak, K. Ledwa, L. Marciniak, LiAl5O8:Fe3+ and LiAl5O8:Fe3+, Nd3+ as a New Luminescent Nanothermometer Operating in 1st Biological Optical Window, Nanomaterials 10 (2) (2020), https://doi.org/10.3390/nano10020189.
[178] A. Kobylinska, K. Kniec, K. Maciejewska, L. Marciniak, The influence of dopant concentration and grain size on the ability for temperature sensing using nanocrystalline MgAl2O4:Co2+, Nd3+ luminescent thermometers, New J. Chem. 43 (15) (2019) 6080–6086, https://doi.org/10.1039/C9NJ00368A.
[179] C. Matuszewska, L. Marciniak, The influence of host material on NIR II and NIR III emitting Ni2+-based luminescent thermometers in ATiO3: Ni2+ (A = Sr, Ca, Mg, Ba) nanocrystals, J. Lumin. 223 (2020) 117221, https://doi.org/10.1016/j.jlumin.2020.117221.
[180] Z. Wang, S. Yu, H. Zhang, H. Duan, Thermochromic luminescence and dielectric response of copper(I) iodide based MOFs as luminescent thermometer, Synth. Met. 255 (2019) 116104, https://doi.org/10.1016/j.synthmet.2019.116104.
[181] G. Liebsch, I. Klimant, O.S. Wolfbeis, Luminescence lifetime temperature sensing based on sol-gels and poly(acrylonitrile)s dyed with ruthenium metal-ligand complexes, Adv. Mater. 11 (15) (1999) 1296–1299, https://doi.org/10.1002/(SICI)1521-4095(199910)11:15<1296::AID-ADMA1296>3.0.CO;2-B.
[182] C. Matuszewska, K. Elzbieciak-Piecka, L. Marciniak, Transition metal ion-based nanocrystalline luminescent thermometry in SrTiO3:Ni2+, Er3+ nanocrystals operating in the second optical window of biological tissues, J. Phys. Chem. C 123 (30) (2019) 18646–18653, https://doi.org/10.1021/acs.jpcc.9b04002.10.1021/acs.jpcc.9b04002.s001.
[183] N. Fujino, M. Ichikawa, T. Koyama, Y. Taniguchi, A molecular thermometer based on luminescence of copper(II) tetraphenylporphyrin, Thin Solid Films 518 (2) (2009) 563–566, https://doi.org/10.1016/j.tsf.2009.07.034.
[184] D. Cauzzi, R. Pattacini, M. Delferro, F. Dini, C. Di Natale, R. Paolesse, S. Bonacchi, M. Montalti, N. Zaccheroni, M. Calvaresi, F. Zerbetto, L. Prodi, Temperature-dependent fluorescence of Cu 5 metal clusters: A molecular thermometer, Angew. Chemie - Int. Ed. 51 (38) (2012) 9662–9665, https://doi.org/10.1002/anie.201204052.
[185] J.H. Wang, M. Li, J. Zheng, X.C. Huang, D. Li, A dual-emitting Cu6–Cu2–Cu6 cluster as a self-calibrated, wide-range luminescent molecular thermometer, Chem. Commun. 50 (65) (2014) 9115–9118, https://doi.org/10.1039/c4cc04100c.
[186] J. Ye, X. Dong, H. Jiang, X. Wang, An intracellular temperature nanoprobe based on biosynthesized fluorescent copper nanoclusters, J. Mater. Chem. B 5 (4) (2017) 691–696, https://doi.org/10.1039/c6tb02751b.
[187] M.E. Köse, B.F. Carroll, K.S. Schanze, Preparation and spectroscopic properties of multiluminophore luminescent oxygen and temperature sensor films, Langmuir 21 (20) (2005) 9121–9129, https://doi.org/10.1021/la050997p.
[188] A. Mills, C. Tommons, R.T. Bailey, M.C. Tedford, P.J. Crilly, Luminescence temperature sensing using poly(vinyl alcohol)-encapsulated Ru(bpy)32+ films, Analyst 131 (4) (2006) 495–500, https://doi.org/10.1039/b516366h.
[189] S.M. Borisov, A.S. Vasylevska, C.h. Krause, O.S. Wolfbeis, Composite luminescent material for dual sensing of oxygen and temperature, Adv. Funct. Mater. 16 (12) (2006) 1536–1542, https://doi.org/10.1002/(ISSN)1616-302810.1002/adfm.v16:1210.1002/adfm.200500778.
[190] A.S. Kocincova, S.M. Borisov, C. Krause, O.S. Wolfbeis, Fiber-optic microsensors for simultaneous sensing of oxygen and pH, and of oxygen and temperature, Anal. Chem. 79 (22) (2007) 8486–8493, https://doi.org/10.1021/ac070514h.
[191] C. Baleiz~a, S. Nagl, M. Schäferling, M. N. Berberan-Santos, and O. S. Wolfbeis, "Dual fluorescence sensor for trace oxygen and temperature with unmatched range and sensitivity," *Anal. Chem.*, vol. 80, no. 16, pp. 6449–6457, Aug. 2008, doi: 10.1021/ac801034p.
[192] N. Bustamante, G. Ielasi, M. Bedoya, and G. Orellana, "Optimization of temperature sensing with polymer-embedded luminescent Ru(II) complexes," *Polymers*, vol. 10, no. 3. 2018, doi: 10.3390/polym10030234.
[193] T. Sun, Z.Y. Zhang, K.T.V. Grattan, A.W. Palmer, S.F. Collins, Analysis of the double exponential behavior in alexandrite for optical temperature sensing applications, Rev. Sci. Instrum. 68 (9) (1997) 3442–3446, https://doi.org/10.1063/1.1148306.
[194] Z. Cai, S. Kang, X. Huang, X. Song, X. Xiao, J. Qiu, G. Dong, A novel wide temperature range and multi-mode optical thermometer based on bi-functional nanocrystal-doped glass ceramics, J. Mater. Chem. C 6 (37) (2018) 9932–9940, https://doi.org/10.1039/C8TC03642J.
[195] H.C. Seat, J.H. Sharp, Dedicated temperature sensing with C-axis oriented single-crystal ruby (Cr3+:Al2O3) fibers: Temperature and strain dependences of R-line fluorescence, IEEE Trans. Instrum. Meas. 53 (1) (2004) 140–154, https://doi.org/10.1109/TIM.2003.822010.
[196] S. K. Sharma, E. Glais, M. Pellerin, C. Chaneac, and B. Viana, " Temperature sensing using a Cr:ZnGa 2 O 4 new phosphor ," in *Oxide-based Materials and Devices VII*, Feb. 2016, vol. 9749, p. 974922, doi: 10.1117/12.2219990.
[197] Y. Shen, L. Tong, Y. Wang, L. Ye, Sapphire-fiber thermometer ranging from 20 to 1800 °C, Appl. Opt. 38 (7) (1999) 1139, https://doi.org/10.1364/ao.38.001139.
[198] A. Mondal, J. Manam, Structural, optical and temperature dependent photoluminescence properties of Cr3+-activated LaGaO3 persistent phosphor for optical thermometry, Ceram. Int. 46 (15) (2020) 23972–23984, https://doi.org/10.1016/j.ceramint.2020.06.174.
[199] J.I. Eldridge, Single fiber temperature probe configuration using anti-Stokes luminescence from Cr:GdAlO3, Meas. Sci. Technol. 29 (6) (2018) 65206, https://doi.org/10.1088/1361-6501/aaba21.
[200] A. Wadhwa et al., Selective enrichment of Ln3+ (Ln = Yb; Er) and Cr3+ into SrF2 and ZnAl2O4 nanocrystals precipitated in fluorosilicate glass-ceramics: A dual mode optical temperature sensing study, J. Non. Cryst. Solids 552 (2021), https://doi.org/10.1016/j.jnoncrysol.2020.120395 120395.
[201] Y. Lv, Y. Jin, H. Wu, D. Liu, G. Xiong, G. Ju, L.i. Chen, Y. Hu, An All-Optical Ratiometric Thermometer Based on Reverse Thermal Response from Interplay among Diverse Emission Centers and Traps with High-Temperature Sensitivity, Ind. Eng. Chem. Res. 58 (47) (2019) 21242–21251, https://doi.org/10.1021/acs.iecr.9b0528610.1021/acs.iecr.9b05286.s001.
[202] S. Lv, B. Shanmugavelu, Y. Wang, Q. Mao, Y. Zhao, Y. Yu, J. Hao, Q. Zhang, J. Qiu, S. Zhou, Transition metal doped smart glass with pressure and temperature sensitive luminescence, Adv. Opt. Mater. 6 (21) (2018) 1800881, https://doi.org/10.1002/adom.201800881.
[203] F. Chi, B. Jiang, Z. Zhao, Y. Chen, X. Wei, C. Duan, M. Yin, W.u. Xu, Multimodal temperature sensing using Zn2GeO4:Mn2+ phosphor as highly sensitive luminescent thermometer, Sensors Actuators B Chem. 296 (2019) 126640, https://doi.org/10.1016/j.snb.2019.126640.
[204] J. Liao, M. Wang, L. Kong, J. Chen, X. Wang, H. Yan, J. Huang, C. Tu, Dual-mode optical temperature sensing behavior of double-perovskite CaGdMgSbO6: Mn4+/Sm3+ phosphors, J. Lumin. 226 (2020) 117492, https://doi.org/10.1016/j.jlumin.2020.117492.
[205] D. Chen, W. Xu, S. Yuan, X. Li, J. Zhong, Ln3+-Sensitized Mn4+near-infrared upconverting luminescence and dual-modal temperature sensing, J. Mater. Chem. C 5 (37) (2017) 9619–9628, https://doi.org/10.1039/c7tc02182h.
[206] G. Li, Y.u. Xue, Q. Mao, L. Pei, H. He, M. Liu, L. Chu, J. Zhong, Synergistic luminescent thermometer using co-doped Ca2GdSbO6:Mn4+/(Eu3+ or Sm3+) phosphors, Dalt. Trans. 51 (12) (2022) 4685–4694, https://doi.org/10.1039/D2DT00005A.
[207] G. Li, G. Li, Q. Mao, L. Pei, H. Yu, M. Liu, L. Chu, J. Zhong, Efficient luminescence lifetime thermometry with enhanced Mn4+-activated BaLaCa1−xMgxSbO6 red phosphors, Chem. Eng. J. 430 (2022) 132923, https://doi.org/10.1016/j.cej.2021.132923.
[208] L.i. Li, G. Tian, Y. Deng, Y. Wang, Z. Cao, F. Ling, Y. Li, S. Jiang, G. Xiang, X. Zhou, Constructing ultra-sensitive dual-mode optical thermometers: Utilizing FIR of Mn 4+ /Eu 3+ and lifetime of Mn 4+ based on double perovskite tellurite phosphor, Opt. Express 28 (22) (2020) 33747, https://doi.org/10.1364/OE.409242.
[209] Y.u. Ding, N. Guo, M. Zhu, W. Lv, R. Ouyang, B. Shao, Photoluminescence and ratiometric fluorescence temperature sensing abilities of zincate phosphors, J. Lumin. 228 (2020) 117600, https://doi.org/10.1016/j.jlumin.2020.117600.
[210] K. Kniec, K. Ledwa, L. Marciniak, Enhancing the relative sensitivity of V5+, V4+ and V3+ based luminescent thermometer by the optimization of the stoichiometry of Y3Al5-xGaxO12 nanocrystals, Nanomaterials 9 (10) (2019) 1375, https://doi.org/10.3390/nano9101375.
[211] D. Chen, S. Liu, Z. Wan, Z. Ji, EuF3/Ga2O3 dual-phase nanostructural glass ceramics with Eu2+/Cr3+ dual-activator luminescence for self-calibrated optical thermometry, J. Phys. Chem. C 120 (38) (2016) 21858–21865, https://doi.org/10.1021/acs.jpcc.6b08271.
[212] D. Chen, Z. Wan, S. Liu, Highly sensitive dual-phase nanoglass-ceramics self-calibrated optical thermometer, Anal. Chem. 88 (7) (2016) 4099–4106, https://doi.org/10.1021/acs.analchem.6b00434.
[213] K. Maciejewska, L. Marciniak, Multimodal Stokes and Anti-Stokes luminescent thermometers based on GdP5O14 co-doped with Cr3+ and Nd3+ ions, Chem. Eng. J. 402 (2020) 126197, https://doi.org/10.1016/j.cej.2020.126197.
[214] M. Back, E. Trave, J. Ueda, S. Tanabe, Ratiometric optical thermometer based on dual near-infrared emission in Cr3+-doped bismuth-based gallate host, Chem. Mater. 28 (22) (2016) 8347–8356, https://doi.org/10.1021/acs.chemmater.6b03625.
[215] Q. Wang, Z. Liang, J. Luo, Y. Yang, Z. Mu, X. Zhang, H. Dong, F. Wu, Ratiometric optical thermometer with high sensitivity based on dual far-red emission of Cr3+ in Sr2MgAl22O36, Ceram. Int. 46 (4) (2020) 5008–5014, https://doi.org/10.1016/j.ceramint.2019.10.241.
[216] R. Jiang et al., The effects of the amount of Ge4+ doped in Zn2Ga3.98-4x/3GexO8:Cr0.02 nanoparticles on size distribution, NIR afterglow imaging and temperature sensing, J. Alloy. Compd. 822 (2020), https://doi.org/10.1016/j.jallcom.2019.153626 153626.
[217] A. Naughton-Duszová, L. Marciniak, A. Dubiel, J. Laszkiewicz-Łukasik, K. Kniec, M. Podsiadło, ZrB2 matrix composites with Cr3+/Nd3+ doped Al2O3 luminescent nanoparticles for non-contact temperature sensing, Process. Appl. Ceram. 14 (3) (2020) 181–187, https://doi.org/10.2298/pac2003181n.
[218] Q.i. Bao, Z. Wang, J. Sun, Z. Wang, X. Meng, K. Qiu, Y. Chen, Z. Yang, P. Li, Crystal structure, luminescence properties, energy transfer, tunable occupation and thermal properties of a novel color-tunable phosphor NaBa1-zSrzB9O15: X Ce3+, y Mn2+, Dalt. Trans. 47 (39) (2018) 13913–13925, https://doi.org/10.1039/C8DT02780C.
[219] B. Zhuang, Y. Liu, S. Yuan, H. Huang, J. Chen, D. Chen, Glass stabilized ultra-stable dual-emitting Mn-doped cesium lead halide perovskite quantum dots for cryogenic temperature sensing, Nanoscale 11 (32) (2019) 15010–15016, https://doi.org/10.1039/c9nr05831a.
[220] J. Zhang, Y. Shi, S. An, Photoluminescence properties of Ca9La(PO4)5SiO4F2: Ce3+/Tb3+/Mn2+ phosphors for applications in white light-emitting diodes

and optical thermometers, Spectrochim. Acta - Part A Mol. Biomol. Spectrosc. 229 (2020) 117886, https://doi.org/10.1016/j.saa.2019.117886.
[221] Y. Zhu, C. Li, and D. Deng, "Temperature sensitive Properties of Eu2+/ Mn2+ Co-doped Ca2Sr (PO4)2," in *2019 18th International Conference on Optical Communications and Networks, ICOCN 2019*, 2019, pp. 1–3, doi: 10.1109/ICOCN.2019.8934125.
[222] H. Liu, L. Mei, L. Liao, Y. Zhang, Q. Guo, T. Zhou, Y. Wang, L.i. Li, Strategy for realizing ratiometric optical thermometry via efficient Tb3+-Mn2+ energy transfer in novel apatite-type phosphor Ca9Tb(PO4)5(SiO4)F2, J. Alloy. Compd. 770 (2019) 1237–1243, https://doi.org/10.1016/j.jallcom.2018.08.167.
[223] Y. Zhang, H. Yao, Y. Xu, Z. Xia, Synergistic weak/strong coupling luminescence in Eu-metal-organic framework/Zn2GeO4:Mn2+ nanocomposites for ratiometric luminescence thermometer, Dye. Pigment. 157 (2018) 321–327, https://doi.org/10.1016/j.dyepig.2018.05.002.
[224] W. Liu, X. Wang, Q.i. Zhu, J.-G. Li, Tb3+/Mn2+ singly/doubly doped Sr3Ce (PO4)3 for multi-color luminescence, excellent thermal stability and high-performance optical thermometry, J. Alloy. Compd. 829 (2020) 154563, https://doi.org/10.1016/j.jallcom.2020.154563.
[225] N.a. Wang, T. Li, L. Han, Y. Wang, Z. Ci, Y. Wang, H. Jiao, The fluorescence self-healing mechanism and temperature-sensitive properties of a multifunctional phosphosilicate phosphor, J. Mater. Sci. 54 (8) (2019) 6434–6450, https://doi.org/10.1007/s10853-019-03350-w.
[226] Q. Wang, M. Liao, Z. Mu, X. Zhang, H. Dong, Z. Liang, J. Luo, Y. Yang, F. Wu, Ratiometric optical thermometer with high sensitivity based on site-selective occupancy of Mn2+ ions in Li5Zn8Al5Ge9O36 under controllable synthesis atmosphere, J. Phys. Chem. C 124 (1) (2020) 886–895, https://doi.org/10.1021/acs.jpcc.9b09379.
[227] K. Maciejewska, B. Poźniak, M. Tikhomirov, A. Kobylińska, and L. Marciniak, "Synthesis, cytotoxicity assessment and optical properties characterization of colloidal gdpo4:Mn2+, eu3+ for high sensitivity luminescent nanothermometers operating in the physiological temperature range," *Nanomaterials*, vol. 10, no. 3. 2020, doi: 10.3390/nano10030421.
[228] P. Wang, J. Mao, L.u. Zhao, B. Jiang, C. Xie, Y. Lin, F. Chi, M. Yin, Y. Chen, Double perovskite A2LaNbO6:Mn4+, Eu3+ (A = Ba, Ca) phosphors: Potential applications in optical temperature sensing, Dalt. Trans. 48 (27) (2019) 10062–10069, https://doi.org/10.1039/C9DT01524H.
[229] W. Li, H. Zhang, S. Chen, Y. Liu, J. Zhuang, B. Lei, Preparation and properties of carbon dot-grafted CaAl12O19:Mn4+ Color-tunable hybrid phosphor, Adv. Opt. Mater. 4 (3) (2016) 427–434, https://doi.org/10.1002/adom.201500572.
[230] J. Hu, E. Song, Y. Zhou, S. Zhang, S. Ye, Z. Xia, Q. Zhang, Non-stoichiometric defect-controlled reduction toward mixed-valence Mn-doped hexaaluminates and their optical applications, J. Mater. Chem. C 7 (19) (2019) 5716–5723, https://doi.org/10.1039/C9TC01026B.
[231] H. Zhou, N. Guo, M. Zhu, J. Li, Y. Miao, B. Shao, Photoluminescence and ratiometric optical thermometry in Mn4+/Eu3+ dual-doped phosphor via site-favorable occupation, J. Lumin. 224 (2020) 117311, https://doi.org/10.1016/j.jlumin.2020.117311.
[232] Y.i. Wei, H. Yang, Z. Gao, Y. Liu, G. Xing, P. Dang, A.A.A. Kheraif, G. Li, J. Lin, R.-S. Liu, Strategies for designing antithermal-quenching red phosphors, Adv. Sci. 7 (8) (2020) 1903060, https://doi.org/10.1002/advs.v7.810.1002/advs.201903060.